

# Site U1322<sup>1</sup>

Expedition 308 Scientists<sup>2</sup>

## Chapter contents

Background and objectives .....	1
Summary of operations .....	3
Lithostratigraphy .....	4
Biostratigraphy .....	6
Paleomagnetism .....	11
Geochemistry and microbiology .....	12
Physical properties .....	14
Downhole measurements .....	16
References .....	21
Figures .....	22
Tables .....	88

## Background and objectives

### Geologic setting of Mars-Ursa Basin

The Mars-Ursa salt-withdrawal basin (hereafter referred to as "Ursa Basin") is located 210 km south-southeast of New Orleans, Louisiana (USA), on the northeastern Gulf of Mexico continental slope in 800–1400 m water depth (Fig. F1). The 500 and 1000 m bathymetric contours shift to the south in this location and record the center of deposition for late Pleistocene sediments from the Mississippi River (Fig. F1). Rapid sedimentation obscured the otherwise hummocky nature of the seafloor in the northern Gulf of Mexico slope (Fig. F1). The study area is bounded to the west by Mars Ridge, a prominent north-south-trending bathymetric high (Fig. F2). Eastward from Mars Ridge, the seafloor slopes down to a zone of slope failures, including one failure described as one of the largest submarine slope failures in the world (Fig. F2) (McAdoo et al., 2000).

In the north-central Gulf of Mexico, the late Pleistocene shelf, shelf-margin, and minibasin turbidite deposits that were sourced from the Mississippi River are termed the Eastern Depositional Complex (Winker and Booth, 2000). The shelf and shelf-margin deposits were described by Coleman and Roberts (1988) and McFarlan and LeRoy (1988). The deepwater strata explored during Expedition 308 comprise one component of this system. These strata accumulated outboard of the shelf break during marine isotope Stages (MIS) 2–4 in response to late Wisconsinan continental glaciation (Winker and Booth, 2000; Winker and Shipp, 2002). They overlie the MIS 5 condensed section that contains the extinction events of the planktonic foraminifer *Globorotalia flexuosa* (70 ka) and the calcareous nannofossil *Pontosphaera* 1 (~70 ka) (Styzen, 1996; Winker and Booth, 2000). This regional datum has been identified in the Mississippi Fan and in other research and industry drill holes in the Gulf of Mexico (Joyce et al., 1990; Martin et al., 1990).

Late Pleistocene strata in Ursa Basin have received attention since the 1990s when overpressured and unconsolidated sands in the shallow section plagued drilling operations (Eaton, 1999; Ostermeier et al., 2000; Winker and Shipp, 2002). This drove the acquisition of high-resolution three-dimensional seismic data and several geotechnical cores to study the geological and geotechnical framework in the region (Fig. F3). Most recently, Sawyer et al. (submitted) presented a comprehensive analysis of the Mars-Ursa latest Pleistocene depositional system.

<sup>1</sup>Expedition 308 Scientists, 2006. Site U1322. In Flemings, P.B., Behrmann, J.H., John, C.M., and the Expedition 308 Scientists, Proc. IODP, 308: College Station TX (Integrated Ocean Drilling Program Management International, Inc.). doi:10.2204/iodp.proc.308.106.2006

<sup>2</sup>Expedition 308 Scientists' addresses.



## Stratigraphic succession

Sediments deposited in the last ~70 k.y. in Ursa Basin can be divided into four successive depositional units, from the older to the younger (Fig. F4):

- Blue Unit,
- Ursa Canyon channel-levee system,
- Southwest Pass Canyon channel-levee system, and
- Distal fan and hemipelagic deposition.

### Blue Unit

The Blue Unit is composed of interbedded sand and mud. The base of the Blue Unit is the base of the deepest sheet sand that ties to a weak negative amplitude reflection within the shallow sedimentary section (Fig. F4). The top of the Blue Unit ties to a strong positive amplitude seismic reflection that marks an increase in impedance with depth at the top of sands within the Blue Unit.

The top of the Blue Unit is difficult to correlate because of its complex seismic character and because it is eroded in places. The top sand within the Blue Unit is truncated by deformation zones associated with two channel-levee systems in the western part of the study area (Fig. F4). In areas where the top of the Blue Unit is not present, it has been mapped as the base of the deformation zones (Sawyer et al., submitted).

### Channel-levee systems

The Ursa Canyon channel-levee system contains a core, deformation zone, and levees (Fig. F4). The core has high-amplitude, chaotic seismic reflections. A deformation zone characterized by rotated slump blocks surrounds the channel core. Both the Blue Unit and levee material are deformed, but not the core. The levees have thin subparallel reflectors and gullwing shapes; they flank each side of the channel and thin laterally away.

The Southwest Pass Canyon channel-levee system is younger and lies west of the Ursa Canyon channel-levee system (Fig. F4). It eroded much of the western levee of the Ursa channel and completely buried the Ursa core and eastern levee. It is similar to the Ursa Canyon channel-levee system, although it is significantly larger.

### Mass transport deposits

Multiple mass transport deposits (MTDs) are present (Fig. F4). The bases of the MTDs are marked by a prominent horizontal reflection that separates parallel reflectors below from the nonreflective MTD above. The edges of the MTDs are marked by the

abrupt, near-vertical termination of the levee facies (Fig. F4).

## Mapped surfaces at Site U1322

Seismic surfaces that could be correlated across all three drill sites are delineated as S10–S80. Surfaces that are particular to a site are delineated by adding the site name to the reflector name, for example “S50-1322” (Table T1). A predrilling time-depth model was composed based on regional check shot data:

$$\text{mbsf} = -8.2595 \times (t_{\text{bsf}})^3 + 107.50 \times (t_{\text{bsf}})^2 + 779.89 \times (t_{\text{bsf}}) - 8.2823, \quad (1)$$

where  $t_{\text{bsf}}$  = two-way traveltime below seafloor (seconds).

## Location of Site U1322

Site U1322 is the easternmost Expedition 308 site in Ursa Basin (Fig. F3). It is located within Mississippi Canyon Lease Block 855 (Fig. F4). Eight seismic surfaces are mapped (Figs. F4, F5; Table T1). Seismic Reflectors S10, S20, S30, and S80 are regional surfaces that span all three drill sites. Seismic Reflector S30 is a detachment surface that underlies one of the MTDs, seismic Reflector S80 is the base of the Blue Unit, seismic Reflector S40-1322 underlies a reflective package and caps an MTD, and seismic Reflectors S50-1322, S60-1322, and S70-1322 mark detachment surfaces for a series of MTDs.

## Drilling objectives

The primary drilling objectives at this site were the following:

- Characterize pressure as a function of depth.
- Characterize porosity as a function of depth.
- Illuminate controls on slope stability.
- Understand the timing of sedimentation and slumping.
- Establish geotechnical and petrophysical properties of sediments.
- Characterize lithology and depositional processes of these channelized turbidite systems.

To achieve these objectives, a dedicated first hole (Hole U1322A) was drilled to conduct logging-while-drilling/measurement-while-drilling (LWD)/(MWD) operations to a terminal depth (TD) of 238 meters below seafloor (mbsf). Hole U1322B was cored to a TD of 238 mbsf. Advanced piston coring (APC) was used from the top to the bottom of the hole. Special tool deployments included three deployments of the temperature/dual pressure (T2P) probe. Two additional geotechnical holes (Holes U1322C and U1322D) were drilled, and eight T2P and four Davis-



Villinger Temperature-Pressure Probe (DVTTP) deployments were performed in these holes.

## Summary of operations

### Hole U1322A

A summary of operations for Hole U1322A can be found in Table T2. Hole U1322A was spudded at 0130 h on 15 June 2005 when the driller tagged the seafloor at 1330.0 meters below rig floor (mbrf) (precision depth recorder [PDR] = 1336.4 mbrf). The bit was jettied to 3.8 mbsf and the vibration-isolated television (VIT) camera was recovered. The hole was then drilled with an MWD/LWD string from 3.8 to 200.0 mbsf at an average rate of penetration (ROP) of 30 m/h. To ensure that we did not exceed our target depth, the interval from 200 to 238.0 mbsf was drilled at an ROP of 20 m/h. There was no indication of pressurized sands throughout the drilled interval. Resistivity and gamma ray data indicated that the main lithology was mud. After the hole was displaced with 70 bbl of 8.9 ppg sepiolite mud, the drill string was pulled out of the hole, clearing the seafloor at 1525 h on 15 June. When the bit was placed at 1040 mbrf, or ~222 m above seafloor, the dynamic positioning (DP) operator began to offset the vessel to Site U1323. The vessel departed location at 1600 h, leaving behind the beacon because of the planned return to this site subsequent to coring operations at Site U1324. A more detailed description of MWD/LWD operations in Hole U1322A can be found in “[Downhole measurements](#).”

### Hole U1322B

A summary of operations for Hole U1322B can be found in Table T3. The vessel was offset 6.2 nmi from Site U1324 on a heading of 079° and an average speed of 1.0 kt and arrived at the location of Site U1322 at 0915 h on 28 June 2005. After observing the seafloor with the VIT camera, Hole U1322B was spudded with the APC at 1145 h. The water depth calculated based on recovery of the first core was 1330.5 mbrf (PDR = 1336.4 mbrf). Piston coring advanced to 61.0 mbsf, when operations were interrupted because a control transformer in the variable field supply of the core winch failed. This required 3.75 h to troubleshoot and repair. Piston coring resumed at 2345 h on 28 June and continued to 0730 h on 30 June, when the total depth of 234.5 mbsf was reached. The average recovery for the hole was 101.0%. Cores were oriented starting with Core 4H. Fluorescent microspheres were deployed in the core catchers of Cores 1H–11H and then on every even-numbered core barrel. The Fugro cutting shoe was used on even-numbered barrels, except when the

APC temperature (APCT) tool was deployed. The uppermost 10 cores and Core 15H fully stroked, and all the other cores partially stroked and were advanced by recovery. The nonmagnetic core barrel was used for all cores.

The T2P probe was deployed three times in this hole. The first measurement in the hole was made at 42.0 mbsf for 60 min following Core 5H. The second attempt was subsequent to Core 15H at 134.3 mbsf and lasted 30 min. On this occasion, the hole was displaced with 10.5 ppg mud. The last deployment lasted 60 min at 157.8 mbsf. This deployment was made after recovering Core 18H and with the hole displaced with 55 bbl of 10.5 ppg mud. The DVTTP was deployed once at 166.7 mbsf, following Core 19H. The hole was displaced with 55 bbl of 10.5 ppg mud prior to this 90 min DVTTP deployment. The bit was pulled free of Hole U1322B at 1010 h on 30 June.

### Hole U1322C

A summary of operations for Hole U1322C can be found in Table T4. Hole U1322C was dedicated to temperature and pressure measurements. Mechanical and electronic problems with the probes during earlier deployments compromised many measurements, and further deployments were required to complete the data set and resolve reliability issues. Following a DP offset 20 m west of Hole U1322A, the VIT camera was deployed. Visual examination of the seafloor confirmed a clear area under the bit. Hole U1322C was spudded with the APC at 1125 h on 30 June 2005. The recovery of the first and only core in this hole established the seafloor depth at 1330.0 mbsf. The hole was then drilled in six intervals to a final depth of 231.5 mbsf. The T2P probe was deployed at 50, 75, 150, and 200 mbsf. On each occasion the probe stayed at the bottom of the hole for 60 min without rotation or circulation. After the first measurement, the hole was stabilized by displacing it with 10.5 ppg mud. The DVTTP was deployed at 100 mbsf (90 min), 220 mbsf (60 min), and 238 mbsf (90 min). Additionally, the hole was displaced with heavy mud prior to each deployment with no circulation or rotation of the drill bit. The hole was displaced with an additional 75 bbl of 10.5 ppg mud prior to abandonment. The bit cleared the seafloor at 1824 h on 1 July and was observed with the VIT camera to ensure that no flow was visible.

While operating in Hole U1322C, the work boat *Emily G* made the third and final visit to the *JOIDES Resolution*. The *Emily G* was on our location and standing by at 0400 h on 30 June. She came alongside and was secured to the port side by 0555 h and offloaded to our vessel catering supplies and freight



originally destined for Panama. We also loaded 35.5 short tons (710 sacks) of Florigel (Attupulgite) from the *Emily G.* The work boat departed for Port Fourchon, Louisiana, at 0930 h, transporting the Mud Engineer George Stokes and two other personnel (Integrated Ocean Drilling Program [IODP] Marine Laboratory Specialist Karen Johnson and Transocean DP Operator John Powell) to shore.

For various technical reasons, many deployments of the probes in Hole U1322C did not yield accurate results, with the exception of the DVTPP deployment at 236 mbsf and a T2P deployment at 150 mbsf. Based on these results (or lack thereof), we decided to spend the remaining 36 h of operation time drilling an additional hole devoted to pressure and temperature measurements at Site U1322. This decision was also motivated by the fact that our revised authorized depth of penetration at Site U1323 (174 mbsf) meant that the interval of major scientific interest could not be penetrated. The purpose of Hole U1322D was to deploy the pressure and temperature probes and spot core after each deployment.

### Hole U1322D

A summary of operations for Hole U1322D can be found in Table T5. The vessel was offset 20 m north of Hole U1322A, where Hole U1322D was spudded with the APC at 1925 h on 1 July 2005. This followed a seafloor survey with the VIT camera. The first core established the seafloor depth at 1330.0 mbrf. The hole was drilled and cored in five steps to a total depth of 175.0 mbsf. Three piston cores were obtained from the seafloor to 9.5, 70.0–79.5, and 100.0–107.8 mbsf. The average recovery of the cored interval of 26.8 m was 101.5%. The T2P probe was deployed four times: at 40.0 mbsf (60 min), 70.0 mbsf (45 min), 100 mbsf (45 min), and 134 mbsf (45 min). The DVTPP was deployed at 175.0 mbsf for 60 min. With the exception of the first T2P run, the holes were displaced with heavy mud prior to deployment and all downhole measurements were attempted with no circulation or rotation.

All operations concluded by 1600 h on 2 July to allow sufficient time to recover the drill string, beacons, and disassemble and store the bottom-hole assembly (BHA) components. The VIT camera was deployed prior to withdrawal of the drill string from the hole, and a short inspection of the top of Hole U1322D confirmed the absence of flow. After the drilling equipment was secured, the vessel began the voyage to Panama at 0030 h on 3 July.

## Lithostratigraphy

Site U1322 has a thinner sediment package above the Blue Unit than either Site U1323 or U1324. Sedi-

ment was recovered to 234.5 mbsf. The succession was divided into two lithostratigraphic units (Units I and II) on the basis of visual core descriptions from Hole U1322B (Fig. F6; Table T6). The total depth of this hole ties closely to seismic Reflector S60-1322. The boundary between lithostratigraphic Units I and II (125.8 mbsf) occurs just above seismic Reflector S30 (Fig. F6). Lithostratigraphic Unit I is dominated by clay locally interbedded with silt and is further divided into four subunits based on intervals of deformed and undeformed sediment. Lithostratigraphic Unit II is composed of mud and characterized by the alternation of deformed and undeformed sediment.

### Description of lithostratigraphic units

#### Unit I

Interval: 308-U1322B-1H-1, 0 cm, through 15H-1, 100 cm

Depth: 0–125.8 mbsf

Age: Holocene/late Pleistocene

Lithology: clay

Lithostratigraphic Unit I includes four subunits (IA–ID). This unit is predominantly composed of clay with a 2 m thick interval of foraminifer-nannofossil-bearing clay at the top. Subunit division is based on the observation of distinct intervals of deformed sediment (Subunits IB and ID). The ratio of deformed intervals to total thickness in this unit is ~47%. The base of lithostratigraphic Unit I is defined at the base of a highly deformed interval and ties to just above seismic Reflector S30.

#### Subunit IA (0–37.4 mbsf)

Lithostratigraphic Subunit IA is 37.43 m thick and is characterized by 1–3 cm thick olive-green and reddish brown couplets of clay accompanied by black mottled bands (Fig. F7). The clay couplets have sharp bases and show color gradation upward from dark green/black near the base to reddish brown at the top. Grain-size grading associated with color change could not be determined by core or smear slide examination. Black mottled bands are rich in organic matter, the color most likely caused by iron sulfide precipitation. The uppermost 2 m of this subunit is rich in foraminifers and nannofossils. The base of lithostratigraphic Subunit IA at 37.43 mbsf is marked by a sharp contact between flat bedding above and deformed bedding below.

#### Subunit IB (37.4–58.6 mbsf)

Lithostratigraphic Subunit IB is composed of centimeter-thick beds and laminae of deformed greenish gray and reddish brown clay. Two strongly folded



and steeply dipping intervals occur in this subunit and are marked by sharply defined basal surfaces at 41.25 and 52.45 mbsf, respectively. The interval between 41.25 and 52.45 mbsf is characterized by brittle deformation including small-scale (centimeter-scale vertical offset) reverse and normal faults (Fig. F8).

#### **Subunit IC (58.6–91.3 mbsf)**

Lithostratigraphic Subunit IC is composed of couplets of greenish gray and brownish gray laminae and thin beds of clay with thicknesses ranging 1–5 cm (Fig. F9). A minor silt component occurs throughout this subunit in laminae, discontinuous lenses, and millimeter-sized burrow fills. The silt-sized grains are predominantly quartz with variable amounts of mica, calcite, dolomite, and other minor constituents.

#### **Subunit ID (91.3–125.8 mbsf)**

Lithostratigraphic Subunit ID is composed of deformed reddish brown and greenish gray clay couplets (Fig. F10). The subunit has a tightly folded zone in the middle that grades downward into a homogeneous clay interval. The homogeneous intervals contain greenish gray and/or brownish gray mud without any sedimentary structures or faults. Reddish mud clasts incorporated in the homogeneous clay are present at the base of this subunit.

### **Unit II**

Interval: 308-U1322B-15H-1, 100 cm, through  
29H-CC, base

Depth: 125.8–234.5 mbsf

Age: late Pleistocene

Lithology: clay and mud

The top of Lithostratigraphic Unit II corresponds to a sharp contact at the base of the thickest deformed interval in Lithostratigraphic Unit I at 125.8 mbsf (Fig. F10) and coincides with the change from a deformed interval above to a laminated and undeformed interval below. This unit is made up of alternating intervals of meter-scale deformed, laminated clay or mud. The deformed intervals are composed of interbeds of brownish and greenish gray mud and are characterized by dipping beds, small-scale faults, recumbent folds, and mud clasts (Fig. F11). Some intervals contain homogeneous mud with a few centimeter- to decimeter-scale mud clasts. These homogeneous layers are more frequent at the base of deformed (folded and faulted) intervals (Fig. F12). We distinguished nine deformed intervals separated by undeformed mud layers at their boundaries. The deformed intervals have thicknesses varying from 2 to 5 m (intervals 2-1 to 2-9 in Fig. F6; Table T7). The

ratio of the deformed intervals to total thickness of lithostratigraphic Unit II is 61% if the homogeneous mud intervals are included as part of the deformed intervals.

Coherent intervals between deformed intervals consist of dark greenish gray and reddish gray laminated mud with local occurrences of black mottled mud as laminae and specks. Three intervals in the upper part of lithostratigraphic Unit II show distinct increases in silt content (Fig. F6), which occurs as thin laminae and specks (burrow fills) throughout these intervals. Silt laminae occur at frequencies of about 5/m; most laminae are discontinuous and disrupted by bioturbation.

### **X-ray diffraction analysis**

Fourteen clay and mud samples from Hole U1322B were analyzed by X-ray diffraction (XRD) to evaluate downhole variations in bulk mineralogy (Fig. F13). The diffractograms illustrate that the mineralogy consists of a mixture of quartz, calcite, dolomite, feldspars, and various phyllosilicates (Fig. F14). In this preliminary study we did not attempt to quantify the mineralogy of the clays and restricted the analysis to bulk rock powders.

With the exception of samples taken from Core 308-U1322B-1H, the overall composition of the samples is remarkably similar, although variations in peak intensities indicate changes in mineral proportions. The larger variations in abundance are observed in the quartz, calcite, and dolomite peaks. The abundance of calcite to dolomite is estimated by taking the ratio of counts per second from the principal peak of each mineral (Fig. F15). At 0.47 mbsf, the foraminifer-nannofossil-bearing clay is dominated by the calcite peak, with a calcite/dolomite peak ratio of ~35, dropping rapidly to ~0.8 in the mottled clay below at 2.14 mbsf. At ~36 mbsf, the calcite/dolomite ratio increases to ~2, with negligible difference between adjacent samples of clay of different colors. Samples taken from various clay and mud intervals below 100 mbsf suggest that dolomite is consistently more abundant, although the calcite/dolomite ratio varies significantly between 0.3 and 0.9. Abundances of calcite and dolomite in the XRD samples are consistent with smear slide observations that show a significant component of calcite in most samples (Fig. F13) and with coulometric analysis (see “[Geochemistry and microbiology](#)”) that shows significant amounts (10–20 wt%) of inorganic carbon throughout the sediments.

The calcite encountered was characterized based on smear slide observations as composed of a mixture of detrital grains and biogenic components (nannofossils and foraminifers). The dolomite grains are most

likely detrital. Thus, it is possible that variations in the calcite/dolomite ratio are in part related to variations in the input of detrital sediment versus biogenic components. Additional shore-based studies with a more representative set of samples are necessary to resolve any smaller-scale variations.

### Interpretation of lithostratigraphy

Lithostratigraphic Unit I is interpreted to contain a succession of clay turbidites deposited in a distal levee environment. Two MTDs occurred within this levee assemblage. Lithostratigraphic Subunit IA is interpreted as hemipelagic drape and very distal turbidites. Lithostratigraphic Subunits IB and ID do not have distinct grain size differences compared to the other subunits within Unit I, but the presence of deformed beds indicate that these intervals have been remobilized and are thus interpreted as MTDs. The homogeneous interval at the base of lithostratigraphic Subunit ID contains mud clasts, which suggest that it is part of the same MTD.

The lithology of lithostratigraphic Unit I (0–125.8 mbsf) at Site U1322 is similar to the lithology of lithostratigraphic Unit I at Site U1324. Seismic Reflectors S10 and S20, corresponding to the upper boundary of lithostratigraphic Subunit ID, can be traced between the two sites. Therefore, lithostratigraphic Unit I at Site U1322 is correlative with lithostratigraphic Unit I at Site U1324. Lithostratigraphic Subunit IA at Site U1322 is slightly thinner than at Site U1324 and also appears to be slightly finer grained (higher clay content). The thickness and apparent grain size changes are consistent with turbidity current overspill from a channel to the west.

The well-preserved layers observed in MTDs in Subunits IB and ID imply mild deformation during transport, meaning that they probably have not moved significant distances from their original location. The MTDs in Site U1324 are also characterized by mild deformation such as dipping and folding of beds, also indicating short transport distance (see the “[Site U1324](#)” chapter). On the other hand, the occurrence of a homogeneous interval at the base of lithostratigraphic Subunit ID indicates strong deformation and homogenization during transport and emplacement. Therefore, the style of deformation of lithostratigraphic Subunit ID at Site U1322 compared to the correlative Subunit ID at Site U1324 indicates that the former was transported farther than the latter.

The base of lithostratigraphic Unit I and top of lithostratigraphic Unit II at 125.8 mbsf marks a lithologic difference from highly deformed and homogenized mud above to coherently laminated mud below. This boundary ties closely to seismic Reflector S30, which

marks a significant contrast in seismic facies (Fig. F6). This major boundary also separates distinct log signatures in formation resistivity (Fig. F43; see “[Downhole measurements](#)”). Within lithostratigraphic Unit II the interpreted breaks at the top and base of packages of MTDs correspond closely to sharp excursions in resistivity. Many of the deformed intervals have higher resistivities than the laminated mud intervals, but the reverse is also observed. However, postcruise analysis of sediment velocity will resolve this issue.

Lithostratigraphic Unit II is characterized by alternating intervals of deformed sediment, homogeneous mud intervals, and coherent laminated mud intervals (Fig. F6). As observed for lithostratigraphic Subunits IB and ID, deformed intervals and homogenized intervals do not have distinct grain size differences compared to coherent intervals. However, the presence of deformed beds indicates that they have been remobilized and they are thus interpreted as MTDs. As the homogenized intervals occur at the base of deformed intervals, they are also interpreted as MTDs. The homogeneous nature of these intervals and the presence of mud clasts suggest emplacement by debris flows, whereas the folded and faulted intervals suggest emplacement by slumps and slides.

### Summary interpretation

Lithostratigraphic Unit I, composed of clay and muddy MTDs, can be correlated to lithostratigraphic Unit I at Site U1324 because of the continuous seismic reflectors and similar lithostratigraphic pattern. Channel-levee systems, west of Site U1324, are thought to be the sediment source. Overspills of mud and clay developed the levee assemblage.

Lithostratigraphic Unit II, composed of thinner interbedded muds and muddy MTDs, is characterized by a stacked set of MTDs at Site U1322. The total ratio of MTDs to total thickness is 61% in lithostratigraphic Unit II.

### Biostratigraphy

We studied calcareous nannofossils and foraminifers in all core catcher samples from Hole U1322B, one sample from Section 308-U1322C-1H-CC, and three core catcher samples from Hole U1322D plus additional samples from Cores 308-U1322B-1H and 15H. Calcareous nannofossils and foraminifers are rare to very abundant with good to moderate preservation in most samples, with reduced abundance toward the bottom of the holes.

Nannofossil Zone QAZ1 *Emiliania huxleyi* Acme with Subzones A (including intervals A1 through A5) and



B was identified, as well as planktonic foraminifer Zones Z and Y (including Subzones Y1–Y6) (Fig. F16). Nannofossil and planktonic foraminifer data indicate that, similar to Site U1324, the sediment sequence recovered at Site U1322 was essentially deposited during the last 60 k.y., with an average sedimentation rate of ~4 m/k.y. The encountered nannofossil and planktonic foraminifer zones correlate well with those at Site U1324. Several benthic foraminifer assemblages were recognized: *Cibicidoides-Globobulimina*, *Bolivina-Bulimina*, *Bulimina-Globobulimina*, and *Nonionella-Epistominella*. The predominance of infaunal benthic foraminifers suggests low-oxygenated “stress” environments due to rapid sedimentation. The deltaic *Nonionella-Epistominella* assemblage, containing many reworked inner neritic species from the lower part of the section, represents downslope transport from the Mississippi Delta.

### Calcareous nannofossils

Calcareous nannofossils were encountered in all samples from Holes U1322B, U1322C, and U1322D (Figs. F17, F18, F19). Nannofossils are extremely abundant in Sample 308-U1322B-7H-1, 100 cm, abundant in Sample 3H-CC, 6–16 cm, and common in other samples above 201.68 mbsf. Nannofossils in samples below 201.68 mbsf in Hole U1322B are rare, which may be related to MTDs in this part of the section. Preservation in the clays and muds ranges from good to moderate throughout the drilled holes. Coarse-grained samples typically contain poorly preserved nannofossils with low to barren overall abundance. Nannofossil assemblages contain rare to common in situ and reworked species. *E. huxleyi* is the most dominant in situ species. Other species, *Calcidiscus leptoporus*, *Ceratolithus cristatus*, *Ceratolithus telesmus*, *Discosphaera tubifera*, *Florosphaera profunda*, *Gephyrocapsa caribbeanica*, *Gephyrocapsa oceanica*, *Helicosphaera carteri*, *Helicosphaera wallichii*, *Pontosphaera multipora*, *Reticulofenestra productella*, *Rhabdosphaera clavigera*, *Rhabdosphaera procera*, *Scapholithus fossilis*, *Syracosphaera histrica*, *Thoracosphaera heimii*, *Thoracosphaera saxeae*, *Umbilicosphaera sibogae*, *Braarudosphaera bigelowii*, and *Coccolithus pelagicus*, were sporadically encountered. *G. oceanica* is typically more abundant than *G. caribbeanica*, although both rarely constitute ~20% of the total abundance. The reworked species are Cretaceous in age and occur throughout the section (Figs. F17, F18). Samples 308-U1322B-2H-CC through 7H-CC contain a persistent high number of reworked Mesozoic species.

Similar to Site U1324, species abundances vary significantly from sample to sample. This might be due to cyclic fluctuations in sediment input from the

Mississippi River. In general, the more abundant the in situ assemblages become, the less the reworked Mesozoic assemblages are found, and vice versa (Fig. F17). We found that hemipelagic environments preserved more in situ nannofossils, whereas environments containing more terrigenous material resulted in less preserved nannofossils and increased reworked Mesozoic assemblages.

Based on the nannofossil stratigraphic subdivision of Hine and Weaver (1998), we recognized the QAZ1 *E. huxleyi* Acme Zone at Site U1322. The zone was subdivided into Subzones A and B. Nannofossil intervals A1–A5 are distinguished (Fig. F20).

### QAZ1 *E. huxleyi* Acme Zone

We identified this zone in Samples 308-U1322B-1H-CC through 29H-CC, based on the dominant abundance of *E. huxleyi* (50% or more). According to Berggren et al. (1995), the first occurrence datum of *E. huxleyi* acme is at 90 ka. In situ species have sporadic distribution throughout the holes. Reworked Mesozoic assemblages form a significant percentage of the total nannofossil abundance in most samples from Site U1322. They typically have higher values in deformed zones (Fig. F17), for example, lithostratigraphic Subunit ID below 210.33 mbsf (see “[Lithostratigraphy](#)”).

#### Subzone A

We distinguished Subzone A in samples from above 201.68 mbsf in Holes U1322B (Samples 308-U1322B-1H-CC through 24H-CC), U1322C (Sample 308-U1322C-1H-CC), and U1322D (Samples 308-U1322D-1H-CC through 3H-CC). This interval is characterized by higher abundances of in situ and reworked nannofossils relative to Subzone B. The in situ species *E. huxleyi* shows cyclic distribution throughout Subzone A. It correlates with lithostratigraphic Unit I and the upper part of Unit II, above seismic Reflector S50-1322 (Fig. F16). Subzone A at Site U1322 corresponds to Subzone A at Site U1324. Within Subzone A, five intervals, A1–A5, were distinguished based on abundance variations in nannofossils. These intervals provide additional datums for correlation between Sites U1322 and U1324 (Fig. F20).

- Interval A1 is distinguished in the uppermost part of the drilled section (Sections 308-U1322B-1H-CC and 308-U1322C-1H-CC). It is characterized by nannofossil ooze dominated by *E. huxleyi* and relatively few reworked Mesozoic species (<500 specimens per 100 fields of view).
- Interval A2 is identified between 13.81 and 61.26 mbsf (Sections 308-U1322B-2H-CC through 7H-

CC and 308-U1322D-2H-CC). It is characterized by abundant reworked Mesozoic species with >500 specimens per 100 fields of view. *E. huxleyi* is abundant in the upper part of Interval A2 and becomes rare toward the bottom.

- Interval A3 lies between 61.26 and 125.75 mbsf (Sections 308-U1322B-8H-CC through 15H-1, 95–99 cm, and 308-U1322D-3H-CC). The main features of Interval A3 are fewer (<500 specimens per 100 fields of view) and variable reworked Mesozoic species relative to Interval A2 and cyclic distribution of *E. huxleyi* varying from barren to abundant. At the very bottom of Interval A3, reworked Mesozoic species become frequent (500–1000 specimens per 100 fields of view). At the base of Interval A3, the in situ and reworked Mesozoic species both show their lowest abundance values.
- Interval A4 is a short section between 125.75 and 142.03 mbsf (Sections 308-U1322B-15H-CC and 16H-CC). It is defined between the lowest total abundance and the maxima in a relative increase of the *G. caribbeanica*-*G. oceanica* group. Interval A4 has higher values of in situ nannofossil species relative to reworked Mesozoic species.
- Interval A5 is between 142.03 and 201.68 mbsf (Sections 308-U1322B-17H-CC through 24H-CC). The top boundary of Interval A5 is the top of the relative increase of the *G. caribbeanica*-*G. oceanica* group, and its base is marked by a decrease of in situ nannofossils. In situ nannofossils within Interval A5 always form >50% of the total abundance.

### Subzone B

Subzone B, containing low abundances of in situ assemblages, was identified in samples below 210.68 mbsf in Hole U1322B (Sections 308-U1322B-25H-CC through 29H-CC). Sudden decreases of in situ nannofossils and increases in reworked Mesozoic assemblages are the main characteristics of this subzone, and two peaks of reworked Mesozoic assemblages are associated with MTDs. Subzone B correlates with the lower part of lithostratigraphic Unit II between seismic Reflectors S50-1322 and S60-1322. Subzone B at Site U1322 can be correlated with the upper part of Subzone B at Site U1324 (Fig. F20).

Correlation of the distinguished nannofossil sub-zones and intervals between Sites U1322 and U1324 is presented in Figure F20. Sediments at Site U1322 above 142.03 mbsf correlate well with sediments from Site U1324 above 162.00 mbsf. This confirms the fact that the upper part of Site U1322 was deposited at a similar sedimentation rate as sediments at Site U1324 above 162.00 mbsf. Sediments below

142.03 mbsf at Site U1322 are condensed relative to those below 162.00 mbsf at Site U1324, making correlation difficult.

### Planktonic foraminifers

Planktonic foraminifers are rare to abundant in core catcher samples from Hole U1322B. In Cores 308-U1322B-5H through 13H and 22H through 29H, interpreted as an MTD, planktonic foraminifers are less abundant. In most samples, the preservation of planktonic foraminifers was good to excellent overall, and only few specimens exhibit abrasion features indicative of reworking. Semiquantitative data of planktonic foraminifers from Hole U1322B are presented in Table T8.

As at the other Expedition 308 sites, the planktonic foraminifer assemblage found in samples from Site U1322 is dominated by *Globigerinoides ruber* (both the pink and white forms) and other subtropical to temperate taxa. Warm-water species *Globorotalia menardii* and its associated forms occur only in Sample 308-U1322B-1H-CC, 5–10 cm, indicating Holocene Zone Z (Fig. F21). The absence of these species down-hole suggests that the sediment section between Cores 308-U1322B-2H and 29H belongs to Zone Y, which is younger than 90 ka (see “Biostratigraphy” in the “Methods” chapter). The last occurrence (LO) datum of *Globorotalia flexuosa* at 68 ka (Joyce et al., 1990), which marks the base of the Blue Unit (Winker and Booth, 2000), was not found. Several specimens of *Pulleniatina obliquiloculata* found in Cores 308-U1322B-17H through 19H may represent either in situ deposition from warm spills or reworking from the previous warm interglacial MIS 5. However, the suitability of these specimens to mark the temporary LO of *P. obliquiloculata* at ~65 ka (Kennett and Huddlestun, 1972; Mallarino et al., in press) is doubtful because these specimens are not concurrent with *G. menardii* in these samples or samples further downsection to indicate near Zone X deposition. Therefore, the absence of these key datum levels suggests that the sediment sequence recovered from Holes U1322B and U1322C was likely all younger than 60 ka, which is in good agreement with the 68 ka age of the base of the Blue Unit determined by Winker and Booth (2000).

### Zone Z

This zone is represented only by Sample 308-1322B-1H-CC, 5–10 cm (Fig. F21). The planktonic foraminifer assemblage is characterized by abundant warm-water species including *G. menardii*, *G. sacculifer*, *G. crassaformis*, *P. obliquiloculata*, and *G. ruber*. The cool-water species *G. inflata* present in this interval appears to have been reworked, as the species became



absent from the Gulf of Mexico about 10.5 k.y. ago and rarely concurred with *G. menardii* in younger intervals (Kennett and Huddlestun, 1972).

## Zone Y

From Cores 308-U1322B-2H through 29H, planktonic foraminifer assemblages are dominated by *G. ruber* and *G. inflata* and occasionally *G. falconensis* and *G. crassaformis*. The absence of warm-water species such as *G. menardii* (Zones X and Z) and *G. flexuosa* (lower Subzone Y6 and below) suggests that the sediment section spans Subzones Y1 through probably the later part of Y6 (Fig. F21). Together with abundance variations of species, these arrays of evidence helped the recognition of Subzones Y1, Y2, Y3–Y5, and Y5–Y6? (Fig. F21).

### Subzone Y1

Samples 308-U1322B-2H-CC, 17–27 cm, and 3H-CC, 6–16 cm, having abundant *G. ruber* and frequent *G. crassaformis* and *G. siphonifera* but reduced *G. inflata*, are assigned to Subzone Y1. According to Kennett and Huddlestun (1972), Subzone Y1 represents an interval of meltwater deposition at the MIS 1/2 transition at ~10.5–16 ka.

### Subzone Y2

Subzone Y2 spans Cores 308-U1322B-4H through 14H, or lithostratigraphic Subunits IB–ID, dominated by MTDs (see “[Lithostratigraphy](#)”). Subzone Y2 is characterized by increased abundance of the cool-water species *G. inflata*, especially from the upper and lower parts of the subzone, respectively, in Samples 308-U1322B-4H-CC, 29–34 cm, 5H-CC, 24–29 cm, and 12H-CC, 28–33 cm, through 14H-CC, 43–48 cm. *G. crassaformis* and *G. siphonifera* are also consistently present and may occasionally become frequent. Between Cores 308-U1322B-4H and 8H, *G. sacculifer* is virtually absent, suggesting a period of severe cooling during MIS 2. According to Kennett and Huddlestun (1972), Subzone Y2 represents deposition during MIS 2, which lasted from ~24 to 16 ka (Bassinot et al., 1994).

### Subzones Y3–Y5

The consistent occurrence of *G. sacculifer*, *G. ruber*, *G. crassaformis*, *G. falconensis*, and *G. inflata* without *G. menardii* and its associated species in Cores 308-U1322B-15H through 21H is considered to represent Subzones Y3–Y5. Because these subzones could not be separated using the data collected on board, the completeness of these subzones is not clear. Several specimens of the warm-water species *P. obliquiloculata* occur in three samples: 308-1322B-17H-CC, 40–

45 cm, 18H-CC, 31–36 cm, and 19H-CC, 28–33 cm. They appear to represent in situ deposition during warm spills rather than reworking from earlier interglacials because *G. menardii* and other species commonly associated with *P. obliquiloculata* in Zone X and earlier warm intervals are missing. It is noteworthy that the samples yielding these specimens are not from the deformed intervals in the upper part of lithostratigraphic Unit II (Fig. F21) (see “[Lithostratigraphy](#)”). According to Kennett and Huddlestun (1972), Subzones Y3, Y4, and Y5 represent deposition during MIS 3 at ~57–24 ka based on the timescale of Bassinot et al. (1994).

### Subzone Y5/Y6?

Planktonic foraminifers are rare in samples from Cores 308-U1322B-22H through 29H, from seismic Reflector S40-1322 to the bottom of Hole U1322B in the lower part of lithostratigraphic Unit II characterized by MTDs (see “[Lithostratigraphy](#)”). The interval is collectively assigned to Subzone Y5/Y6? pending further studies. The absence of *G. menardii* (Zone X, 85 ka and older) and *G. flexuosa* (lower Zone Y6, 68 ka and older) suggests that the sediment section must be younger than 68 ka. The temporary last occurrence of consistent *P. obliquiloculata* was at ~65 ka in Subzone Y6 (Kennett and Huddlestun, 1972; Malarino et al., in press). Several specimens of *P. obliquiloculata* found in three samples from Subzones Y3–Y5 (as mentioned above) may indicate an age close to 65 ka. However, the absence of such associated species as *G. menardii* and *G. flexuosa* from the Y3–Y5 interval, as well as the absence of all the three species from this Y5/Y6 interval, suggests an age younger than 65 ka for the lower sediment section at Site U1322. According to Winker and Shipp (2002), the *G. flexuosa* datum lies close to the base of the Blue Unit, which is ~200 m below the bottom of Holes U1322B and U1324B (see “[Background and objectives](#)” and “[Lithostratigraphy](#)” and also “[Background and objectives](#)” and “[Lithostratigraphy](#)” in the “Site 1324” chapter).

## Benthic foraminifers

Benthic foraminifers are rare to abundant in core catcher samples from Hole U1322B, becoming more abundant than planktonic foraminifers in Cores 308-U1322B-23H through 27H (Fig. F22). Preservation of benthic foraminifers in most samples varies from good to very good except for displaced or reworked specimens. The assemblages include many calcareous taxa and a few porcellaneous and agglutinated species. Species with an infaunal living mode are dominant, especially those preferring oxygen-poor, nutrient-rich environments. The *Bolivina-*



*Bulimina* assemblage, which was described at Sites U1319 and U1320, is also found at Site U1322 (above 330 mbsf). A *Bulimina-Globobulimina* assemblage, including the two subassemblages *Cibicidoides-Globobulimina* and *Bulimina-Globobulimina* and a *Nonionella-Epistominella* assemblage similar to those found in present-day sediments from the lower Mississippi Delta and upper slope are also recognized. Semiquantitative data of benthic foraminifers from Hole U1322B are listed in Table T9.

### ***Bolivina-Bulimina* assemblage**

The *Bolivina-Bulimina* assemblage was recognized in samples from Cores 308-U1322B-4H through 14H. As already described from Sites U1319 and U1320, this assemblage is characterized by abundant small thin-shelled species including *Bolivina spissa*, *Bolivina* spp., *Bulimina aculeata*, *Fursenkoina bradyi*, *Cassidulina laevigata*, *Stainforthia complanata*, and *Chilostomella ovoidea*. Epifaunal species such as *Gyroidina* spp. and *Cibicidoides* spp. are extremely rare or absent. This infauna-dominated assemblage indicates upper slope to lower bathyal depths greater than 400 m with low oxygen content due to rapid sediment loading. The predominance of *Bolivina* and *Bulimina* between 90 and 125 mbsf corresponds to the deformed section in lithostratigraphic Subunit ID (Fig. F22) (see “[Lithostratigraphy](#)”).

### ***Bulimina-Globobulimina* assemblage**

This assemblage is characterized by common occurrences of many species found in the *Bolivina-Bulimina* assemblage plus *Globobulimina affinis* and *Uvigerina hispidocostata*. The large thin-shelled *G. affinis* is very distinctive. The assemblage can be divided into two subassemblages: *Bulimina-Globobulimina* and *Cibicidoides-Globobulimina*, as detailed below.

The *Bulimina-Globobulimina* subassemblage is found in samples from Cores 308-U1322B-15H through 21H. Apart from those described above, rare to frequent *Bulimina mexicana*, *Oridosalis* spp., *Valvularia bradyana*, and *F. bradyi* may also be present. This subassemblage represents a benthic foraminifer association under lower-stress environments than the *Bolivina-Bulimina* assemblage.

The *Cibicidoides-Globobulimina* subassemblage spans Cores 308-U1322B-3H through 5H. Unlike the *Bulimina-Globobulimina* subassemblage, this subassemblage contains more frequent epifaunal taxa including *Cibicidoides*, *Oridosalis*, *Gyroidina*, and *Hoeglundina*, but *Fursenkoina* is virtually absent. It represents a transitional benthic foraminifer association toward a normal bathyal environment.

### ***Nonionella-Epistominella* assemblage**

We recognized the *Nonionella-Epistominella* assemblage in samples from Cores 308-U1322B-22H through 29H, characterized by numerous tiny *Nonionella basiloba* and *Epistominella exigua* with a test ~100 µm across. Small-sized *Bolivina*, *Stainforthia*, and *Cassidulina* and large-sized *Lenticulina* range from rare to frequent in this assemblage. Although relatively rare, reworked *Ammonia beccarii*, *Elphidium* spp., and *Quinqueloculina* spp. from inner neritic settings occur throughout the interval. Similar assemblages exist today along the outer margin of the Mississippi Delta, close to the shelf edge (Poag, 1981). The presence of this assemblage from the bottom part of Hole U1322B suggests strong downslope transport, probably related to the Southwest Pass Canyon or sediment gravity flows directly from the north during MIS 4 (see “[Background and objectives](#)”).

### **Age model and sedimentation rates**

The age models developed during the expedition are preliminary. Biostratigraphic dating of Pleistocene sediments is difficult, and we had to rely on several assumptions to constrain age models and sedimentation rates. In the case of Site U1322, we took into consideration planktonic foraminifer biostratigraphic data only (Table T10; Fig. F23). The age constraints are mainly derived from the modified ages for the boundaries between planktonic foraminifer subzones according to Bassinot et al. (1994) (see “[Biostratigraphy](#)” in the “Methods” chapter). The estimated sedimentation rates (Fig. F23) are 0.89 m/k.y. between the seafloor and 13.81 mbsf (last occurrence [LO] of *G. inflata*), 3.2 m/k.y. between 13.81 and 32.92 mbsf (Subzone Y2/Y3 boundary), and 1.8 m/k.y. between 125.75 and 189.0 mbsf (Subzone Y5/Y6 boundary). The interval between 32.92 and 125.75 corresponds to the lower part of lithostratigraphic Subunit IA-ID, which is characterized by frequent MTDs. This can explain the extremely high sedimentation rates in this interval (~12 m/k.y.). Below 189.0 mbsf, no biostratigraphic datum was recovered. However, considering that we did not retrieve *P. obliquiloculata* and *G. flexuosa* specimens, we infer that the oldest sediment recovered is younger than the LO of these two species (Subzone Y6; ~65 ka for the LO of consistent *P. obliquiloculata* [Kennett and Huddlestun, 1972; Mallarino et al., in press] and 68 ka for the LO of *G. flexuosa* [Joyce et al., 1990]). According to Winker and Booth (2000), the LO of *G. flexuosa* lies close to the base of the Blue Unit, which is ~200 m below the bottom of Hole U1322B (see “[Lithostratigraphy](#)”). Thus, assuming that the oldest sediment recovered in Hole U1322B is ~60 ka or older, we estimate a sedimentation rate



between 189.0 and 234.46 mbsf of 16 m/k.y. or greater. More rigorous postcruise work is needed to confirm this interpretation.

## Paleomagnetism

All archive-half cores of Hole U1322B were measured to a peak alternating-field (AF) demagnetization of 20 mT using the pass-through cryogenic magnetometer (Table T11). The APC coring system was used from Cores 308-U1322B-1H to 29H; Cores 6H to 29H were oriented using the Tensor tool (see “[Summary of operations](#)”). Hole U1322B was the first hole of the expedition where a special geotechnical cutting shoe from Fugro Inc. was deployed (Table T11). As this shoe is magnetic, its use resulted in a considerable overprint in the cores where it was deployed (see discussion below).

### Paleomagnetic intervals

Based on paleomagnetic measurements, Hole U1322B was divided into three paleomagnetic intervals. Unlike at previous sites, the paleomagnetic intervals in Hole U1322B were defined by the magnetic susceptibility ( $\kappa$ ) record rather than natural remanent magnetization ( $NRM_{20mT}$ ) because of the better correlation of  $\kappa$  between Sites U1324 and U1322.  $\kappa$  and  $NRM_{20mT}$  are weakly correlated in Hole U1322B. Paleomagnetic Interval 1 is characterized by a significant  $\kappa$  peak recognized between 0 and 37 mbsf. Paleomagnetic Interval 2, between 37 and 125 mbsf, is characterized by a steady increase in  $\kappa$ , whereas  $NRM_{20mT}$  intensity shows an interval of very low values. Lithostratigraphic Unit II corresponds to the top of paleomagnetic Interval 3, ranging from 125 to 234 mbsf. This interval indicates higher signal variance around a generally higher mean value. The paleomagnetic intervals are described in more detail below.

#### Interval 1 (0–37 mbsf)

Paleomagnetic Interval 1 lies within lithostratigraphic Subunit IA (see “[Lithostratigraphy](#)”).  $NRM_{20mT}$  averages  $\sim 0.006$  mA/m, with lower intensities of 0.002 mA/m toward the bottom of the interval (Fig. F24A).  $\kappa$  ranges between 0 and  $18 \times 10^{-5}$  SI, steadily increasing toward the bottom of Interval 1 (Fig. F24B). Declination has a relatively stable average direction of  $160^\circ$  (Fig. F24C). The mean inclination shows directions of  $\sim 55^\circ$  between 24 and 33 mbsf (Fig. F24D). However, Core 308-U1322E-4H shows deviating inclination directions of up to  $-35^\circ$ , coinciding with a clay lithology with minor silt laminae (see “[Lithostratigraphy](#)”). This subinterval is

labeled “A” in Figure F24D but was drilled using the magnetic Fugro drill shoe.

#### Interval 2 (37–125 mbsf)

Paleomagnetic Interval 2 includes lithostratigraphic Subunits IB, IC, and ID (see “[Lithostratigraphy](#)”).  $NRM_{20mT}$  is characterized by a low mean intensity of  $\sim 0.002$  mA/m throughout the whole interval (Fig. F24A), with the exception of some background noise. This interval was divided into two subintervals according to trends in  $\kappa$ . Between 37 and 70 mbsf,  $\kappa$  shows an average value of  $12 \times 10^{-5}$  SI. Starting at 70 mbsf,  $\kappa$  increases toward peak values of  $40 \times 10^{-5}$  SI at the bottom of the interval (Fig. F24B).  $NRM_{20mT}$  intensity shows no similar trend. Declination in Interval 2 is scattered throughout the range of possible values. In general, declination is noisy in this interval and is unreliable (Fig. F24C). Inclination has slightly shallower values on average than those in Interval 1, at  $\sim 50^\circ$ . There are three exceptions to this: between 62 and 71 mbsf (up to  $-85^\circ$ ), between 80 and 90 mbsf (up to  $-68^\circ$ ), and between 116 and 125 mbsf (up to  $-85^\circ$ ) inclination deviates markedly (these subintervals are labeled B, C, and D, respectively). Peaks B and C correlate with Cores 308-U1322B-8H and 10H, respectively.

The observed deviations in the inclination data in Hole U1322B (A, B, C, and D Intervals 1 and 2) correspond to cores taken with the geotechnical cutting shoe (Fugro Inc.), which is magnetic (see “[Summary of operations](#)”). This cutting shoe seems to cause a considerable magnetic overprint on the recovered sediments, and the excursions are therefore considered to be artifacts. Hence, data points from cores recovered using the Fugro cutting shoe were plotted in red and not included in the data analysis. The Fugro cutting shoe was deployed in Cores 308-U1322B-2H, 4H, 8H, 10H, and 14H and every even-numbered core downhole (see also Table T11). Therefore, the inclination deviations in Subintervals 2A–2D are caused by drilling overprint not removed by the applied peak field of 20 mT. Inclinations in Core 308-U1322B-2H show only slightly deviating values, but the overprint effect seems to be present as well. Below Core 308-U1322B-14H (in lithostratigraphic Unit II/paleomagnetic Interval 3), this overprint effect cannot be clearly distinguished from the average inclination direction. This may be due to the increasing consolidation state of the sediments with depth or the generally higher intensity values, and thus stronger remanent magnetizations, in this interval. The latter hypothesis is supported by the fact that the strongest inclination deviations occur within the  $NRM_{20mT}$  interval with the lowest intensity values (Fig. F24A).



### Interval 3 (125–234 mbsf)

Interval 3 spans lithostratigraphic Unit II and has relatively high average NRM<sub>20mT</sub> intensities compared to Intervals 1 and 2 (average value = 0.02 mA/m, ranging from 0.001 to 0.050 mA/m). Changes in NRM<sub>20mT</sub> values are very high and seem to correlate with the frequent changes in lithology (Fig. F25A). Therefore, data from this interval are not used for paleomagnetic studies. Values of  $\kappa$  average  $18 \times 10^{-5}$  SI (Fig. F25B).  $\kappa$  and NRM<sub>20mT</sub> show an even weaker correlation than in Intervals 1 and 2. Declination is less scattered but nevertheless noisy in Interval 3 (Fig. F24C). Some of the declination data seem to be offset from the general trend. Between 125 and 166 mbsf (Cores 308-U1322B-15H through 19H), declination shows decreasing directions from 140° to 10°. Below Core 308-U1322B-20H, the general direction is more or less stable at ~320°. Tensor tool data measured for the first five cores were lost to a data storage error; therefore, the orientation of these cores was not corrected. From Core 308-U1322B-6H to TD it was possible to reconstruct the orientation data from the Tensor tool, but the offsets in the record after correction seem artificial and therefore declination data are unreliable. Inclination is relatively stable (ranging between 30° and 45°) in Interval 3 in contrast to the noisy declination data (Fig. F24D).

### Magnetostratigraphy

Site U1322 is characterized by various MTDs and is not appropriate for paleomagnetic studies downhole from 125 mbsf. The uppermost 125 m of Hole U1322B (spanning paleomagnetic Intervals 1 and 2) correlate to the uppermost 160 m of Hole U1324B by its signal shape and the correlation of major seismic reflectors between the two sites (see “[Lithostratigraphy](#)”). Magnetic tie points MTP1 and MTP3 are identified in  $\kappa$  data (Fig. F24B), corresponding to MTP1 and MTP3 in Hole U1324B. But these tie points are tentative and solely supported by the magnetic susceptibility record. The NRM<sub>20mT</sub> intensity data do not show the same trends at these depth intervals. Therefore, no magnetic tie points were included in the preliminary age model (see Fig. F23).

## Geochemistry and microbiology

### Inorganic geochemistry

#### Interstitial water geochemistry

Interstitial water chemistry data for Site U1322 are listed in Table T12 and shown in Figures F26, F27, F28, and F29. Alkalinity is generally constant with minimal variation in concentration from 3.75 to 6.25 mM (Table T12). From the seafloor to ~34 mbsf

(i.e., seismic Reflector S10), alkalinity increases to a maximum of 5.85 mM and then decreases to a minimum of 3.75 mM at ~85 mbsf (i.e., seismic Reflector S20). Between 90 and 103 mbsf (i.e., seismic Reflector S30), alkalinity once again reaches a local maximum of 5.6 mM. Below seismic Reflector S30, alkalinity increases slightly at first and then remains constant until the bottom of the core (Fig. F26). The pH of the interstitial water varies between 6.46 and 7.65. The acidic nature of the interstitial water (pH <7) above 100 mbsf at this site is similar to pH at Site U1324, but large pH fluctuations with several mimima and maxima occur within this part of the core. From 100 mbsf to TD, pH values are higher and average  $7.2 \pm 0.1$  (Fig. F26).

Salinity varies between 3.3 and 3.8 parts per hundred (pph) (Table T12). Above 34 mbsf (i.e., seismic Reflector S10), salinity is higher, centered at 3.7–3.8 pph. Between 34 and 84 mbsf salinity decreases from 3.8 to 3.3 pph, and then it remains relatively constant downhole to the bottom of the hole. Interstitial water chlorinity varies from 542 to 578 mM. The seafloor chloride concentration is similar to the standard seawater value (International Association of the Physical Sciences of the Ocean [IAPSO] seawater standard = 559 mM), increases to 578 mM within the upper 15 mbsf (Fig. F26), and decreases back to approximately seawater chlorinity values within 50 mbsf.

Dissolved sulfate concentrations approximate standard seawater concentrations (28.9 mM) above 34 mbsf (i.e., seismic Reflector S10). Below this depth, sulfate concentrations rapidly decrease to a minimum of 0 mM at 75 mbsf and remain constant to TD (Fig. F27). The sulfate/methane interface (SMI) depth is 74 mbsf. Interstitial water ammonium concentrations are very high, ranging from 428 to 4432  $\mu$ M, and a general downhole increase is observed to 130 mbsf (i.e., seismic Reflector S30). Below seismic Reflector S30, ammonium contents are generally high and constant (~4000  $\mu$ M) to 190 mbsf and then decrease to 2274 mM at 207 mbsf. Below this depth, ammonium concentrations remain constant to the bottom of the hole. Dissolved phosphate concentrations are very low (<4.0  $\mu$ M), in particular above 34 mbsf (<2.8  $\mu$ M) (Table T12). Below 34 mbsf to TD, several local phosphate maxima are observed (Fig. F27). Interstitial water data also show elevated concentrations of dissolved silica ( $H_4SiO_4$ ) from 259 to 532 nM (Fig. F27).

$Na^+$  concentrations do not vary significantly downhole.  $Mg^{2+}$  displays minimal downhole variation, with slightly higher concentrations above seismic Reflector S10 than those elsewhere.  $K^+$  concentrations decrease and  $Ca^{2+}$  concentrations increase sig-



nificantly from the seafloor to ~34 mbsf (i.e., seismic Reflector S10). Below this interval to seismic Reflector S30 (165 mbsf), concentrations of K<sup>+</sup>, Mg<sup>2+</sup>, and Ca<sup>2+</sup> decrease slightly. Below seismic Reflector S30, concentrations of these elements remain relatively constant to the bottom of the hole (Fig. F28).

Downhole variations of Li<sup>+</sup>, B<sup>3+</sup>, and Sr<sup>2+</sup> concentrations are similar and generally increase to a maximum at ~34 mbsf (i.e., seismic Reflector S10) and then decrease toward seismic Reflector S30, although small local maxima are observed both for B<sup>3+</sup> and Sr<sup>2+</sup> within this interval (Fig. F29). Li<sup>+</sup>, B<sup>3+</sup>, and Sr<sup>2+</sup> concentrations remain constant below seismic Reflector S30 to TD. Concentrations of Ba<sup>2+</sup> are generally low (<1.3 µM) in depths shallower than 56 mbsf. The maximum concentration of 36.4 µM, at 75 mbsf (above seismic Reflector S20), decreases to 7.9 µM at 130 mbsf (i.e., seismic Reflector S30). Below this depth, Ba<sup>2+</sup> contents are constant at ~10 ± 2 µM (Fig. F29). Dissolved Mn<sup>2+</sup> concentrations rapidly decrease from a maximum of 61.2 µM near the seafloor and are generally <2 µM below 121 mbsf (Fig. F29). The interstitial water contains high concentrations of dissolved Fe<sup>2+</sup> at shallow depths, with two local maxima of 351 and 476 µM at 8.5 and 84 mbsf, respectively (Fig. F29). High concentrations of dissolved Fe<sup>2+</sup> caused iron oxyhydroxide precipitation (lepidocrocite, FeO[OH]), as deduced from XRD analyses of the precipitates from the pore waters immediately after squeezing in the laboratory. Several interstitial water samples from Holes U1322C and U1322D were also analyzed, and the data generally fit with chemical pore water profiles for Hole U1322B. In summary, large pore water chemical variations are observed at shallow depths, in particular around seismic Reflector S10.

### Solid-phase chemistry

Initial results for total inorganic carbon (TIC), calcium carbonate (CaCO<sub>3</sub>), total organic carbon (TOC), total nitrogen, molar ratio of organic carbon to total nitrogen (C/N), and total hydrogen analyses on sediment squeeze cakes are listed in Table T13 and presented in Figure F30.

TIC contents range from 0.62 to 2.82 wt% (average = 1.74 wt%, which corresponds to an average CaCO<sub>3</sub> concentration of 14.54 wt%). The foraminifer-nannofossil-rich clays within the uppermost 2–3 m of Site U1322 account for the peak maximum of 23.46 wt% in calcium carbonate. Inorganic carbon concentrations increase throughout lithostratigraphic Unit I to a maximum concentration of 2.82 wt% at ~130 mbsf. This peak concentration coincides with seismic Reflector S30 and the abrupt change from the clay-rich formation of lithostrati-

graphic Unit I to clay and mud interbedded MTDs in lithostratigraphic Unit II.

TOC contents generally decrease with depth, with local peak maxima at 10, 150, and 200 mbsf. TOC concentrations range between 0.26 and 1.64 wt% (average = 0.83 wt%). The spike in organic carbon at 10 mbsf corresponds with organic-rich black bands observed within the red and green color-banded clays of lithostratigraphic Subunit IA (see Fig. F7). Increases in TOC and decreases in TIC within lithostratigraphic Unit II at 150 and 200 mbsf are coincident with MTDs 2-2 and 2-5 in lithostratigraphic Unit II (see Fig. F6).

Total nitrogen concentrations, as a whole, are lower than concentrations observed at Ursa Basin Site U1324. Total nitrogen concentrations range from 0.05 to 0.21 wt% (average = 0.093 wt%). Peak concentrations in the total nitrogen curve occur opposite to local decreases in TOC in both lithostratigraphic Units I and II. Average total hydrogen contents vary between 0.01 and 2.84 wt% (average = 0.52 wt%).

C/N values at Site U1322 were the highest molar ratios observed during Expedition 308. C/N ratios range between 1.71 and 25.28 (average = 12.73). This broad range in ratios suggests input of organic matter from hemipelagic to predominantly terrestrial sources. C/N ratios center around an average value of 14.69 within lithostratigraphic Unit I, with rapid decreases at 20.9 and 44.2 mbsf and a spike in the ratio at 8.5 mbsf. C/N ratios exhibit far greater variability within the MTDs interpreted in lithostratigraphic Unit II. C/N minima at 143.8, 178.8, and 218.5 mbsf suggest greater relative input of hemipelagic organic matter, and maxima at 154.3, 186.7, and 199.9 mbsf imply higher amounts of terrestrial material.

### Solid-phase initial interpretations

Site U1322 has the highest average TOC content among all Expedition 308 sites. Interbasinal differences in organic matter concentrations indicate greater accumulation of TOC toward the center of Ursa Basin at Site U1322 relative to Site U1324 along the flank of the basin. Organic carbon concentrations and C/N ratios at Site U1322 peak within the uppermost 8.5 m in lithostratigraphic Unit I and again at 154.3 and 199.9 mbsf, coincident with MTDs 2-2 and 2-5 in lithostratigraphic Unit II (see Fig. F6), respectively. MTDs 2-1, 2-3, and 2-7 within lithostratigraphic Unit II (see Fig. F6) are also associated with decreasing TOC concentrations and lower C/N ratios. The origin of sedimentary organic matter may be better assessed with carbon and nitrogen isotopic analyses (Jasper and Gagosian, 1990).



## Organic geochemistry

### Hydrocarbon gas composition

The vertical distribution of headspace methane and ethane is shown in Figure F31. Methane concentrations in the headspace volumes range between 1 and 51,001 ppmv. Rapid increases in methane concentrations begin in the middle of lithostratigraphic Unit I, whereas there are only minor amounts of methane from the seafloor to 60 mbsf. Methane was the predominant hydrocarbon species determined at Site U1322. Only very minor amounts of ethane (<3.4 ppmv) and ethylene (<2.6 ppmv) were detected in headspace samples (Table T14). No higher hydrocarbons were detected at Site U1322. Concentrations of methane fluctuate with depth, and the calculated SMI occurs at 74 mbsf (Fig. F32). The highest concentrations of methane were in the range of 29,536–51,001 ppmv between 75 and 129 mbsf. According to the lithologic description, this gas-bearing interval consists of mud and clay, both confined within lithostratigraphic Unit I. These strata are also positively correlated with slight increases of diagenetic ethane.

The maximum concentrations of hydrocarbons in expansion void gas (EVG) in the headspace sampled in Section 308-U1322B-14H-2 were as follows:

- methane = 707,229 ppmv,
- ethane = 38 ppmv,
- ethylene = 1 ppmv, and
- butane = 3 ppmv.

The concentrations of methane in EVG were one order of magnitude higher than those of the maximum range in headspace samples. When interpreting  $C_1/C_2$  ratios or  $C_n/C_{n+1}$ , we need to consider that minor amounts of  $C_2$  through  $C_5$  compounds can also be generated in situ during early (low temperature) diagenesis of organic matter (e.g., Kvenvolden and Barnard, 1983). The  $C_1/C_2$  ratios at Site U1322 are generally high, suggesting biogenic origin of the methane, possibly derived from in situ microbial activities or migrated from elsewhere. Hence, the almost exclusive presence of methane suggests that the hydrocarbon gases found at Site U1322 are of biogenic, not thermogenic, origin. Stable carbon isotopic ratios ( $\delta^{13}\text{C}$ ) at the molecular level will help verify the origin of  $\text{CH}_4$  in headspace and EVG.

## Microbiology

### Biomass enumeration

Microbial cell biomass in Hole U1322B was estimated using whole-round core samples (Fig. F33). The sampling frequency was every 4–5 m between 2.9 and 21.0 mbsf, every 7–11 m between 21.0 and

129.2 mbsf, and every 14–20 m between 129.2 and 231.5 mbsf.

A maximum cell density of  $4.0 \times 10^5$  cells/mL was observed at 2.9 mbsf. Microbial abundances decreased with depth; at 74.5 mbsf, biomass was below the cell enumeration confidence limit of  $1.0 \times 10^4$  cells/mL (Table T15). The extremely low cellular biomass at Site U1322 is consistent with microbial abundance levels at Site U1324. The microbial biomass in Ursula Basin is an order of magnitude less than cellular densities observed at Sites U1319 and U1320 in Brazos-Trinity Basin IV.

## Physical properties

Downhole profiles of physical properties were established for Site U1322 where the overburden above the Blue Unit is thin (see “[Background and objectives](#)”). Physical properties are compared with those from Site U1324, where overburden above the Blue Unit is thick, and are also compared with those of Site U1323, where there is an intermediate overburden.

### Density and porosity

To increase the resolution of moisture and density (MAD) data near seismic Reflectors S20 and S30, extra samples were taken in Cores 308-U1322B-10H, 15H, 16H, and 17H.

Bulk densities determined from the different methods (gamma ray attenuation [GRA], MAD, and image-derived density [IDRO]) are in good agreement (Fig. F34A). LWD porosities were calculated assuming a grain density of  $2.7 \text{ g/cm}^3$  and a pore water density of  $1.024 \text{ g/cm}^3$ .

MAD bulk densities increase from  $1.3$  to  $\sim 1.8 \text{ g/cm}^3$  from the seafloor to 28 mbsf (Fig. F34A). Correspondingly, porosity values decrease from 80% to 56% (Fig. F34C). From 28 mbsf to the bottom of the hole there is little increase in density (and little decrease in porosity). Nevertheless, small shifts from the main trend are observed within this lower interval. The first is a 3% increase in porosity recorded from 28 mbsf (the depth of seismic Reflector S10) to 34 mbsf. This correlates with the silt laminae interval at the bottom of lithostratigraphic Subunit IA (see “[Lithostratigraphy](#)”). The next two shifts, up to 5% in porosity, are recorded at the base of lithostratigraphic Subunits IB and ID and are interpreted as MTDs. At these boundaries, the MTDs show higher densities and lower porosities than the nondeformed sediments below them. The boundary between the top of the MTDs and the nondeformed unit above is recorded with only a gradual change in density and porosity.



## Noncontact resistivity

Noncontact resistivities (NCR) at Site U1322 increase 0.2  $\Omega\text{m}$  from the seafloor to 30 mbsf and then remain relatively constant at ~0.6  $\Omega\text{m}$  until 70 mbsf (Fig. F35A). From that depth downhole resistivity values abruptly increase and become more scattered but center on a mean value of 1  $\Omega\text{m}$  (Fig. F35A). At 70 mbsf the first high methane concentrations were detected (see “[Geochemistry and microbiology](#)”). Thus, the large shift in NCR at this depth and the high scatter in the data are believed to result from gas expansion and the formation of voids and cracks.

NCR in Hole U1322B and LWD-derived resistivity measurements from Hole U1322A do not correlate well. Only a few peaks appear in both logs, but the shapes and magnitudes of the peaks are different. In addition, the resistivities from LWD data are generally higher than those of NCR (Fig. F35B). This might result from measurement conditions, especially temperature contrast between laboratory and in situ conditions.

In the uppermost 15 mbsf, resistivity increases more in the LWD data than the NCR data (Fig. F35A, F35B). The LWD data in this interval are probably affected by the large borehole diameter (see “[Down-hole measurements](#)”) and may be not as reliable as the NCR data. From 90 mbsf downhole, the LWD data show relatively constant values along the profile, with major excursions in MTD intervals (Fig. F35A). Some of these excursions may reach resistivities as high as 2.5  $\Omega\text{m}$ .

## Magnetic susceptibility

Magnetic susceptibility generally increases slightly from the top to the bottom of the hole (Fig. F36). In the uppermost part of the hole, very low magnetic susceptibility values correspond to increases in the carbonate content (see “[Lithostratigraphy](#)”). In lithostratigraphic Subunit IA (0–37.43 mbsf), magnetic susceptibilities increase with depth and then decrease to the base of the unit (Fig. F36). The maximum magnetic susceptibility value in this interval is reached at 31 mbsf, where a thin interval of silt/sand layers was identified, according to the lithostratigraphic description (see “[Lithostratigraphy](#)”). It correlates with seismic Reflector S10.

Magnetic susceptibilities within lithostratigraphic Subunit IB (37.43–58.60 mbsf) sharply increase from  $32 \times 10^{-5}$  to  $42 \times 10^{-5}$  SI (Fig. F36). This unit, interpreted as an MTD, is composed of three subunits. The middle unit is characterized by deformed and faulted sediments, whereas the bottom and the top units are less deformed (see “[Lithostratigraphy](#)”).

Different magnetic susceptibility values are present in each subunit.

Lithostratigraphic Subunit IC (58.6–91.31 mbsf) is characterized by a sharp decrease in magnetic susceptibility values and then increasing values to the base of the unit. Nevertheless, between 78 and 87 mbsf, lower values are measured. Lithostratigraphic Subunit ID (91.31–125.8 mbsf) shows higher values of magnetic susceptibility than the general trend of the profile. This correlates with the presence of silty intervals and mud clasts within the mass transport deposit, particularly near the base of the unit (see “[Lithostratigraphy](#)”).

The lowermost part of the profile, corresponding to lithostratigraphic Unit II (125.8–234.5 mbsf), is composed of stacked MTDs (see “[Lithostratigraphy](#)”). Magnetic susceptibility values are more scattered within this unit. Magnetic susceptibilities tend to increase with depth. High values of magnetic susceptibility appear to be related to MTDs, mud clasts, and/or faulted sediments within MTD and silt/sand intervals. Seismic Reflectors S40-1322 and S50-1322 are identified as peaks in magnetic susceptibility.

## Thermal conductivity

Between Cores 308-U1322B-21H and 22H, one thermal conductivity measurement per section was performed. Thermal conductivity values at Site U1322 average 1.15 W/(m·K) and increase with depth in the uppermost 20 m of the sediment column (Fig. F37), as would be expected from the decreasing porosity profile (Fig. F34C).

Below 20 mbsf, the thermal conductivity profile has high variability (0.8–1.35 W/[m·K]), probably resulting from the effect of gas expansion in the cores. At the bottom of lithostratigraphic Unit II, the thermal conductivity profile stabilizes and decreases gently from 1.18 to 1.1 W/(m·K).

## P-wave velocity

P-wave velocity data from the multisensor track (MST) P-wave logger (PWL) were recorded from near the seafloor to 72.42 mbsf. PWL velocity measurements range from 1478 m/s near the seafloor to 1609 m/s at 60 mbsf (Fig. F38). From the seafloor to 60 mbsf, P-wave velocities increase. From 60 to 70 mbsf, where gas expansion affected measurements, P-wave velocities decrease. Velocities from P-wave Sensors 1 and 2 (PWS1 and PWS2) insertion probes show a similar trend, while the contact probe PWS3 shows slightly higher velocities. Anisotropy within the measured interval is relatively low and centered around a mean value of 0.8%.



## Undrained shear strength

At Site U1322 several extra measurements were performed near lithostratigraphic unit boundaries and in deformed sediments (MTD) and faults. The undrained shear strengths measured by the automated vane shear (AVS) system consistently matched those measured with the penetrometer (Fig. F39B). Peak undrained shear strengths increase downhole from near zero at the top of lithostratigraphic Unit I to ~140 kPa at 200 mbsf (Fig. F39A). As depth increases, the undrained shear strength data become more variable.

MTDs generally have higher undrained shear strengths than undisturbed sediments. The shear strength decreases abruptly with depth at the base of the MTDs as shown at the base of lithostratigraphic Subunit IB (Fig. F39). In contrast, the shear strength only increases gradually with depth at the top of MTDs, as shown at the top of lithostratigraphic Sub-unit IB. There is a particularly abrupt decrease in shear strength (~50 kPa) with depth at the top of lithostratigraphic Unit II (125 msbf) (Fig. F39).

The residual shear strength profile shows high variability (Fig. F39A). Overall, a linear trend is observed from 0 kPa at the top of lithostratigraphic Unit I to ~40 kPa at 200 mbsf. The profile is similar to that of the peak undrained shear strength, with higher values in slump deposits and lower values in non-slumped deposits. The difference between the two is, however, more subtle. Below 200 mbsf residual shear strength values are relatively low (~20 kPa) and show almost no increase with depth. The sensitivity is generally low (~4) with some intermediate values (from 5 to 10) and a few peak values that indicate high sensitivity (Fig. F39C).

In Figure F40A, peak shear strength is plotted and compared with iso-lines of the ratio between peak shear strength and the vertical hydrostatic effective stress ( $\tau_{fu}^{\text{peak}}/\sigma_{vh}'$ ).  $\sigma_{vh}'$  is calculated from the LWD bulk density log and assumes hydrostatic conditions (see “Physical properties” in the “Methods” chapter). The relationship between the ratio lines and peak undrained shear strength gives an indication of the consolidation state of the clay. At Site U1322 peak undrained shear strength is not parallel to a particular ratio line. Within lithostratigraphic Subunits IA and IB, undrained peak shear strength follows the 0.1 ratio line (Fig. F40A). In lithostratigraphic Sub-units IC and ID, the undrained shear strength profile moves in between the lower ratio lines of 0.1 and 0.05. Below that depth undrained shear strength is more variable, with slump deposits having values between the ratio lines of 0.1 and 0.05 and nonslump deposits between 0.05 and 0.25.

## Summary

At Site U1322 the porosity profile (Fig. F34C) decreases relatively rapidly from the seafloor to 30 mbsf and then more gently to the bottom of the borehole. Shifts from the main trend are observed at MTDs. These shifts have a maximum magnitude of 5%, with lower porosities in MTDs than in undisturbed deposits. These porosity changes are mirrored by the bulk density profile (Fig. F34A).

The undrained shear strength increases linearly with depth. A shift of 50 kPa at 125 mbsf is observed at the base of lithostratigraphic Subunit ID, a 30 m thick MTD. Smaller shifts are also observed at the base of each MTD. MTDs typically have higher undrained shear strengths than undisturbed deposits.

From the main trends in porosity (Fig. F34), undrained shear strength (Fig. F40A), and the relation of the shear strength to the hydrostatic vertical effective stress ( $\tau_{fu}^{\text{peak}}/\sigma_{vh}'$ ) (Fig. F40B), it is possible to make some inferences regarding the sediment consolidation state:

- The change in porosity and undrained shear strength at 125 mbsf indicates that lithostratigraphic Unit II is less consolidated than the underlying MTD.
- MTDs tend to be more consolidated. Higher consolidation might result from reformation of the originally loose sediments into a more packed structure by dewatering during the landslide process. This phenomenon has been observed in other areas such as the Amazon Fan (Piper et al., 1997).
- Porosity (Fig. F34) and undrained shear strength (Fig. F40) values at the top of the MTDs do not vary significantly with respect to the undisturbed sediments above. This might imply that dewatering and consolidation preferentially takes place at the base of the slump where shearing is most likely.

## Downhole measurements

The first MWD/LWD hole in the Ursa Basin was Hole U1322A. The primary objectives were to document the vertical and lateral variations in rock properties in the Ursa Basin and to provide key parameters controlling generation of overpressure, rates of sedimentation, and timing of MTDs. The drilling operations proceeded with careful pressure monitoring because of the risk of encountering shallow-water flows by penetrating sand-prone, overpressured sediments (see “Background and objectives”).



## Logging while drilling and measurement while drilling

### Operations

LWD/MWD operations at Hole U1322A began with the initial makeup of the BHA, tool initialization, and calibration. The LWD tools (17.15 cm collars) included the GeoVision Resistivity (GVR) tool, MWD (PowerPulse) tool, Array Resistivity Compensated (ARC) tool, and Vision Density Neutron (VDN) tool. Because of the potential of encountering unstable and overpressured zones, the LWD BHA used in the Ursa Basin sites included a 13.97 cm full-hole (FH) pin bottom connection, 13.97 cm FH boxtop connection, and 9.63 m long jar section above the VDN to aid in removing tools in the event of a collapsed hole. Hole U1322A was spudded at 1330 mbrf (seafloor depth) with an initial pump rate of ~55 gpm and bit rotation of 10 rpm. The bit was jetted to 3.8 mbsf, and the VIT camera was recovered. Drilling proceeded to 200 mbsf at an average ROP of 30 m/h (Fig. F41). Drilling continued with a reduced ROP of 20 m/h below 200 mbsf to avoid exceeding the target depth of 238 mbsf.

### Logging data quality

LWD log quality data are displayed in Figure F41. Borehole conditions were good with a maximum density-derived caliper log (DCAV) of 33 cm at ~35 mbsf. The caliper data below 120 mbsf are close to bit size and only show a slight enlargement (~30 cm) at 200 mbsf. The bulk density correction values vary only minimally from -0.04 to 0.14 g/cm<sup>3</sup> (average = 0.02 g/cm<sup>3</sup>), indicating reliable bulk density measurements.

The depths in mbsf for LWD logs were fixed by identifying the gamma ray signal associated with the seafloor and shifting the logging data according to the seafloor. The gamma ray log pick for the seafloor was at 1330 mbrf. The rig floor logging datum was 10.5 m above sea level.

### Annular pressure while drilling and equivalent circulating density

Pressure within the borehole was monitored during MWD operations (see discussion in “[Array Resistivity Compensated Tool](#)” in “Downhole measurements” in the “Methods” chapter) as annular pressure while drilling (APWD), annular pressure in excess of hydrostatic (APWD\*), and equivalent circulating density referenced to the seafloor (ECD<sub>rf</sub>) (Fig. F42). ECD<sub>rf</sub> decreases from the top to the bottom of the borehole. APWD\* increases slightly with depth to the bottom of the borehole, indicative of a grad-

ual increase in pressure that is necessary to overcome pipe friction (or wall drag). There is no record of shallow-water flow into the borehole. The ECD<sub>rf</sub> and APWD\* logs vary systematically below 120 mbsf.

### Results

LWD/MWD operations in Hole U1322A reached 238 mbsf without encountering any major sand units. Hole quality was good (average diameter = 26.9 cm) for most of the borehole, and caliper measurements are only slightly increased above 40 mbsf (Fig. F43). These increased caliper values correlate with low gamma ray data, suggesting an increased silt/sand content in the sediments. However, gamma ray measurements have near-constant values of ~70 gAPI throughout the borehole. This is only interrupted at ~215 mbsf, where gamma radiation increases to 90 gAPI. This increase is not reflected in resistivity, which remains relatively monotonous throughout the borehole. The only notable resistivity increase, from ~1 to ~3.5 Ωm, occurs at 160 mbsf.

Bulk density increases from 1.0 to 1.6 g/cm<sup>3</sup> at shallow depths and then increases gradually to 2.0 g/cm<sup>3</sup> at the bottom of Hole U1322A. This corresponds with the decrease in neutron porosity from 83% to 43%. These trends are also observed in the photoelectric factor (PEF) values and imply similar material throughout the borehole.

### Core-log-seismic integration

LWD observations are linked to seismic data through a time-depth conversion constructed from regional check shot data collected prior to Expedition 308 ([Equation 1](#)). The TWT from sea level is related to  $t_{bsf}$  by adding  $t_{bsf}$  to the TWT from sea level to the seafloor (1.766 s) (Table T1) as picked on high-resolution seismic data.

The synthetic seismogram for Hole U1322A was constructed using LWD density data (Fig. F44). Reflection coefficients were calculated using LWD density data and a constant compressional wave velocity of 1600 m/s. A 200 Hz minimum-phase Ricker wavelet was convolved with the reflection coefficients to create the synthetic seismogram. The correlation between the synthetic seismogram and the high-resolution seismic data matches from 0 to 100 mbsf. A time-depth mismatch occurs at seismic Reflector S30 and continues to seismic Reflector S50-1322, where the synthetic reflections occur slightly shallower than the same events in the high-resolution seismic data (Fig. F44). Nevertheless, the overall quality of the time-depth model allows an approximate correlation of seismic reflections with observations in core and log data.



LWD logs display subtle variations throughout the borehole, and the strongest contrast is observed in resistivity and gamma ray logs. These correspond to seismic Reflectors S10 and S30 and support the definition between lithostratigraphic Subunits IA and IB and lithostratigraphic Units I and II (Fig. F43). Seismic Reflector S10 also correlates with small decreases in resistivity and gamma ray within a silt interval, suggesting that increased sand content creates the acoustic impedance contrast. Although seismic Reflector S30 corresponds to low resistivity, the gamma ray contrast is less prominent. The largest variations in log responses occur from the seafloor to ~35 mbsf, which correspond to lithostratigraphic Subunit IA. This unit consists of intercalated layers of clay, foraminifer-bearing layers, and silt. These variations are identified in the LWD data and allow extrapolation between core and seismic observations.

### GeoVision resistivity imaging

Resistivity images of Hole U1322A are of good quality and allow identification of several structures (Figs. F45, F46). Based on visual core descriptions, Hole U1322B was divided into lithostratigraphic Units I and II, which are dominated by clay with occasional interbedded silt units (see “[Lithostratigraphy](#)”). These units are further divided into subunits that reflect the occurrence of either undisturbed or contorted and faulted sediments. Lithostratigraphic Subunit IB was characterized as an MTD with small faults, folded beds, and steep dipping surfaces; these features are also imaged by the GVR data (Fig. F45). Diversely sized high- and low-resistivity oval-shaped patches likely represent the hinge line of these folds. The resistivity contrasts are the result of cutting through layers of different resistivity composing the fold. These folds are clearly revealed by mirrored sinusoids centered on an oval-shaped area of high or low resistivity, depending on the imaged material.

Lithostratigraphic Subunit IB contains several reverse and normal faults. However, these are mostly on the centimeter scale (see “[Lithostratigraphy](#)”) and are problematic to identify in the GVR images. The change between disturbed Subunit IB and laminated Subunit IC is defined by an increase in resistivity (Fig. F45).

East-west-oriented borehole breakouts imaged by the GVR indicate the direction of the minimal horizontal stress (Figs. F45, F46). Consequently, the maximum horizontal stress direction in Hole U1322A is north-south. However, Ursula Basin slopes to the southeast, and it remains unclear if these breakouts are the expression of the local or regional stress field. Similar to Subunit IB, lithostratigraphic Unit II MTDs contain steeply dipping folds and highly disturbed

sediment layers, expressed by variable resistivity (Fig. F46). Horizontal and even bedding of MTDs 2-3 and 2-5 immediately above and below MTD 2-4 are also indicated by resistivity measurements and support the lithostratigraphic division.

## Temperature and pressure measurements

### Advanced piston corer temperature tool

The APCT tool was deployed twice in Hole U1322B (Table T16). Temperature was measured in the sediment for 10 min. The temperature decay curves are extrapolated with an assumed thermal conductivity of 1.2 W/(m·K) to estimate in situ temperatures. The first deployment was at 80.0 mbsf (Core 308-U1322B-9H) and provided an in situ temperature of 6.44°C (Fig. F47). The second deployment (108.5 mbsf; Core 308-U1322B-12H) yielded an equilibrium temperature of 6.56°C (Fig. F48).

### Temperature/Dual Pressure Probe

Eleven deployments of the T2P probe were completed at Site U1322 (Table T16). These measurements provided numerous constraints on in situ temperature and formation pressure.

### T2P Deployment 17

T2P Deployment 17 recorded pressure and temperature increases while penetrating the sediment; however, upon removal of the bit from the bottom of the hole the pressure signals decreased (Table T17; Fig. F49). These pressure decreases were interpreted to reflect pulling the T2P probe tip partly out of the sediment when picking up the drill bit off the bottom of the hole. We interpret that the collected delivery system (CDS) did not completely decouple the drill string from the tool. Thus, when the drill string was raised, it dislodged the probe from the weak formation. The pressures were nearly constant at subhydrostatic after backing off the bit and thus did not provide any constraint on in situ conditions. Hydrostatic pressure is 13.68 MPa. The temperature profile showed a spike associated with penetration and a second spike with backing off the drill bit (Table T17; Fig. F49) followed by a temperature decay. The probe appeared to reach equilibrium with the sediment at 4.90°C.

### T2P Deployment 19

During T2P Deployment 19, the pressure and temperature sensors recorded increases during landing of the CDS in the BHA and during penetration into the sediment (Table T18; Fig. F50). A temperature increase was also observed when the drill bit was picked up from the bottom of the hole. This was coincident with large decreases in tip and shaft pres-



sures. After this decrease, the tip and shaft pressures equilibrated to 15.2 MPa (Fig. F50). The hydrostatic pressure is 14.61 MPa. It was interpreted that picking up the drill string also raised the T2P. It is unclear what the constant pressure of 15.2 MPa represented. Temperature measurements decayed quickly after frictional heating caused by raising the bit. The temperature decayed to a final value of 7.69°C.

### T2P Deployment 20

Pressure and temperature increased during landing of the CDS in the BHA during T2P Deployment 20. However, there was significant noise in the data while landing and while pushing into the formation (Table T19; Fig. F51). This noise resulted from landing the tool with the bit 12 m off the bottom of the hole, then pulling the tool back into the pipe, and then landing the CDS with the bit 3 m off the bottom of the hole. Fluids were circulated during landing of the CDS in the BHA, which also could have created noise. After pushing the tool into the formation and picking up the bit, tip and shaft pressures decreased. The tip then slowly increased to a final value of 15.4 MPa. The shaft pressure was nearly constant at 15.6 MPa. Hydrostatic pressure was 14.84 MPa. The temperature dissipation was smooth after picking up the bit. The equilibrium temperature was 8.31°C.

### T2P Deployment 21

T2P Deployment 21 (Table T20) recorded only 3 min of data. Inspection of the data acquisition unit documented that the memory card was not properly seated; thus, data were not recorded. The memory card was replaced, and the quick-release button for the card was removed. This modification decreased the probability that the memory card could be accidentally ejected during tool assembly or deployment.

### T2P Deployment 22

During T2P Deployment 22 (Table T21) an internal leak flooded the electronics connecting the pressure transducers and the thermistor to the data acquisition unit. This shorted all circuits, and no data were recorded. A leak at an O-ring seal between the drive tube and the drive tube nut caused the malfunction. The poor O-ring seal was the result of the drive tube being out-of-round from damage in a previous deployment. The deformed drive tube was removed from use. All electrical components were cleaned, dried, and tested.

### T2P Deployment 23

Temperature and pressures increased with landing of the CDS in the BHA and with penetration into the

formation during T2P Deployment 23 (Table T22; Fig. F52). The tip pressure decreased when the bit was picked up and then gradually increased to a final pressure of 14.4 MPa. The shaft pressure decreased when the bit was pulled up and then dissipated to 15.4 MPa. Hydrostatic pressure was 14.76 MPa. After initial frictional heating, the temperature decayed to an equilibrium value of 8.07°C.

### T2P Deployment 24

While landing the CDS in the BHA during T2P Deployment 24, pressures and temperature increased. Increases also occurred when the tool was pushed into the formation (Table T23; Fig. F53). Pressure and temperature dissipated while the tool was in the formation. The tip pressure reached a final pressure of 15.8 MPa and the shaft pressure decreased to 17.3 MPa. The hydrostatic reference is 15.26 MPa. The temperature profile decreased to a final value of 8.81°C.

### T2P Deployment 25

Similar to previous shallow deployments, pressure and temperature increased during T2P Deployment 25 when the probe was pushed into the formation, and then pressure dropped rapidly when the drill bit was picked up (Table T24; Fig. F54). The tip and shaft pressures then rapidly equilibrated at 13.5 and 13.6 MPa, less than hydrostatic (13.65 MPa). The temperature decreased rapidly while picking up the bit, after which temperature was nearly constant at 4.93°C. The pressure and temperature measurements suggest that the probe was not in good communication with the formation after picking up the bit; measurements may have been influenced by communication with fluid at the bottom of Hole U1322D.

### T2P Deployment 26

Pressure and temperature data increased during penetration of the tool into the formation during T2P Deployment 26 (Table T25; Fig. F55). Tip and shaft pressures dropped when the bit was picked up and then were nearly constant at 13.7 and 13.8 MPa. Hydrostatic pressure was 13.95 MPa. Pressure and temperature perturbations occurred around 0727 h (Fig. F55) but were not related to deployment activities (Table T25). The temperature profile decreased rapidly and showed multiple step increases and decreases before reaching a final temperature of 5.31°C.

### T2P Deployment 27

Penetration of the probe into the formation created pressure and temperature increases during T2P Deployment 27 (Table T26; Fig. F56). After picking up



the bit, the tip pressure rapidly decreased to a near-constant value of 14.0 MPa, which is less than hydrostatic pressure (14.25 MPa). The shaft pressure dissipated to a final value of 14.6 MPa. Smooth temperature decay was recorded. The final temperature ( $6.79^{\circ}\text{C}$ ) was assumed to be in equilibrium with the formation.

### T2P Deployment 28

T2P Deployment 28 had large pressure and temperature increases with penetration and pressure drops associated with picking up the bit (Table T27; Fig. F57). Pressures at the shaft and tip were near constant at 14.2 and 14.3 MPa after picking the bit up. Hydrostatic pressure was 14.60 MPa. Temperature decayed to a formation temperature of  $6.95^{\circ}\text{C}$ .

Data recording stopped during recovery of the probe. Inspection of the tool revealed that the tip broke and the drive tube bent during deployment. Damage to the probe likely occurred while pushing into the formation, and then the tip was broken when pulling out of the formation. The tool then would have flooded and data recording stopped. Because of the damage during deployment, the end pressure and temperature records should be interpreted with caution.

### Davis-Villinger Temperature-Pressure Probe

Five DVTTP deployments were completed at Site U1322 (Table T16) to provide additional constraints on formation pressure and temperature. Similar to the T2P data, the DVTTP provided multiple temperature measurements but only a few reliable pressure measurements.

### DVTTP Deployment 16

Temperature and pressure increased during DVTTP Deployment 16 penetration (Fig. F58). The pressure then decreased rapidly to  $\sim 15.9$  MPa, which is higher than hydrostatic pressure (14.93 MPa). Temperature dropped rapidly and then slowly increased while the tool was in the formation. These data were interpreted to record a system leak and communication with borehole fluids.

### DVTTP Deployment 17

Pressure and temperature responses for DVTTP Deployment 17 were good during penetration and were followed by dissipation (Fig. F59). The pressure dissipated to a final value of 14.8 MPa but had not equilibrated with the formation. Hydrostatic pressure was 14.25 MPa. The temperature equilibrated with the formation at  $7.04^{\circ}\text{C}$ .

### DVTTP Deployment 18

Pressure increased during penetration during DVTTP Deployment 18 and then decreased abruptly when the bit was picked up (Fig. F60). The decrease may have been caused by pulling the tool up when the bit was picked up. The pressure then increased to 16.4 MPa, where the hydrostatic reference was 15.46 MPa. Temperature increased during penetration and then dissipated while the tool was in the formation (Fig. F60). The final temperature was  $9.19^{\circ}\text{C}$ . This may be slightly above in situ conditions, as the temperature was still decreasing.

### DVTTP Deployment 19

Pressure and temperature profiles for DVTTP Deployment 19 showed good penetration and dissipation responses (Fig. F61). Pressure dissipated to 16.6 MPa but had not equilibrated with the sediment, where hydrostatic pressure was 15.64 MPa. Equilibrium temperature was  $9.30^{\circ}\text{C}$ .

### DVTTP Deployment 20

Similar to DVTTP Deployment 19, pressure and temperature responses provided constraints on in situ conditions during DVTTP Deployment 20. After penetration, the pressure dissipated to 16.4 MPa and the temperature dissipated to  $8.96^{\circ}\text{C}$  (Fig. F62). Hydrostatic pressure was 15.01 MPa. The temperature was assumed to be in equilibrium with the formation.

### Temperature and pressure summary

The combined APCT, T2P, and DVTTP tool measurements helped to constrain the temperature and the pressure field at Site U1322. Temperature increased linearly with depth (Fig. F63). A regression of the temperatures provided a thermal gradient of  $26.2^{\circ}\text{C}/\text{km}$ .

The pressure profile at Site U1322 was harder to constrain. Pressure dissipation curves provided maximum estimates of in situ pressure between 100 and 238 mbsf (Fig. F64). Pressure increases with time were also observed at Site U1322. It was believed that these reflect pore fluids equilibrating with a void around the pressure sensor. This void may have been caused when the bit was picked up if the bit movement pulled up the DVTTP or T2P. Incorporation of these increases can also provide a lower bound on formation pressure (Fig. F65). In general, the observations confirmed overpressure at Site U1322.

### Summary

Logging data obtained at Site U1322 provided crucial information about the character of the sediments in this region and their physical properties as summarized below.



- The logging data change at depth is consistent with the core observations between lithostratigraphic Units I and II. Unit I is characterized by alternating laminated silt-clay layers and two MTDs, whereas Unit II has silt and sand alternating with MTDs.
- The main structures observed by GVR data in Hole U1322A are folded beds and steeply dipping surfaces, interrupted by undisturbed laminated units. GVR imaging also supports the division into sub-units (see “[Lithostratigraphy](#)”).
- A synthetic seismogram for Hole U1322A was constructed using the LWD density data. The correlation between the synthetic seismogram and the high-resolution seismic matches only in the uppermost 100 mbsf.
- In situ pressure and temperature measurements constrained the thermal gradient at 26.2°C/km at Site U1322 and documented overpressure.

## References

- Bassinot, F.C., Labeyrie, L.D., Vincent, E., Quidelleur, X., Shackleton, N.J., and Lancelot, Y., 1994. The astronomical theory of climate and the age of the Brunhes-Matuyama magnetic reversal. *Earth Planet. Sci. Lett.*, 126:91–108. [doi:10.1016/0012-821X\(94\)90244-5](https://doi.org/10.1016/0012-821X(94)90244-5)
- Berggren, W.A., Hilgen, F.J., Langereis, C.G., Kent, D.V., Obradovich, J.D., Raffi, I., Raymo, M.E., and Shackleton, N.J., 1995. Late Neogene chronology: new perspectives in high-resolution stratigraphy. *Geol. Soc. Am. Bull.*, 107:1272–1287. [doi:10.1130/0016-7606\(1995\)107<1272:LNCNPI>2.3.CO;2](https://doi.org/10.1130/0016-7606(1995)107<1272:LNCNPI>2.3.CO;2)
- Coleman, J.M., and Roberts, H.H., 1988. Late Quaternary depositional framework of the Louisiana continental shelf and upper continental slope. *Trans.—Gulf Coast Assoc. Geol. Soc.*, 407–419.
- Eaton, L.F., 1999. Drilling through deepwater shallow water flow zones at Ursula. *Proc.—SPE/IADC Middle East Drill. Conf.*, 153–164.
- Hine, H., and Weaver, P.P.E., 1998. Quaternary. In Bown, P.R. (Ed.), *Calcareous Nannofossil Biostratigraphy*: Dordrecht, The Netherlands (Kluwer Academic Publ.), 266–283.
- Jasper, J.P., and Gagosian, R.B., 1990. The sources and deposition of organic matter in the Late Quaternary Pigmy Basin, Gulf of Mexico. *Geochim. Cosmochim. Acta*, 54:1117–1132. [doi:10.1016/0016-7037\(90\)90443-O](https://doi.org/10.1016/0016-7037(90)90443-O)
- Joyce, J.E., Tjalsma, L.R.C., and Prutzman, J.M., 1990. High-resolution planktic stable isotope record and spectral analysis for the last 5.35 m.y.: Ocean Drilling Program Site 625 Northeast Gulf of Mexico. *Paleoceanography*, 5:507–529.
- Kennett, J.P., and Huddlestun, P., 1972. Late Pleistocene paleoclimatology, foraminiferal biostratigraphy, and tephrochronology, western Gulf of Mexico. *Quat. Res.*, 2:38–69. [doi:10.1016/0033-5894\(72\)90004-X](https://doi.org/10.1016/0033-5894(72)90004-X)
- Kvenvolden, K.A., and Barnard, L.A., 1983. Gas hydrates of the Blake Outer Ridge, Site 533, Deep Sea Drilling Project Leg 76. In Sheridan, R.E., Gradstein, F.M., et al., *Init. Repts. DSDP*, 76: Washington (U.S. Govt. Printing Office), 353–365.
- Mallarino, G., Droxler, A.W., Beaubouef, R.T., Abreu, V., and Laberye, L., in press. Sea level influence on the nature and timing of a mini-basin sedimentary fill (northwestern slope of the Gulf of Mexico). *AAPG Bull.*
- Martin, R.E., Johnson, G.W., Neff, E.D., and Krantz, D.W., 1990. Quaternary planktonic foraminiferal assemblage zones of the northeast Gulf of Mexico, Columbia basin (Caribbean Sea), and tropical Atlantic Ocean: graphic correlation of microfossil and oxygen isotope datums. *Paleoceanography*, 5:531–555.
- McAdoo, B.G., Pratson, L.F., and Orange, D.L., 2000. Submarine landslide geomorphology, U.S. continental slope. *Mar. Geol.*, 169:103–136. [doi:10.1016/S0025-3227\(00\)00050-5](https://doi.org/10.1016/S0025-3227(00)00050-5)
- McFarlan, E., and LeRoy, D.O., 1988. Subsurface geology of the Late Tertiary and Quaternary deposits, coastal Louisiana, and the adjacent continental shelf. *Trans.—Gulf Coast Assoc. Geol. Soc.*, 421–433.
- Ostermeier, R.M., Pelletier, J.H., Winker, C.D., Nicholson, J.W., Rambow, F.H., and Cowan, K.M., 2000. Dealing with shallow-water flow in the deepwater Gulf of Mexico. *Proc. Offshore Tech. Conf.*, 32(1):75–86.
- Piper, D.J.W., Pirmez, C., Manley, P.L., Long, D., Flood, R.D., Normark, W.R., and Showers, W.J., 1997. Mass-transport deposits of the Amazon Fan. In Flood, R.D., Piper, D.J.W., Klaus, A., and Peterson, L.C. (Eds.), *Proc. ODP, Sci. Results*, 155: College Station, TX (Ocean Drilling Program), 109–146. [PDF]
- Poag, C.W., 1981. *Ecologic Atlas of Benthic Foraminifera of the Gulf of Mexico*: Stroudsburg, PA (Hutchinson Ross).
- Sawyer, D.E., Flemings, P.B., Shipp, C., and Winker, C., submitted. Seismic geomorphology, lithology, and evolution of the late Pleistocene Mars-Ursa turbidite minibasin, northern Gulf of Mexico. *AAPG Bull.*
- Styzen, M.J., 1996. Late Cenozoic chronostratigraphy of the Gulf of Mexico. *Spec. Publ.—SEPM (Soc. Sediment. Geol.)*, GCS407:1–2.
- Winker, C.D., and Booth, J.R., 2000. Sedimentary dynamics of the salt-dominated continental slope, Gulf of Mexico: integration of observations from the seafloor, near-surface, and deep subsurface. *Deep-Water Reservoirs of the World: Proc. GCSSEPM 20th Annu. Res. Conf.*, 1059–1086.
- Winker, C.D., and Shipp, R.C., 2002. Sequence stratigraphic framework for prediction of shallow water flow in the greater Mars-Ursa area, Mississippi Canyon area, Gulf of Mexico continental slope [22nd Annual GCSSEPM Foundation Bob F. Perkins Research Conference, Houston, TX, 8–11 December, 2002]. (Abstract)

Publication: 8 July 2006  
MS 308-106



**Figure F1.** The Mars-Ursa basin is located 95 km downdip of the Mississippi River on the continental slope. Large box outlines Figure F2. Small box locates Figure F3.

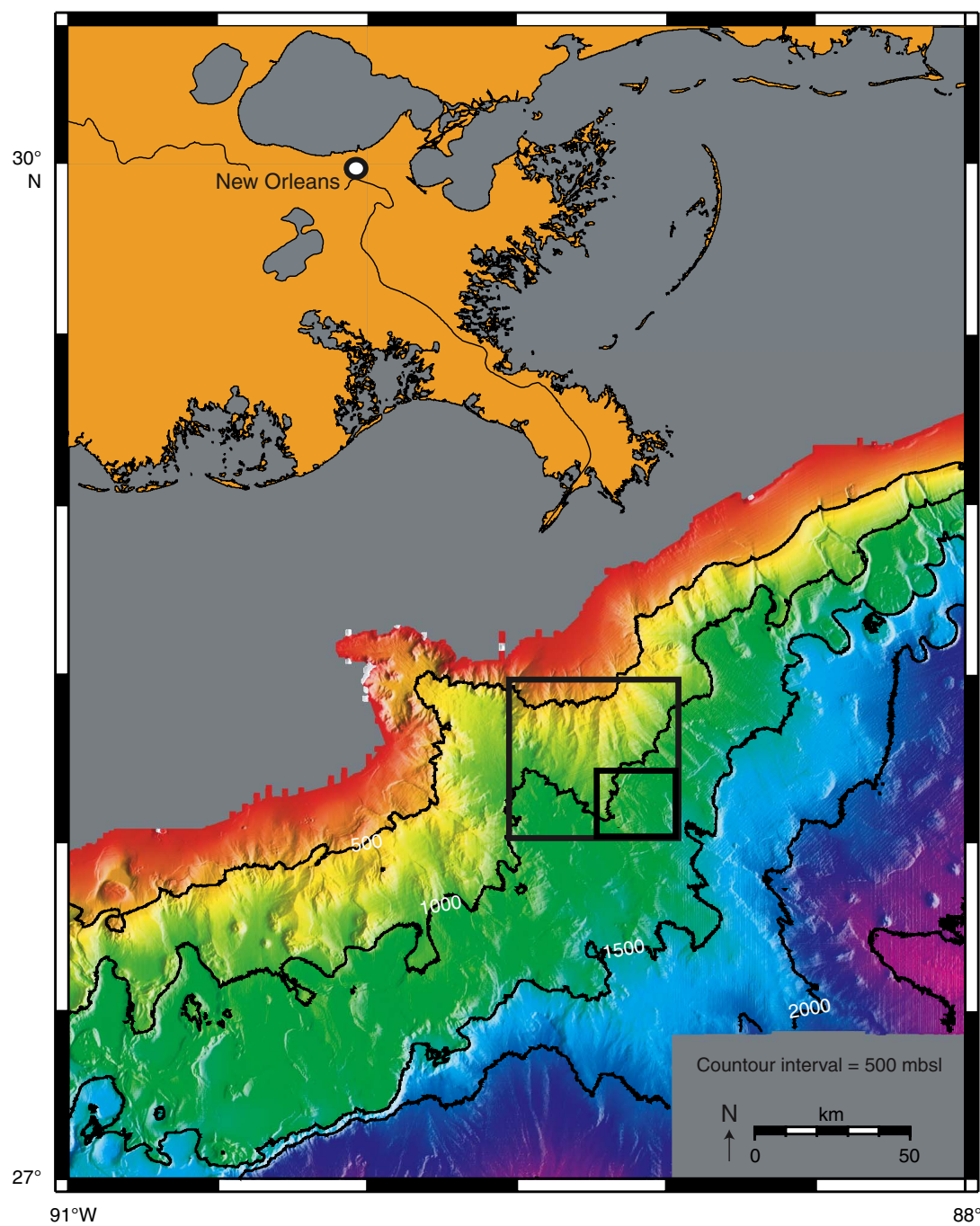


**Figure F2.** Striking bathymetry in the Mars-Ursa region is produced by the thick wedge of Pleistocene sediments from the Mississippi River. Mars Ridge is the bathymetric expression of a buried Pleistocene channel-levee system. Location of map is shown in Figure F1. Box locates Figure F3.

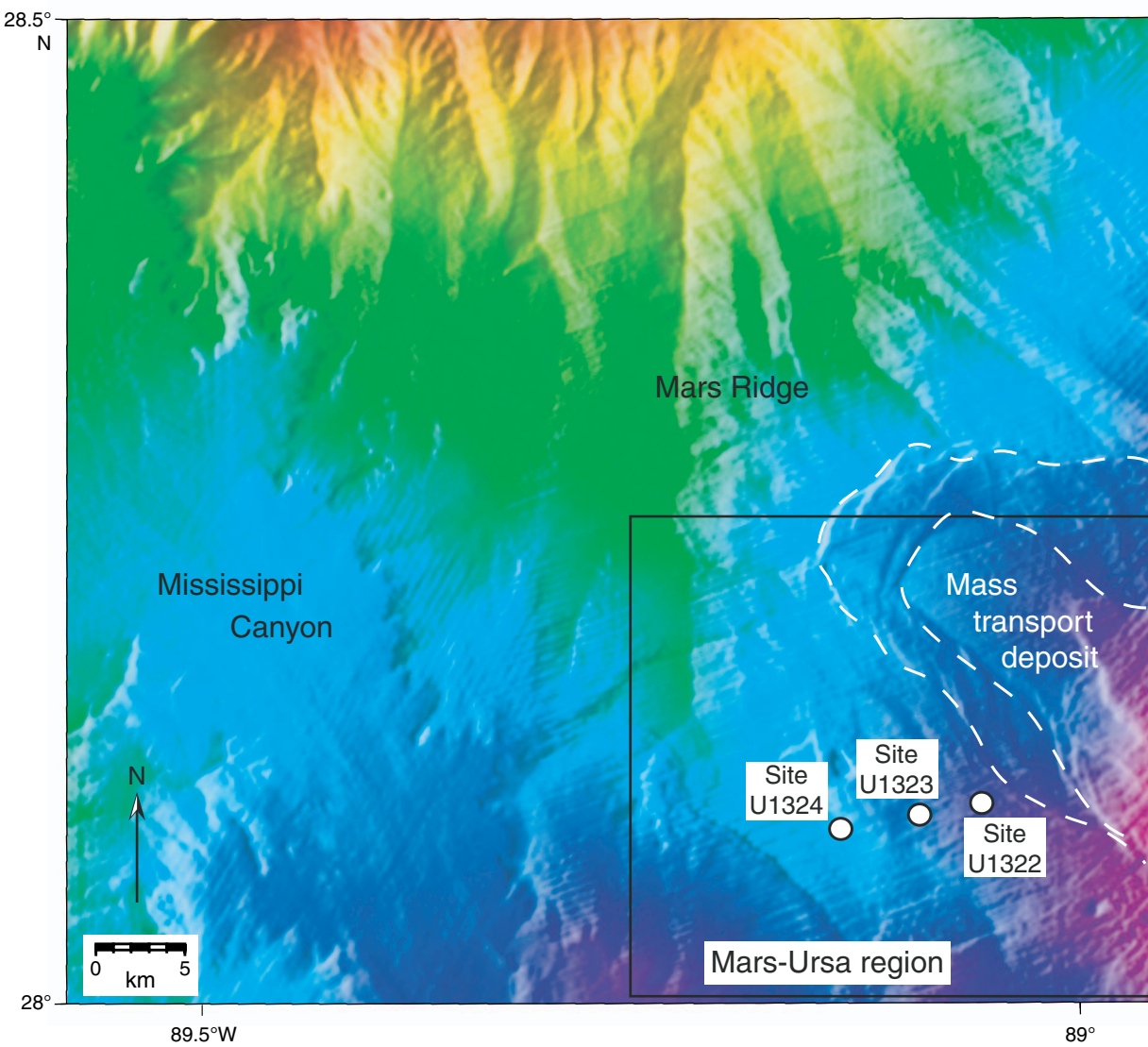


**Figure F3.** Base map of the Mars-Ursa study area with location of seismic data, well locations, and bathymetry contours. Contour interval = 200 m. Figure is located in Figure F1.

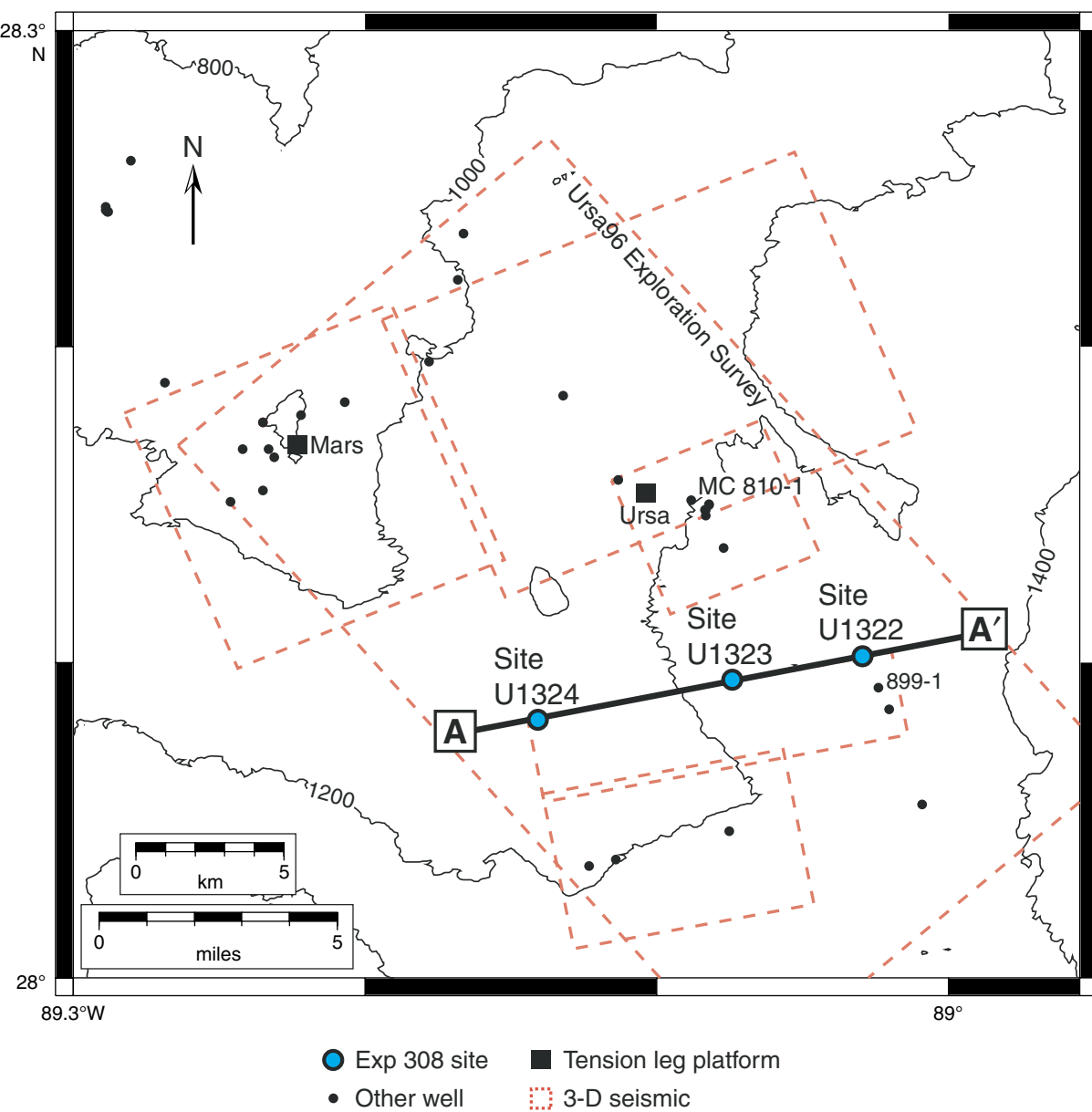


**Figure F4.** A. Seismic cross section A–A' (located in Fig. F3). B. Interpreted cross section A–A' showing main depositional elements and key surfaces. The Ursa Canyon channel-levee system and Southwest Pass Canyon channel-levee system eroded and buried the Blue Unit basin-floor fan. Mass transport deposits (MTDs) have occurred on the flanks of the channel levees. Vertical exaggeration in both figures = ~10.

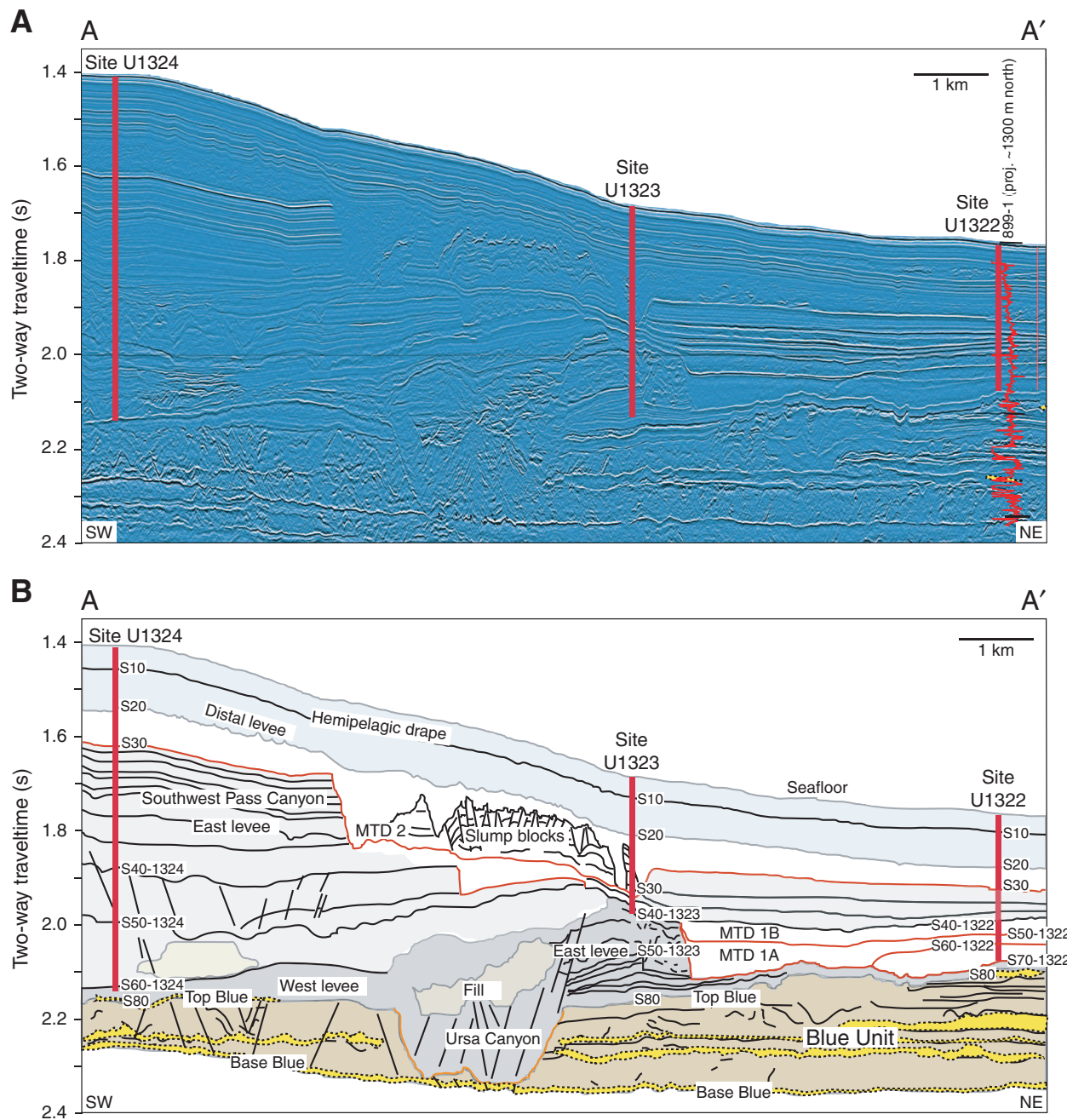
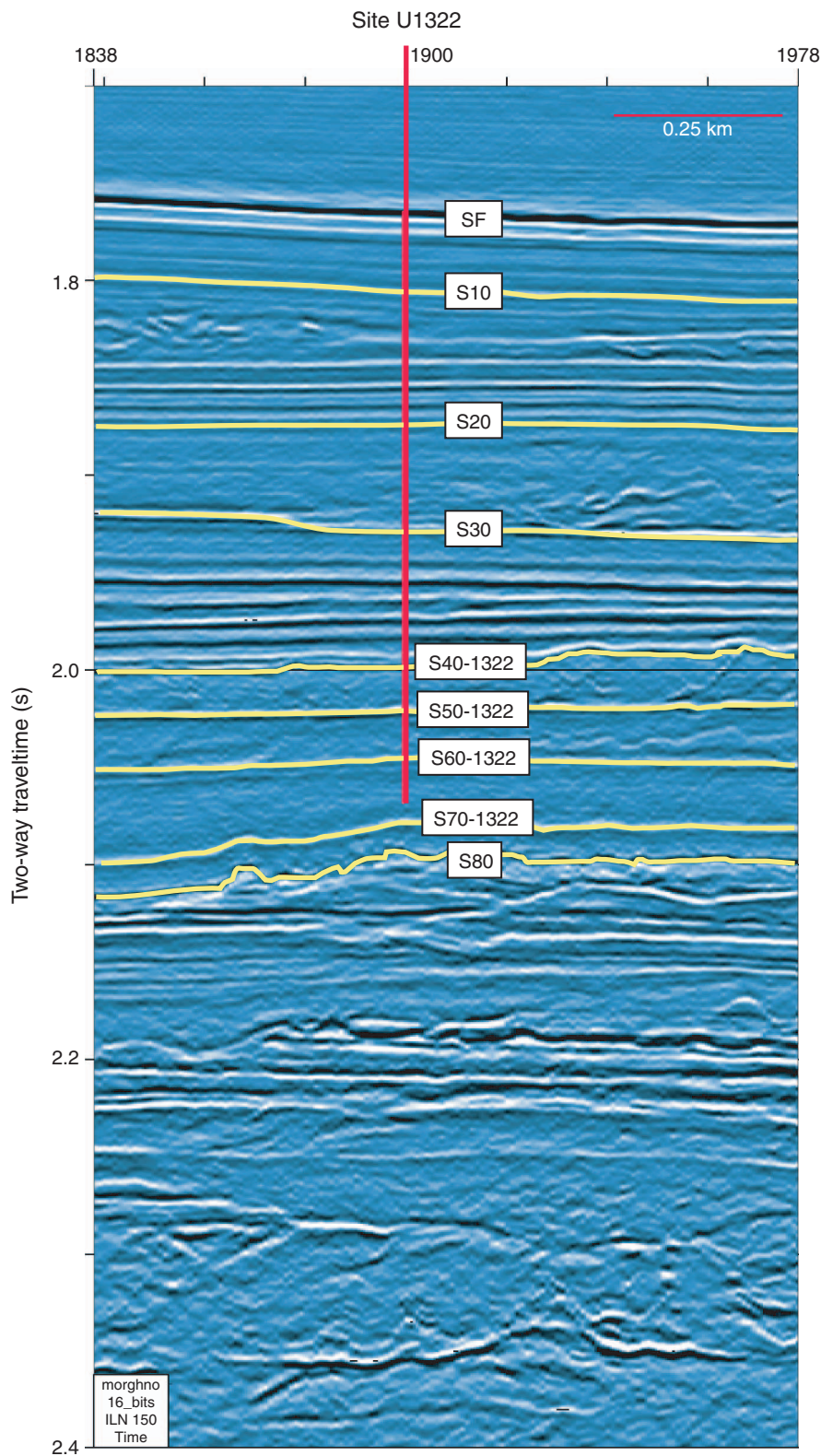
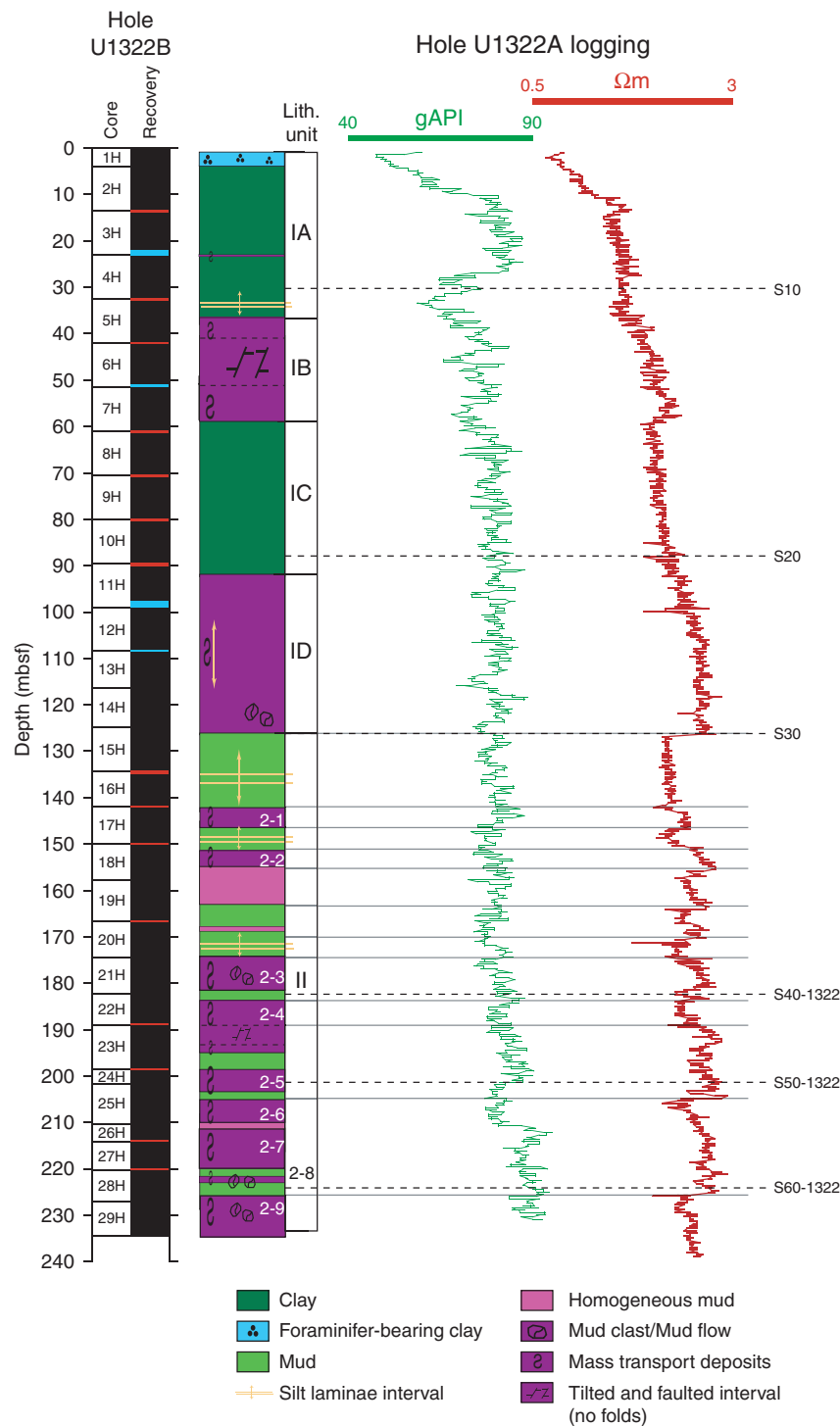


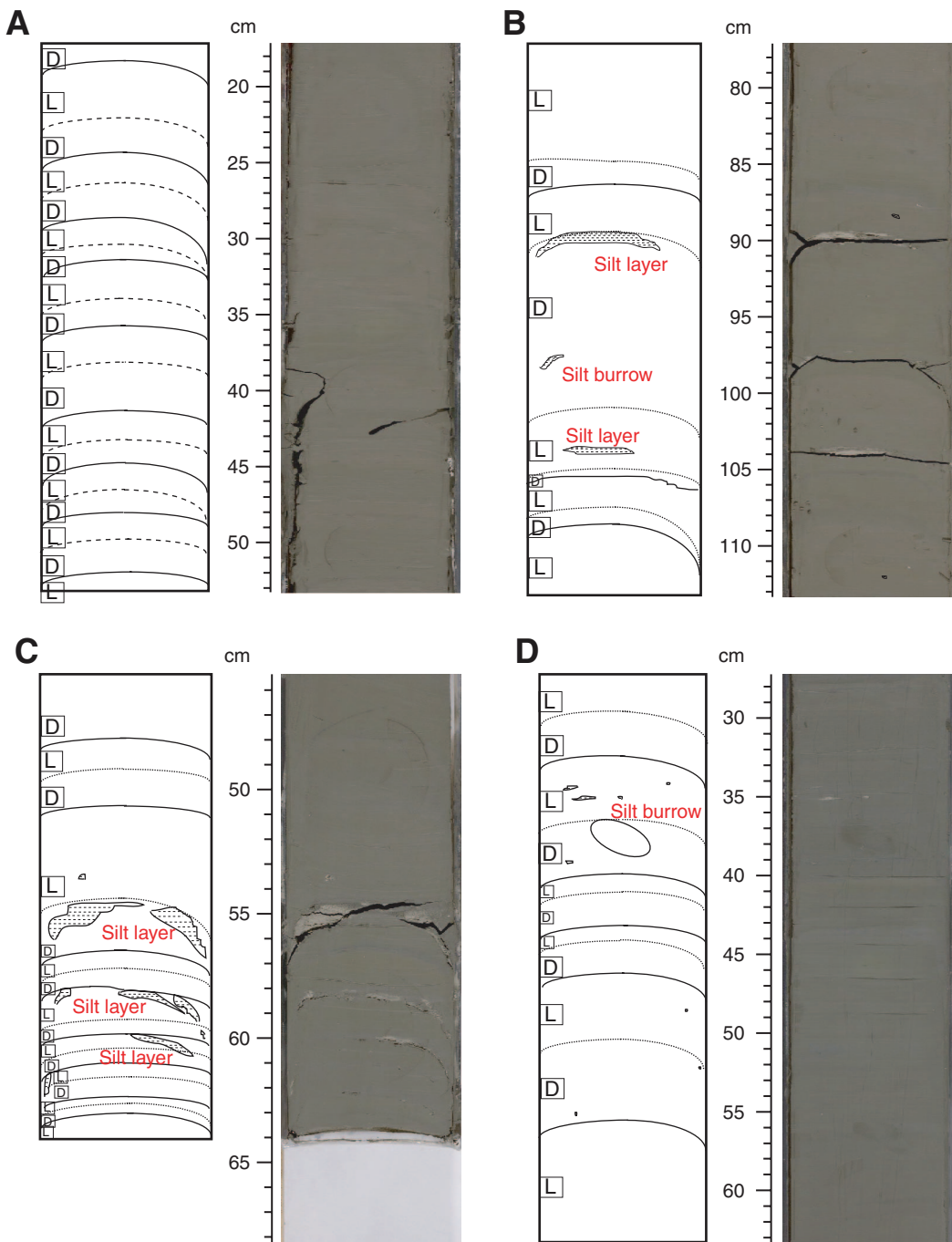
Figure F5. East-west-oriented seismic strip chart, Site U1322. SF = seafloor.



**Figure F6.** Summary of lithostratigraphy and well log measurements at Site U1322. Data columns include core recovery; summary of lithology and structural observations in core (2-1 through 2-9 refer to individual mass transport deposits delineated in core) with lithostratigraphic unit boundaries and gamma ray (GR) and resistivity curves.

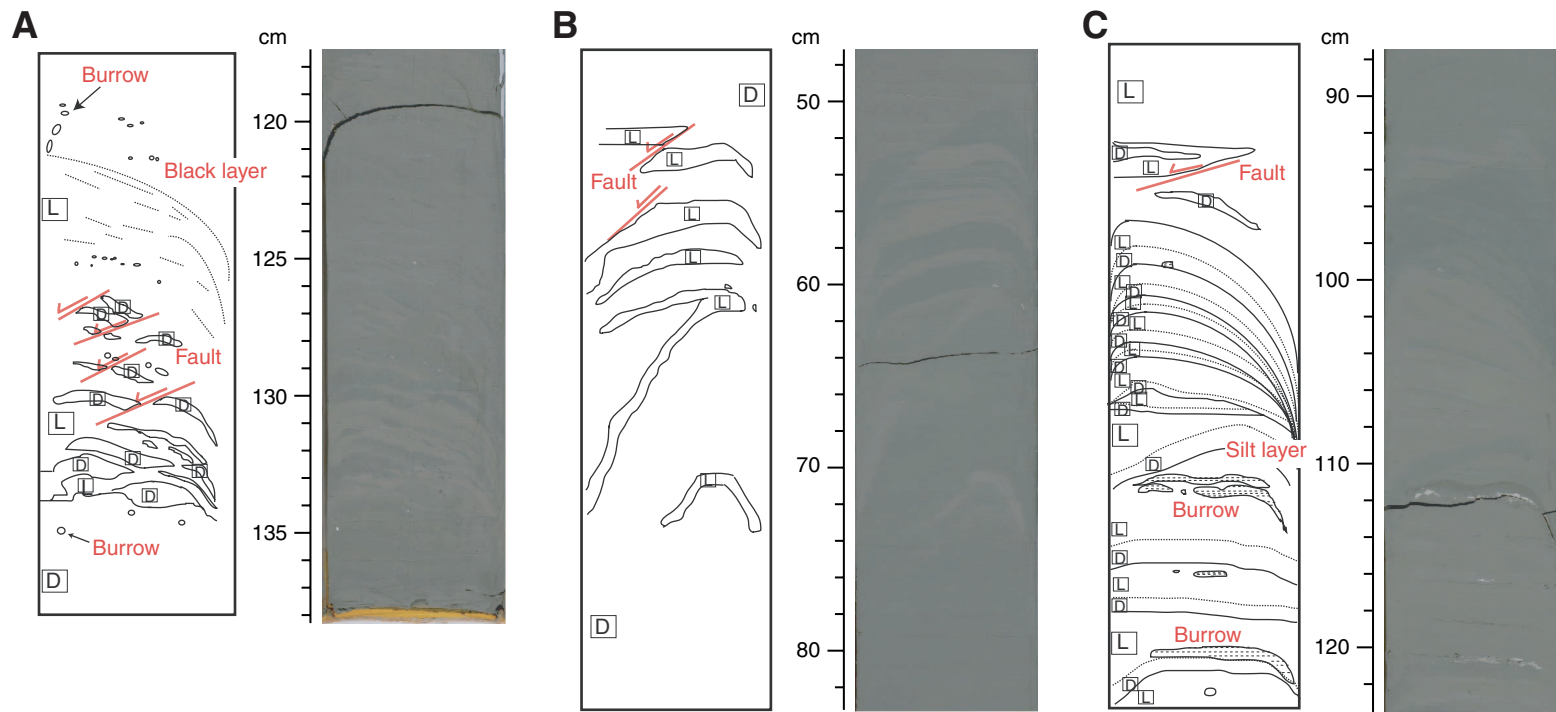


**Figure F7.** Example of dark (D) and light (L) greenish gray banded clay and homogeneous green and brown clay with rare wispy silt laminae in lithostratigraphic Subunit IA. A. Interval 308-U1322B-4H-1, 18–53 cm. B. Interval 308-U1322B-4H-5, 78–113 cm. C. Interval 308-U1322B-4H-7, 45–68 cm. D. Interval 308-U1322B-5H-4, 28–63 cm.

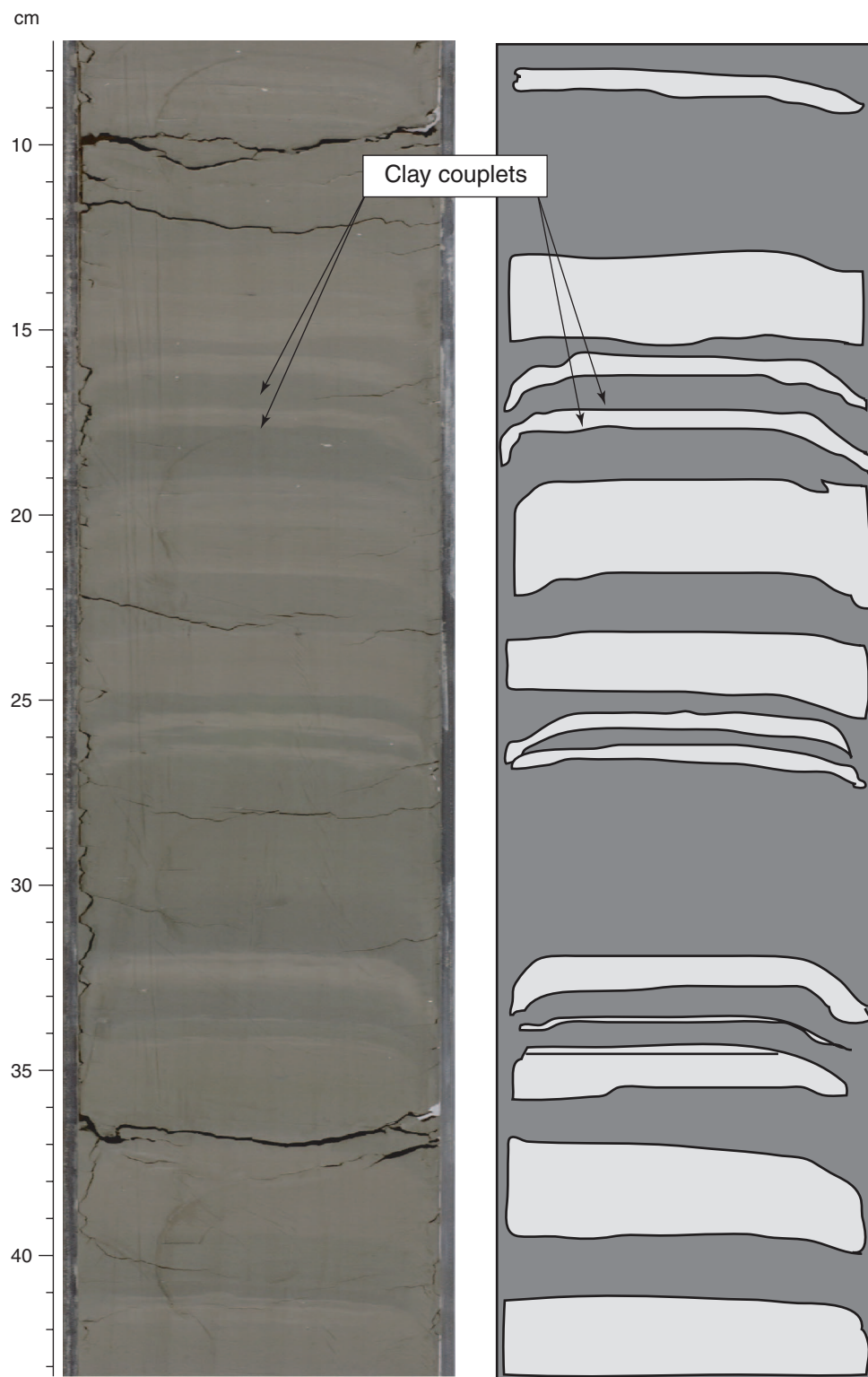




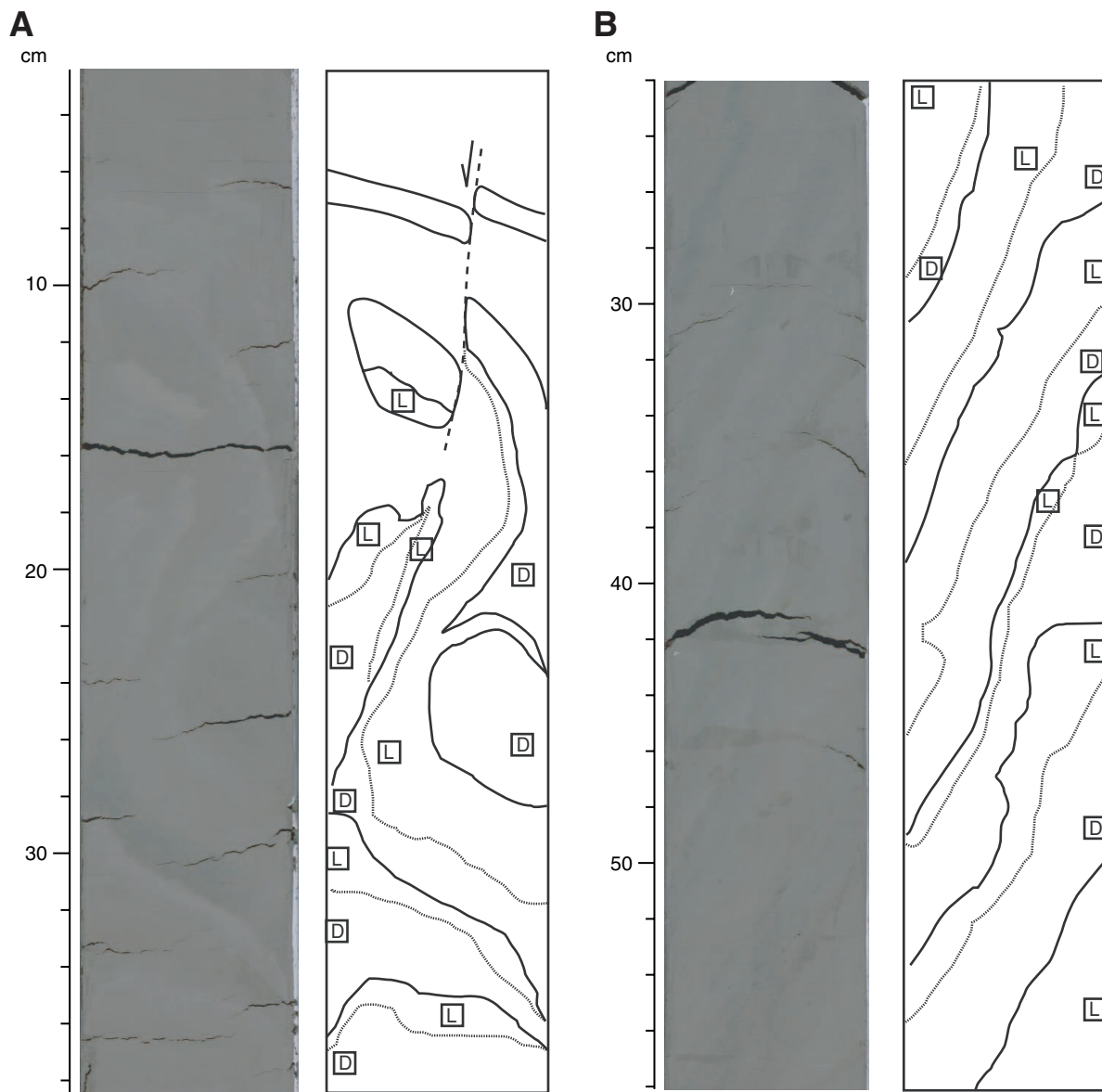
**Figure F8.** Deformed light and dark green clay with silt laminae and specks of silt in lithostratigraphic Subunit IB mass transport deposits. A. Small-scale normal faults (interval 308-U1322B-6H-3, 118–138 cm). B. Interval 308-U1322B-6H-4, 48–82 cm. C. Interval 308-U1322B-6H-4, 88–122 cm.



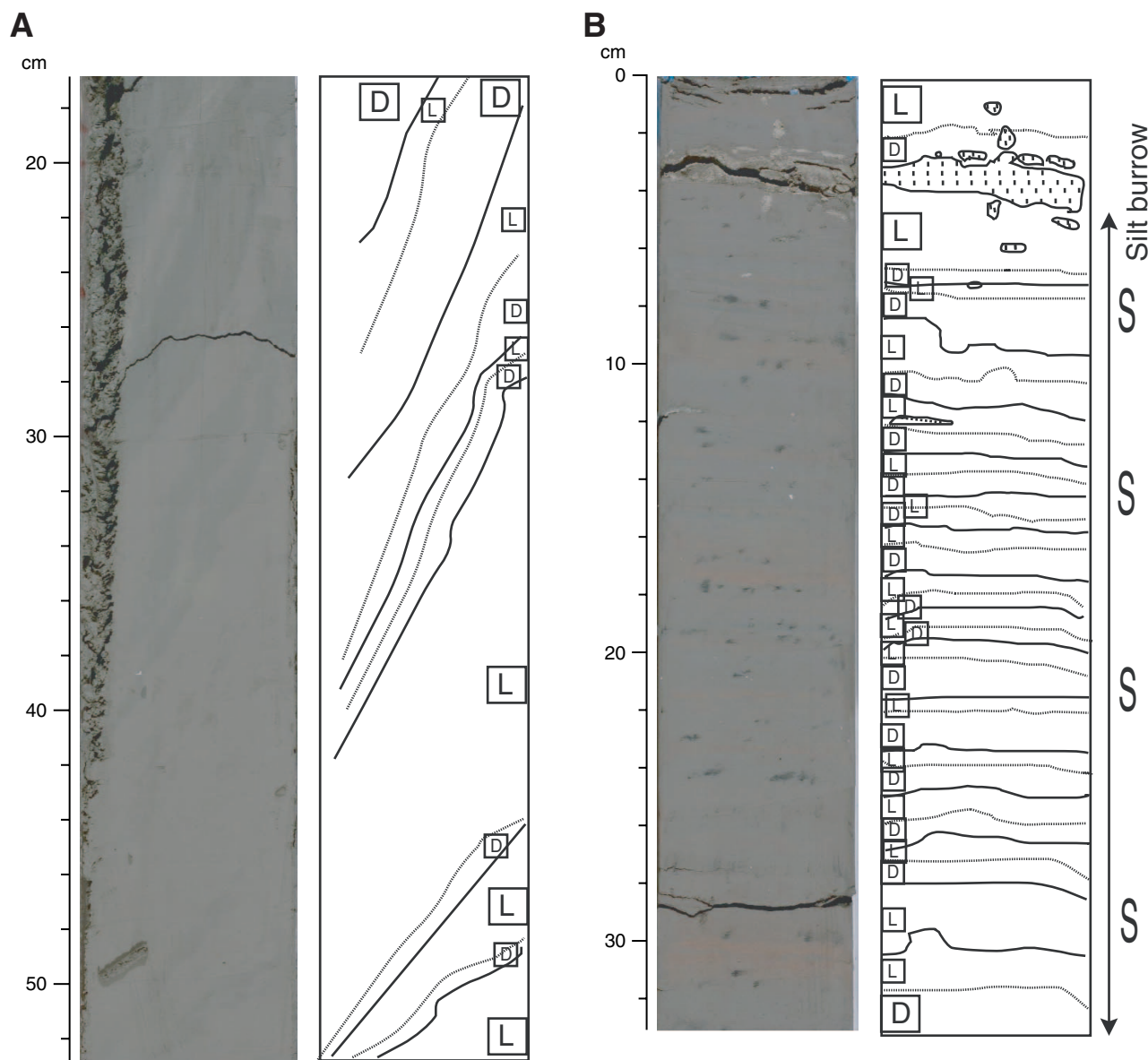
**Figure F9.** Greenish gray and lighter clay couplets in lithostratigraphic Subunit IC (interval 308-U1322B-9H-4, 7–43 cm).



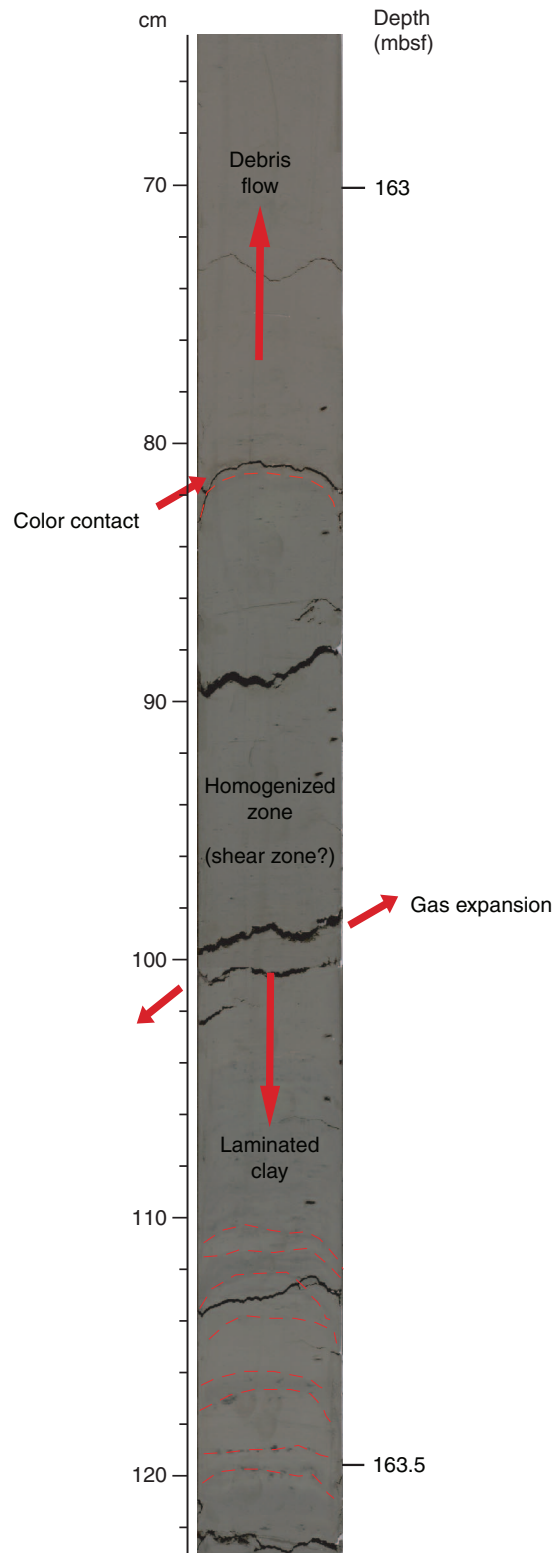
**Figure F10.** Lithostratigraphic Subunit ID mass transport deposits. A. Dark (D) and light (L) greenish gray clay occasionally coupled with blackish clay laminae and dark greenish gray mud showing deformed bedding (interval 308-U1322B-11H-5, 6–38 cm). B. Tilted greenish gray and brownish mud layers alternating with blackish mottled laminae with measured bedding dips of 50°–80°N (see Table T7) (interval 308-U1322B-12H-7, 22–58 cm).



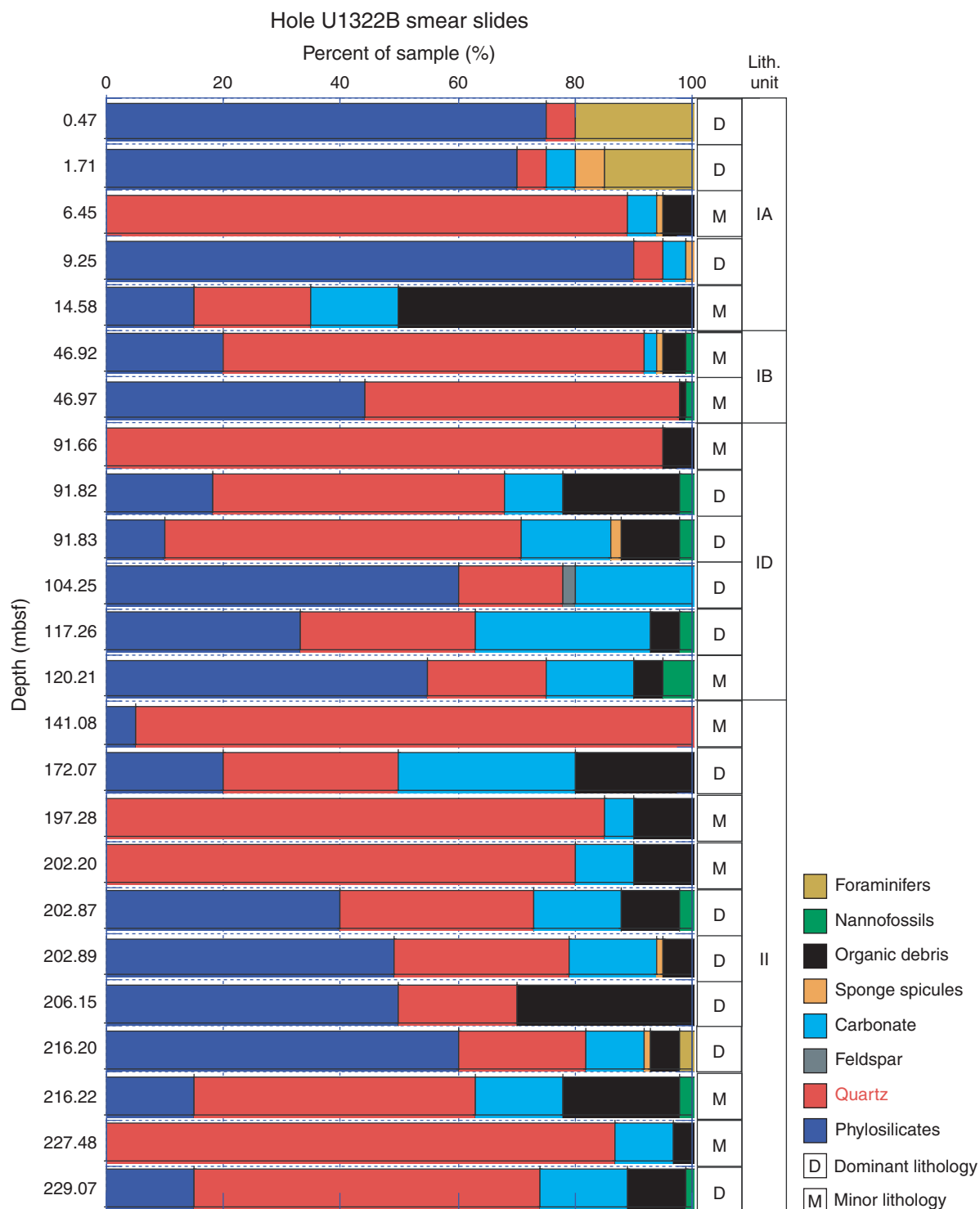
**Figure F11.** Alternating of mass transport deposits with undeformed coherent sediments in lithostratigraphic Unit II. A. Brownish, greenish, and black clay in deformed intervals. Note the tilted layers with an apparent dip of 50°–70° (interval 308-U1322B-17H-1, 18–52 cm). B. Greenish gray mud with reddish brown mottled bands including black specks and bioturbated silt and very fine sand laminae (interval 308-U1322B-20H-4, 0–32 cm).



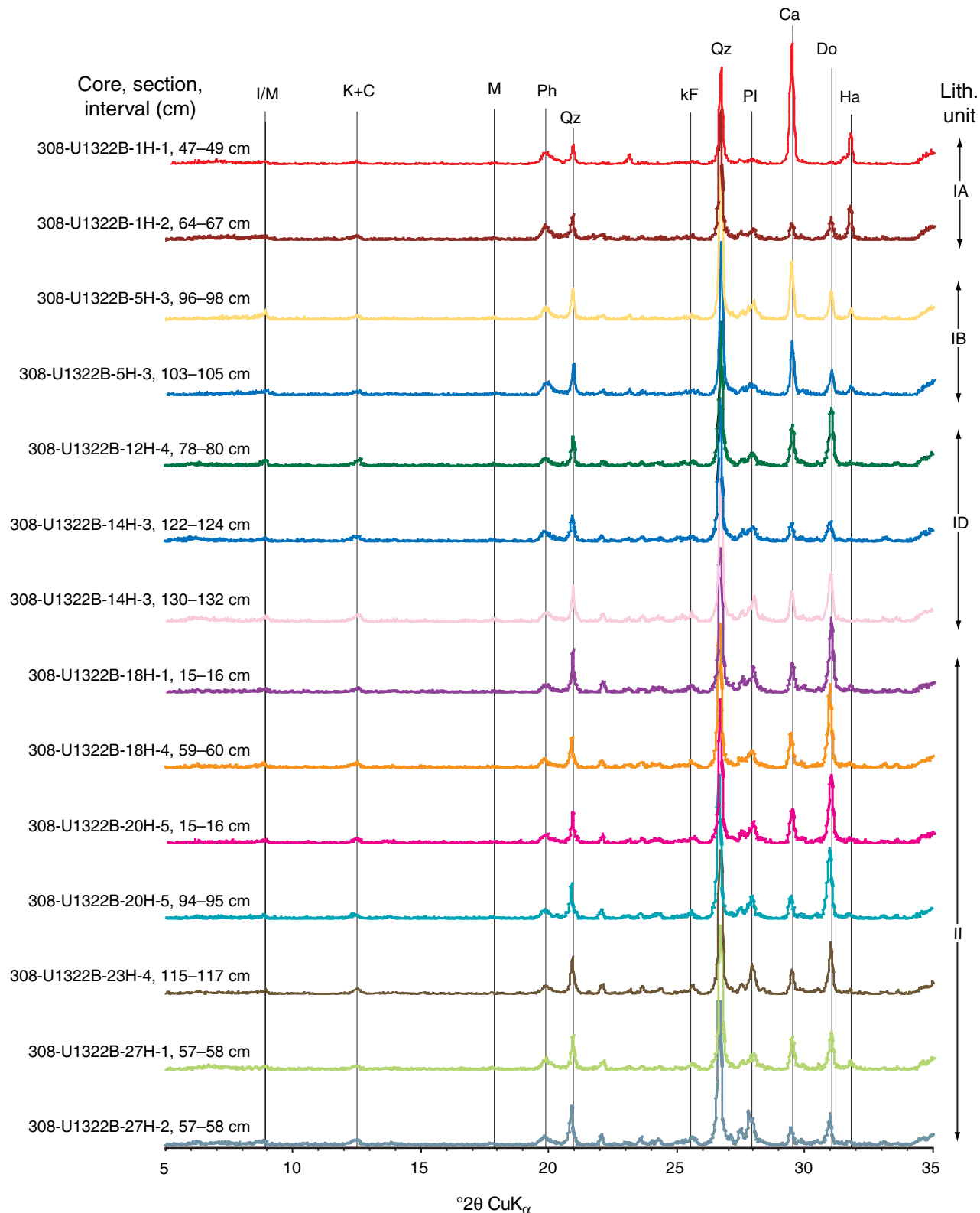
**Figure F12.** Boundary between the homogenized zone below mass transport Deposit 2-2 and coherent layers (Table T7) in lithostratigraphic Unit II. The homogenized zone is composed of brownish mud that may represent a debris flow, and the coherent layers are laminated couplets of clay that represent hemipelagic deposition. A transitional zone of homogeneous greenish mud lies between these zones and is interpreted as a shear zone (interval 308-U1322B-19H-4, 65–122 cm).



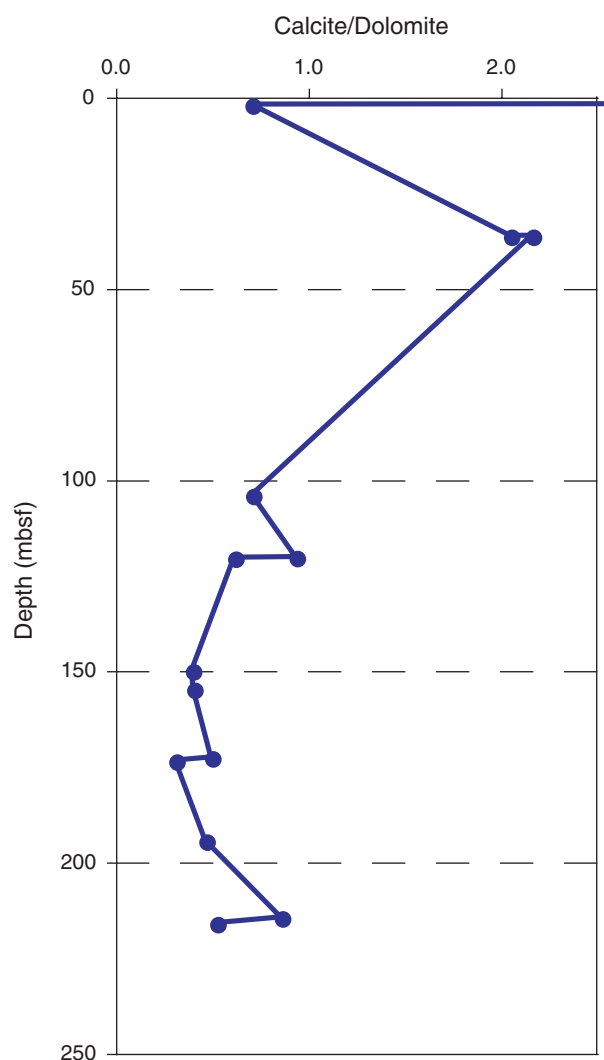
**Figure F13.** Summary of smear slide analysis from Hole U1322B including samples taken in dominant and minor lithologies.



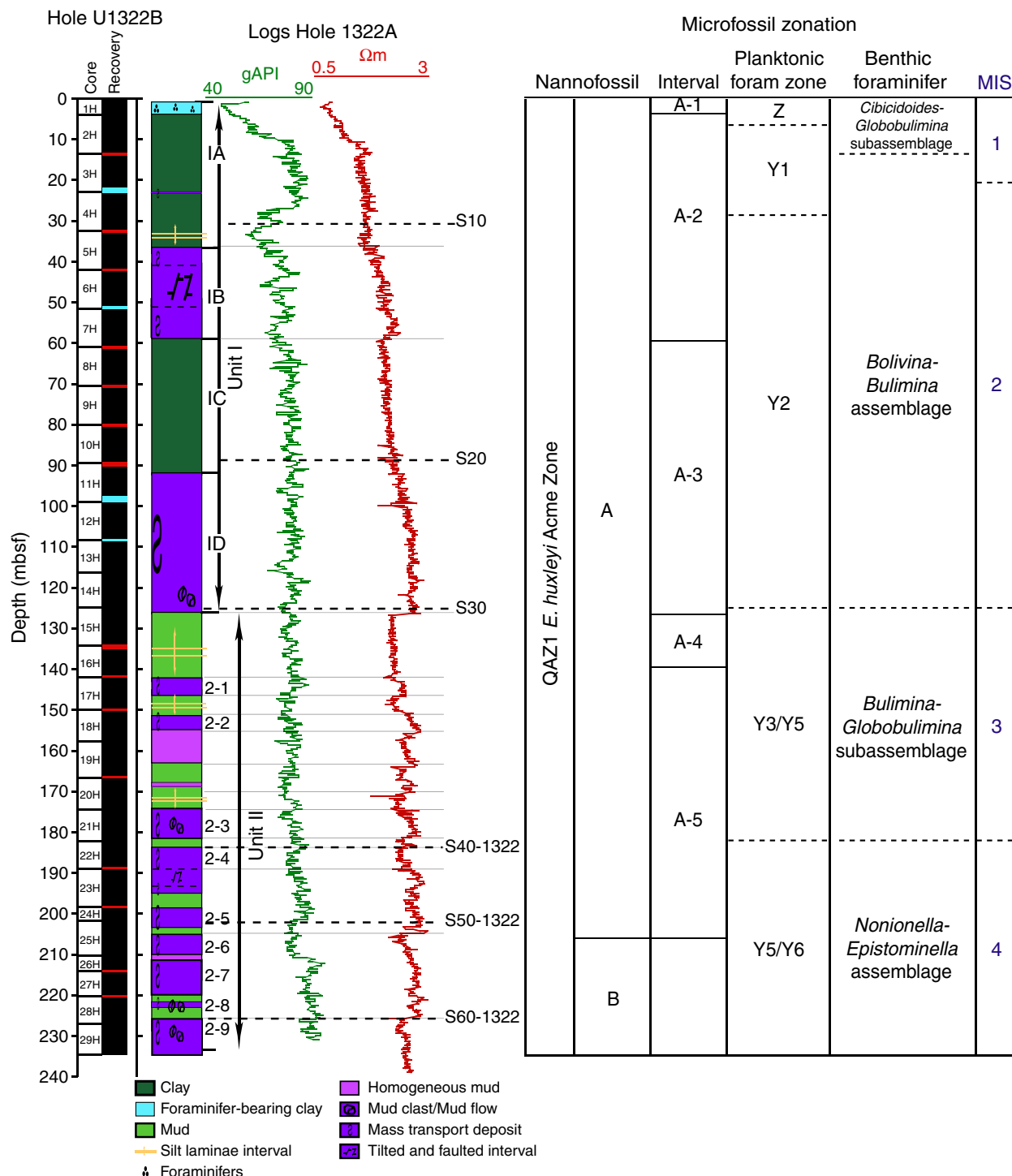
**Figure F14.** Bulk powder X-ray diffractograms of samples from selected intervals in Hole U1322B. All diffractograms have the same vertical scale. Thin vertical lines denote characteristic mineral peaks: I/M = illite/mica, K + C = kaolinite + chlorite, M = mica, Ph = phyllosilicates, Qz = quartz, kF = potassium feldspar, Pl = plagioclase, Ca = calcite, Do = dolomite, Ha = halite.



**Figure F15.** Peak count ratios of calcite/dolomite. First sample at 0.47 mbsf is dominated by calcite (calcite/dolomite = 35.2) and plots outside the selected scale range.

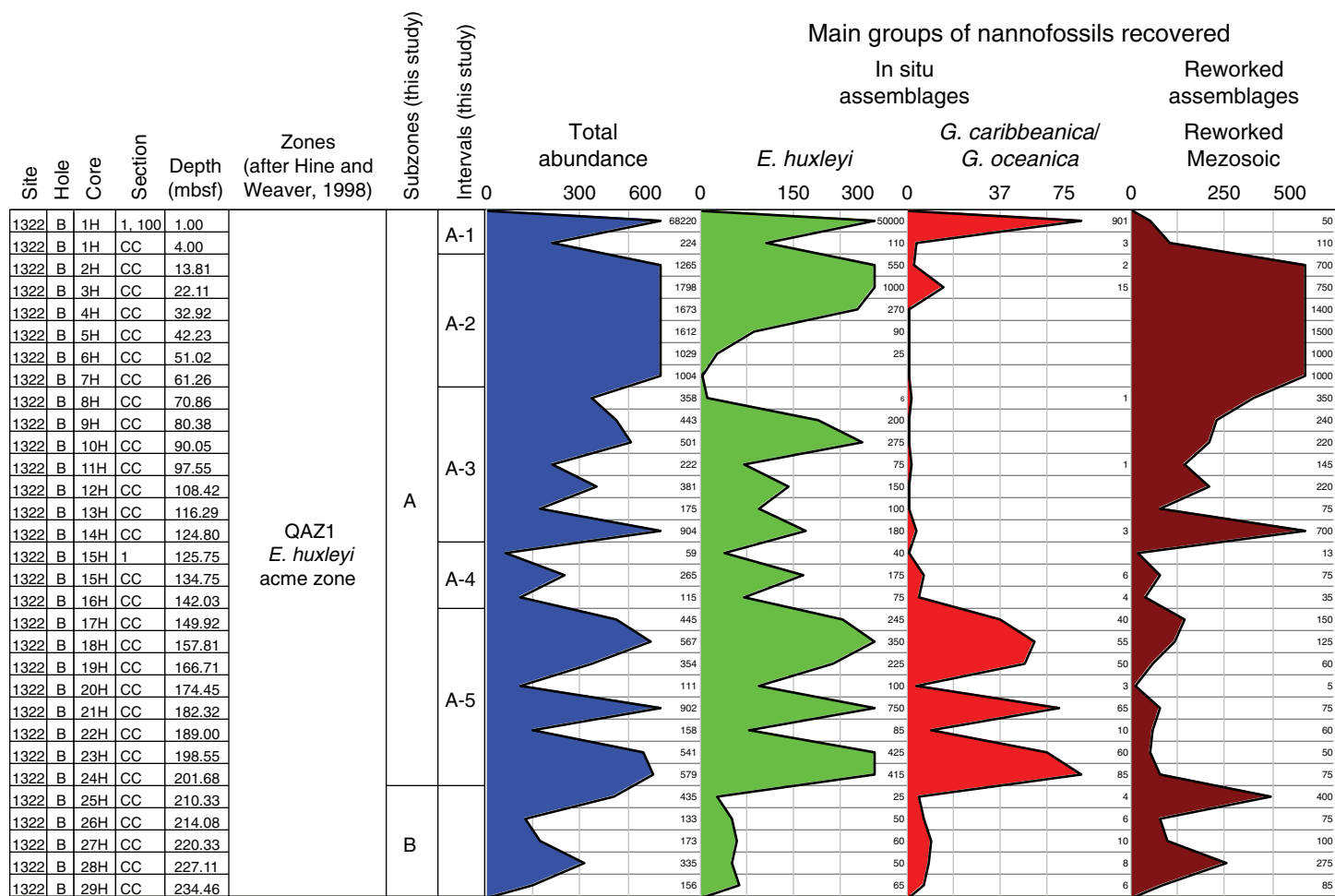


**Figure F16.** Biostratigraphic summary, Site U1322 including nannofossil and planktonic foraminifer zones and benthic foraminifer assemblages, gamma ray resistivity results, seismic reflectors, lithostratigraphy (see “**Lithostratigraphy**” and “**Physical properties**”), and correlation to marine isotope stages (MIS).

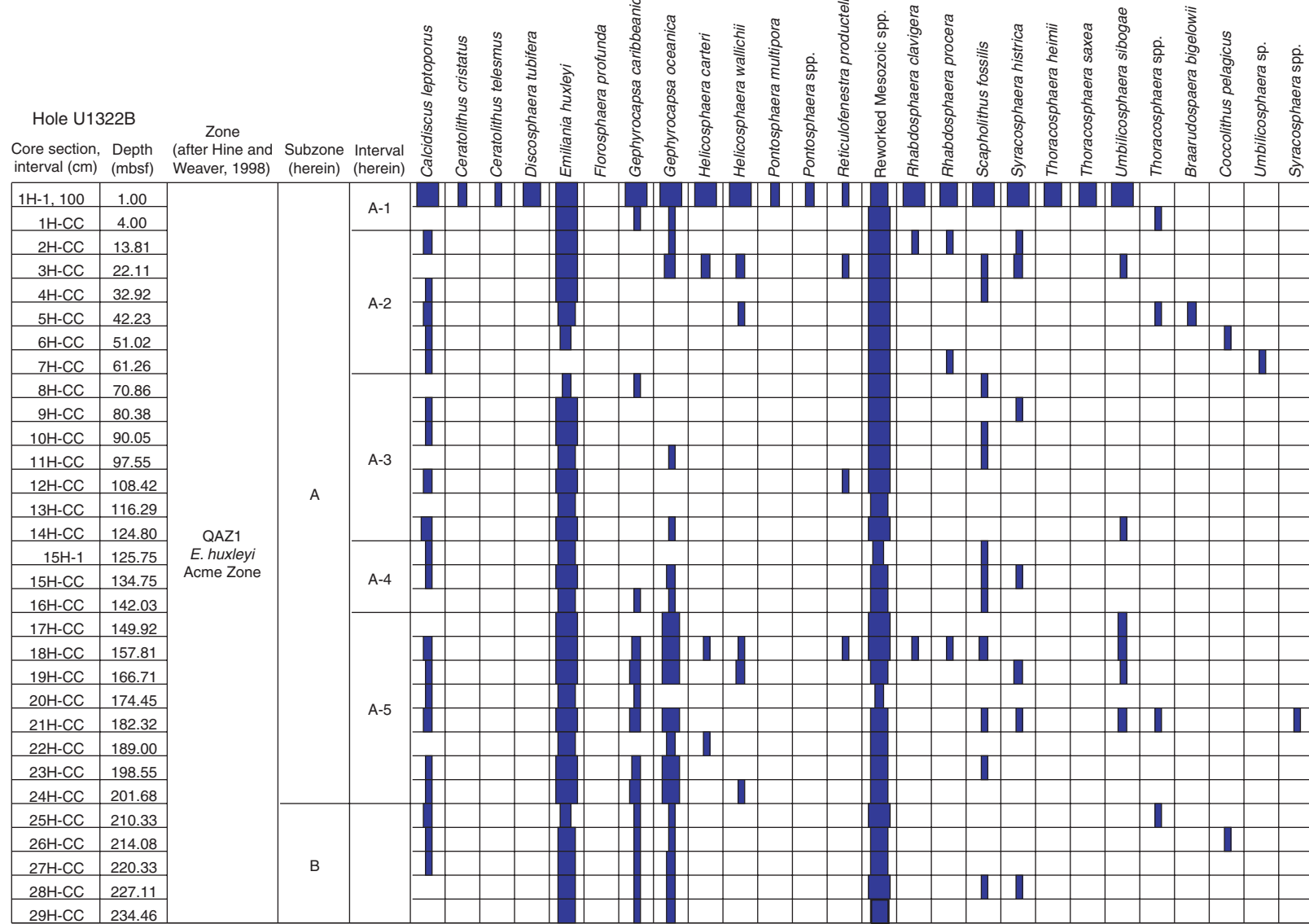




**Figure F17.** Nannofossil zonation for Hole U1322B using the distribution of stratigraphically important nannofossil groups showing relative abundance of total nannofossils and main groups in each sample.

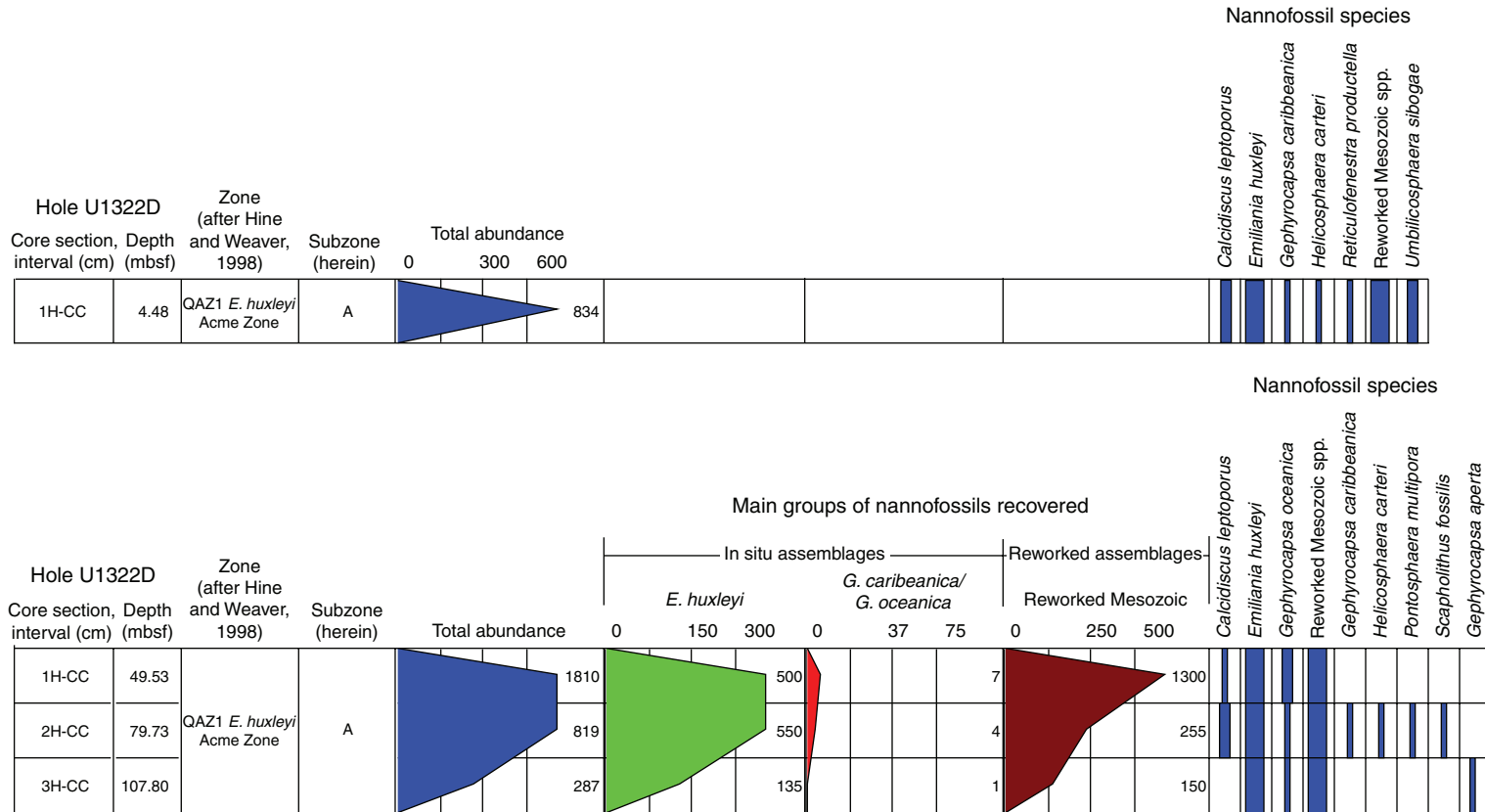


**Figure F18.** General distribution of nannofossils from Hole U1322B, showing the sporadic pattern for most species. Nannofossil zonation is given.

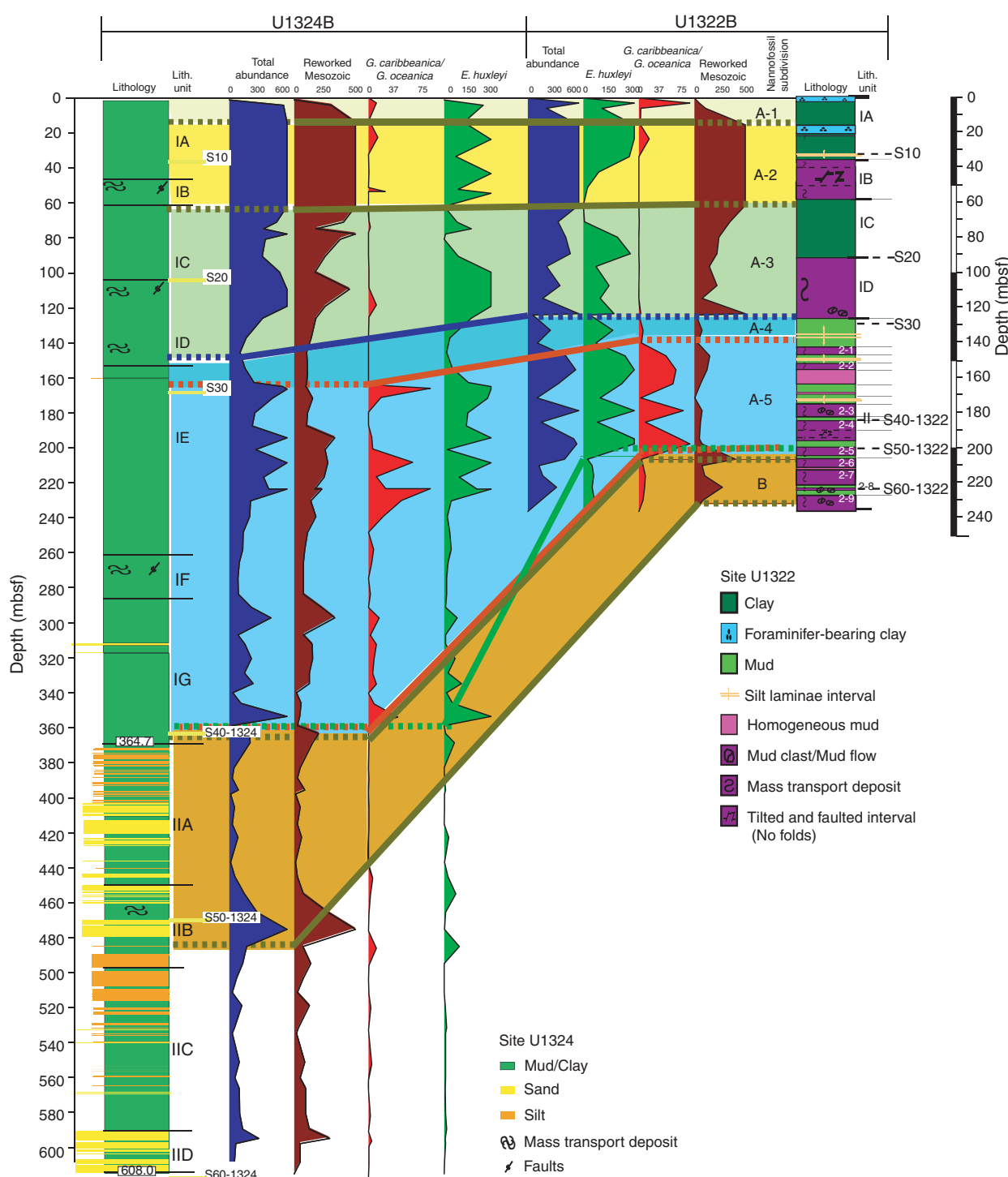




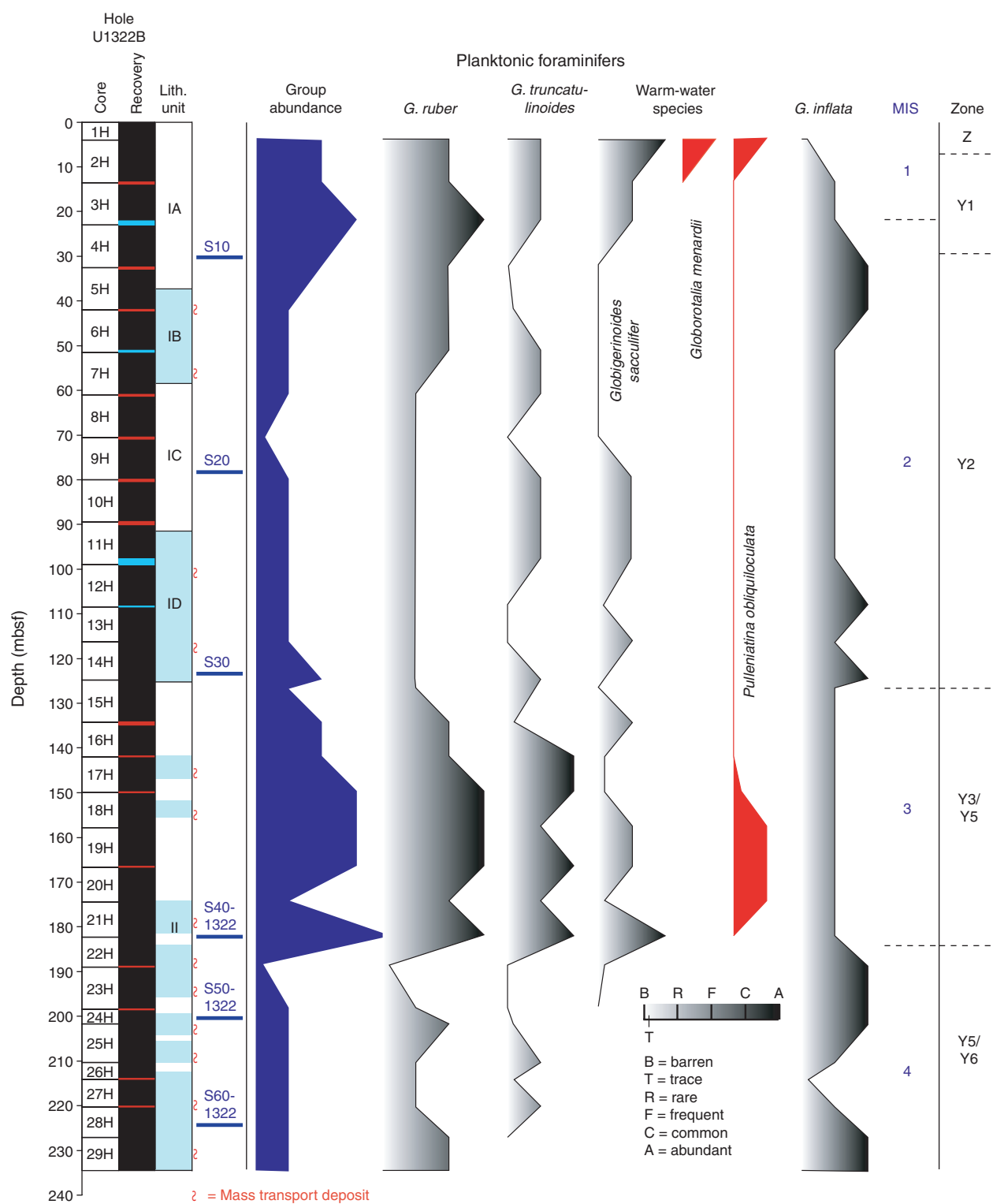
**Figure F19.** Distribution of nannofossils from Holes U1322C and U1322D. Nannofossil zonation is given.



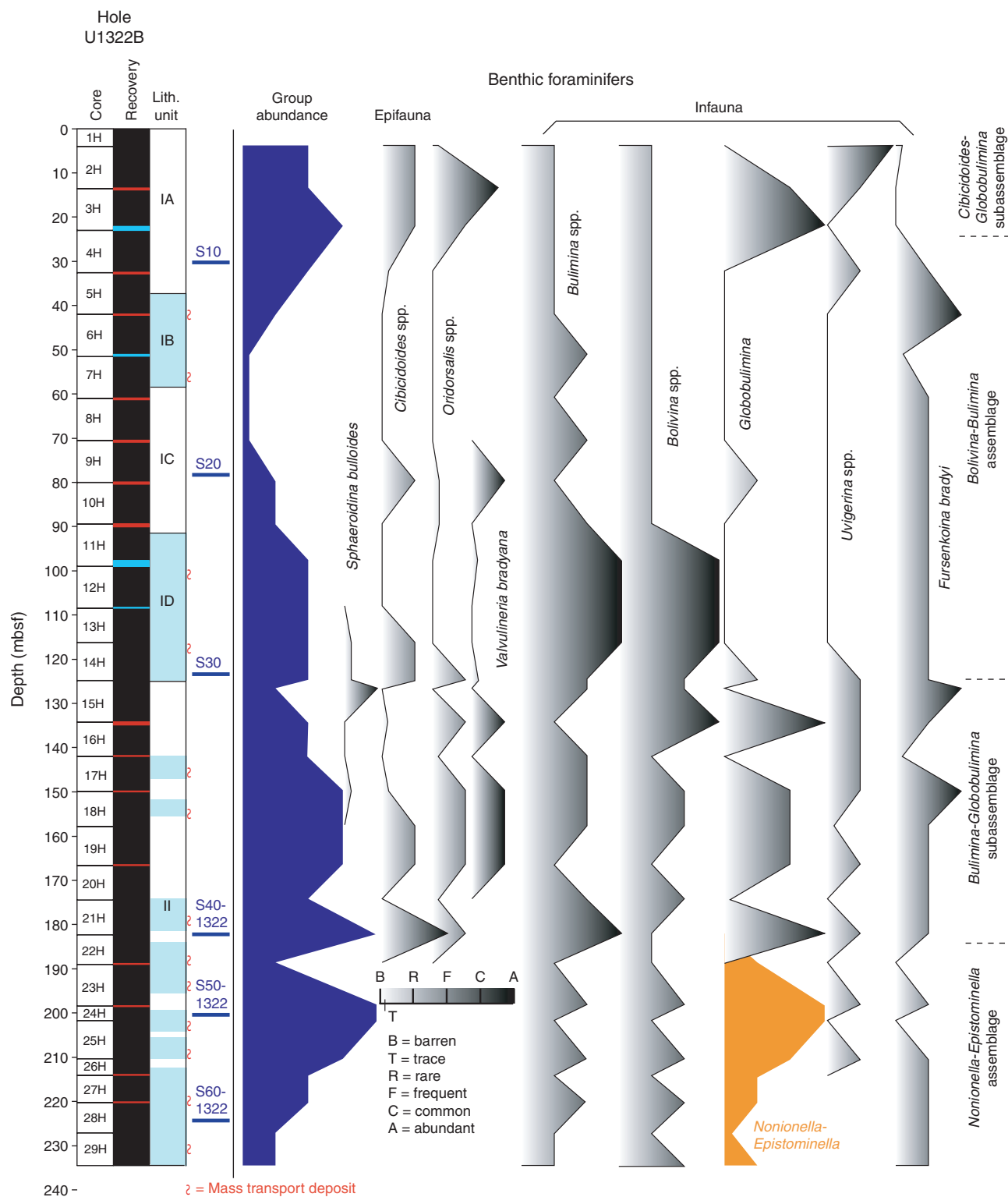
**Figure F20.** Correlation of sediment sections between Sites U1324 and U1322 on the basis of stratigraphically important nannofossil groups. Also shown are lithostratigraphic units and subunits and seismic reflectors.



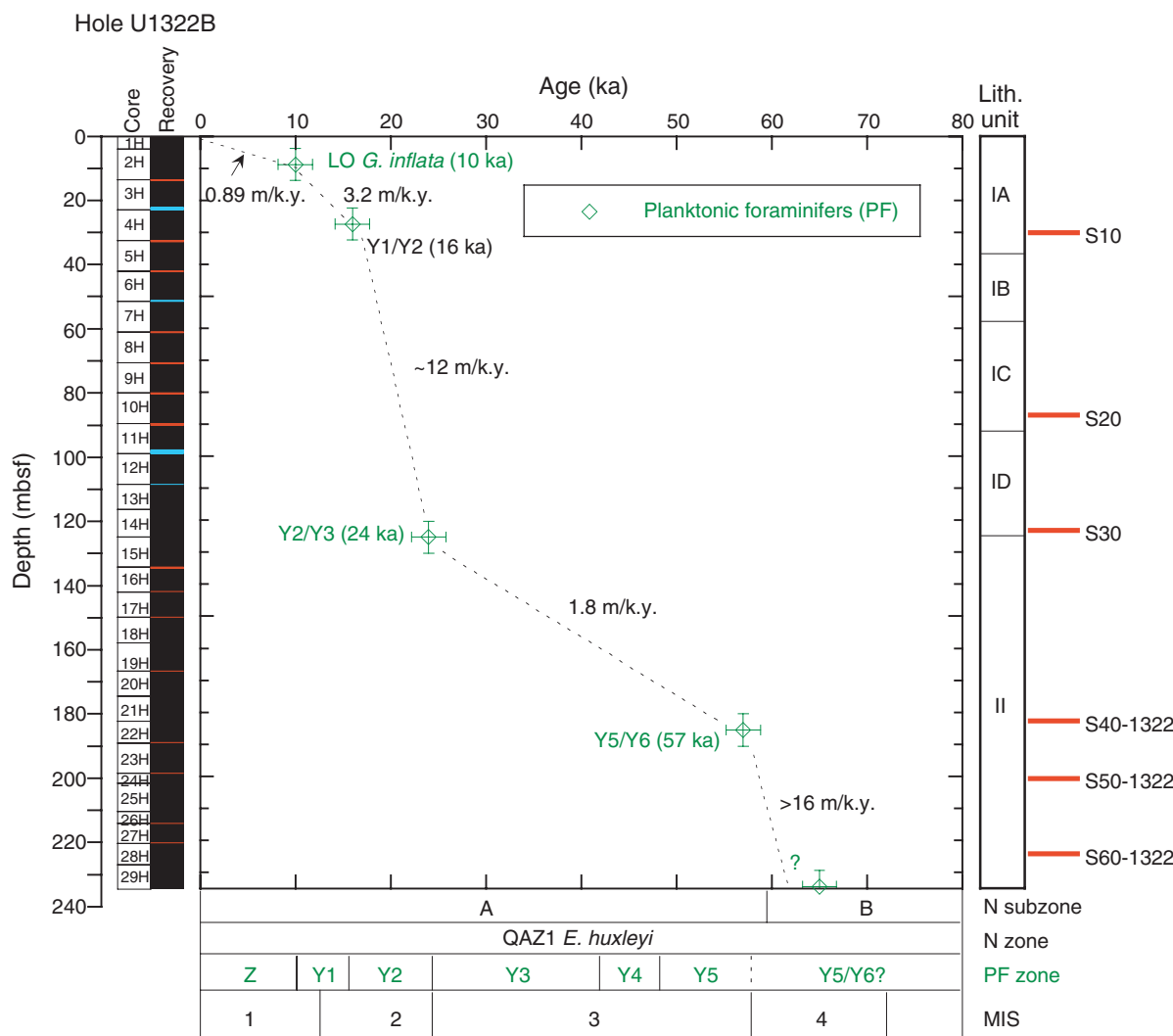
**Figure F21.** Planktonic foraminifer biostratigraphy and abundance of selected taxa from Hole U1322B. Also shown are lithostratigraphic units and subunits, seismic reflectors, and marine isotopic stages (MIS).



**Figure F22.** Distribution of selected epifaunal and infaunal benthic foraminifer species from Hole U1322B. Also shown are lithostratigraphic units and subunits, seismic reflectors, and benthic foraminifer assemblages and subassemblages.

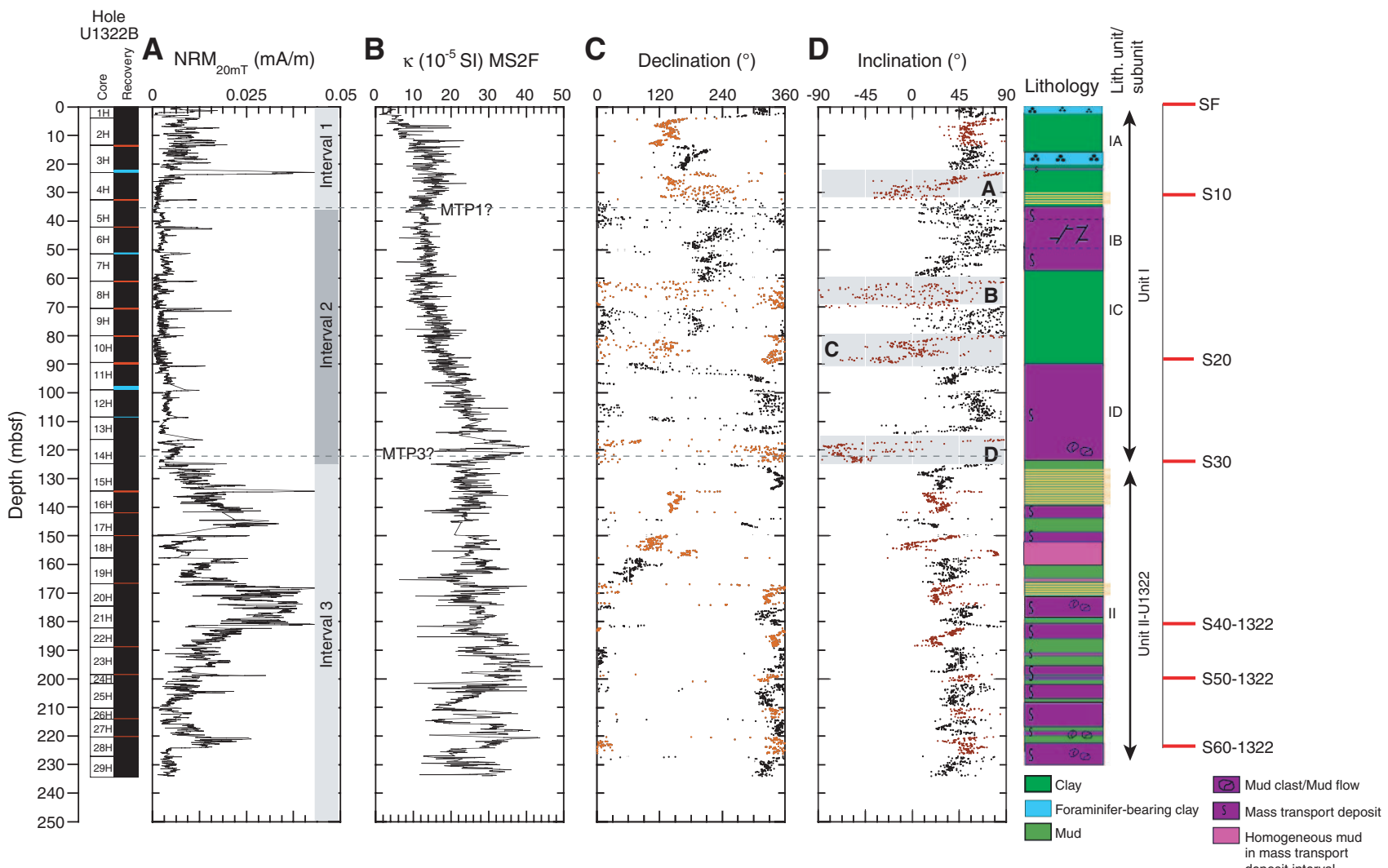


**Figure F23.** Planktonic foraminifer datums and calculated sedimentation rates for Site U1322 (see Table T10). Lithostratigraphic units and subunits and seismic reflectors are described in “[Background and objectives](#)” and “[Lithostratigraphy](#),” respectively. N = nannofossil datum. MIS = marine isotope stage.

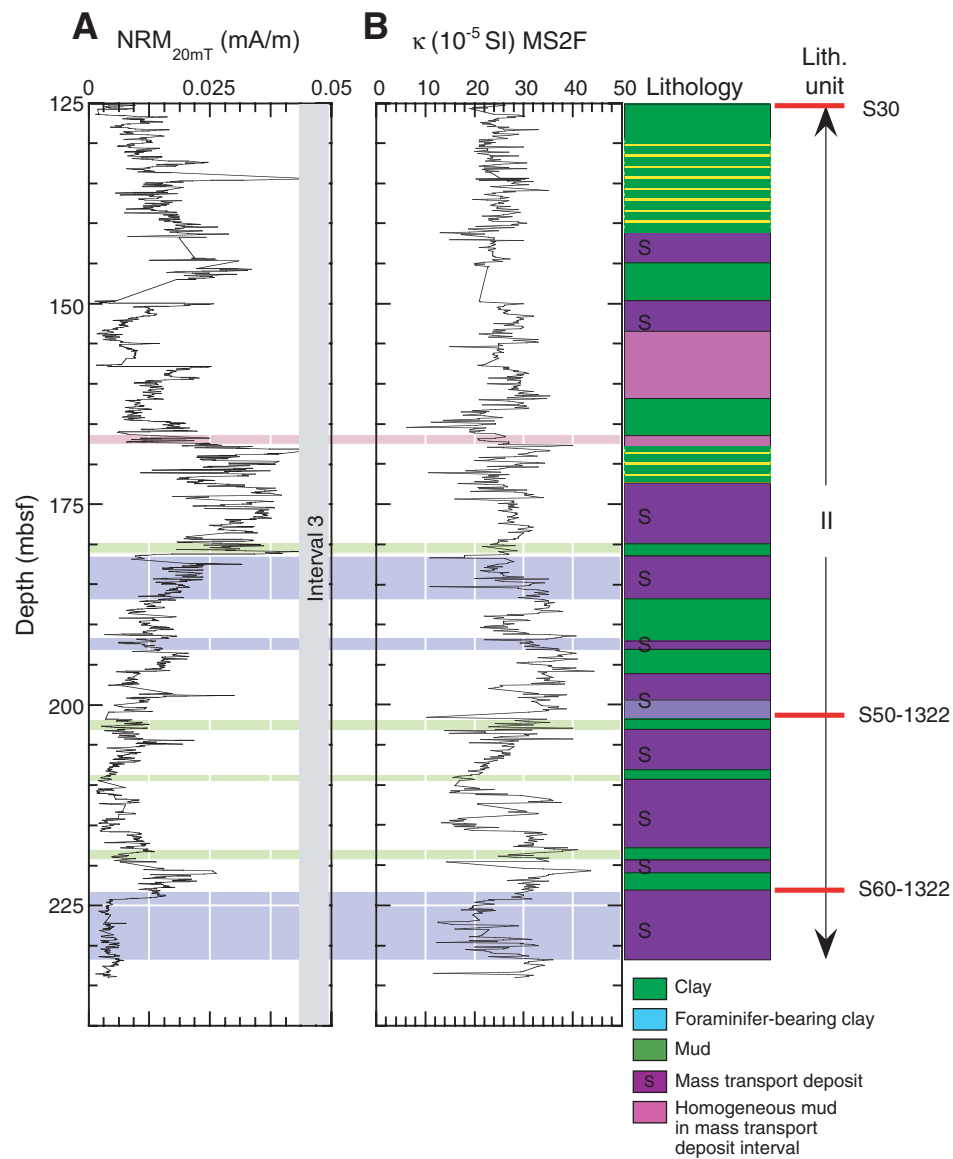




**Figure F24.** Uncorrected shipboard measurements on archive-half sections for (A) natural remanent magnetization after 20 mT AF demagnetization ( $\text{NRM}_{20\text{mT}}$ ), (B) MS2F sensor magnetic point susceptibility performed on archive halves at 10 cm resolution, including tentative magnetostratigraphic tie points MTP1 and MTP3, (C) declination (black = data from cores recovered using a nonmagnetic APC cutting shoe, red = data from cores recovered with the special Fugro cutting shoe), and (D) inclination (black = data from cores recovered using a nonmagnetic APC cutting shoe, red = data from cores recovered with the special Fugro cutting shoe). Depths have been corrected for voids in the core; paleomagnetic intervals, lithostratigraphic units, seismic reflectors (SF = seafloor), and paleomagnetic Subintervals 2A, 2B, 2C, and 2D are also shown.



**Figure F25.** Detailed close-up of the potential correlation of (A) natural remanent magnetization after 20 mT AF demagnetization ( $\text{NRM}_{20\text{mT}}$ ) and (B) magnetic susceptibility compared to the lithologic changes in lithostratigraphic Unit II (125–235 mbsf). Peaks in both records often coincide with a change in lithology, but no general correlation pattern is apparent.



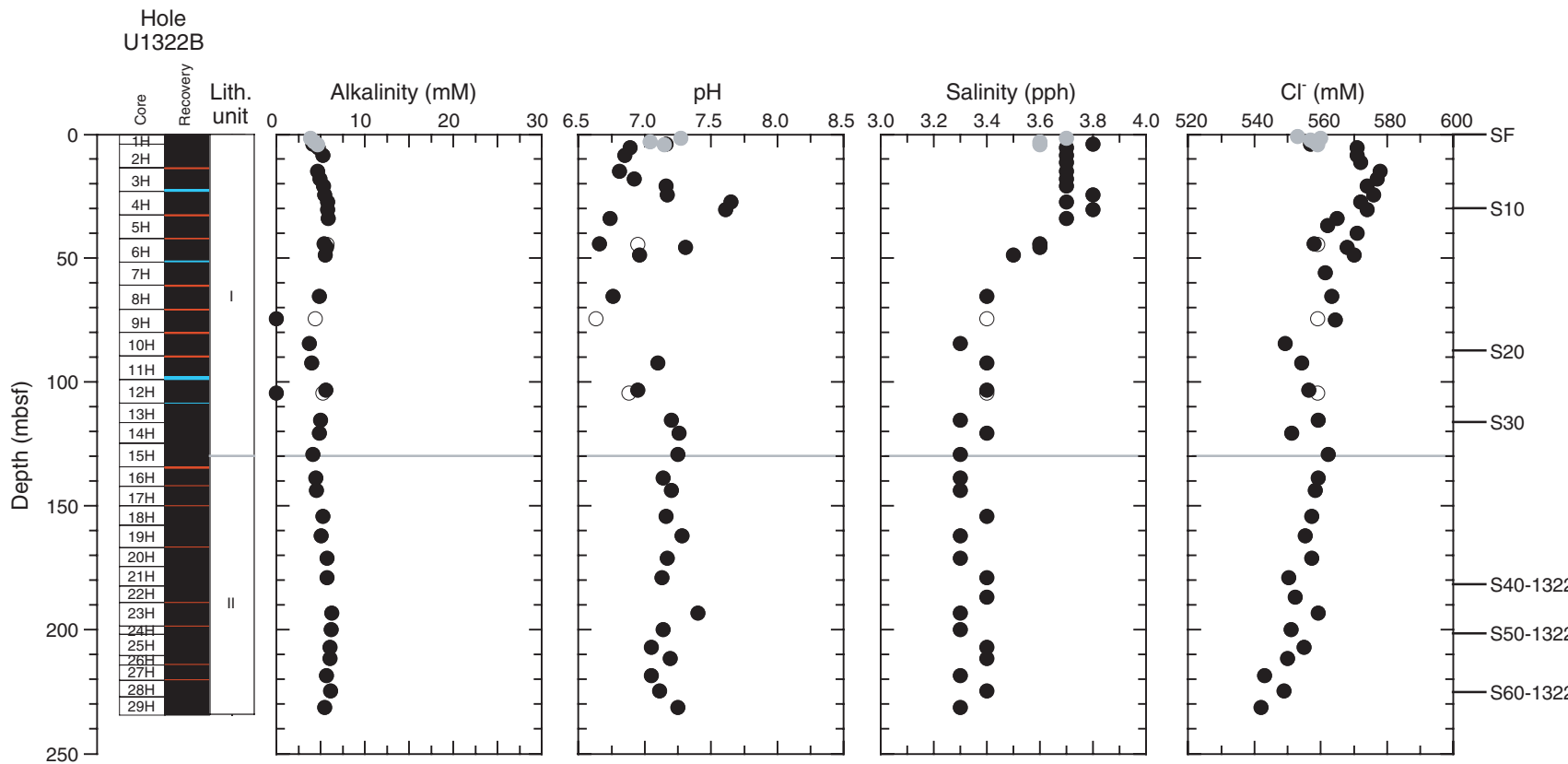




**Figure F27.** Interstitial water concentration profiles for  $\text{SO}_4^{2-}$ ,  $\text{NH}_4^+$ ,  $\text{PO}_4^{3-}$ , and  $\text{H}_4\text{SiO}_4$  (black = Hole U1322B, gray = Hole 1322C) along with lithostratigraphic units and seismic reflectors (SF = seafloor).

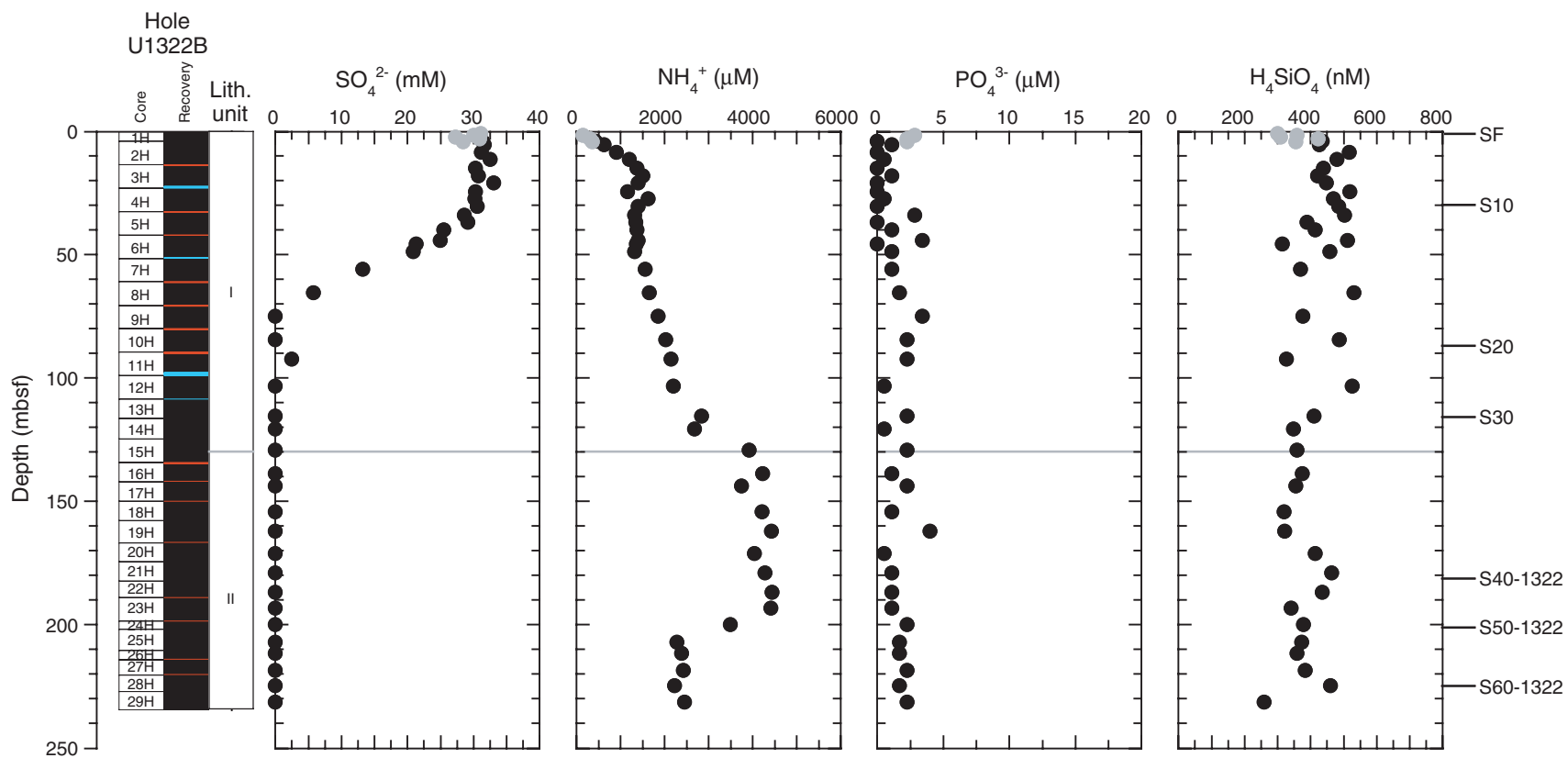


**Figure F28.** Interstitial water concentration profiles for major cations  $\text{Na}^+$ ,  $\text{K}^+$ ,  $\text{Ca}^{2+}$ ,  $\text{Mg}^{2+}$  (black = Hole U1322B, gray = Hole 1322C) along with lithostratigraphic units and seismic reflectors (SF = seafloor).

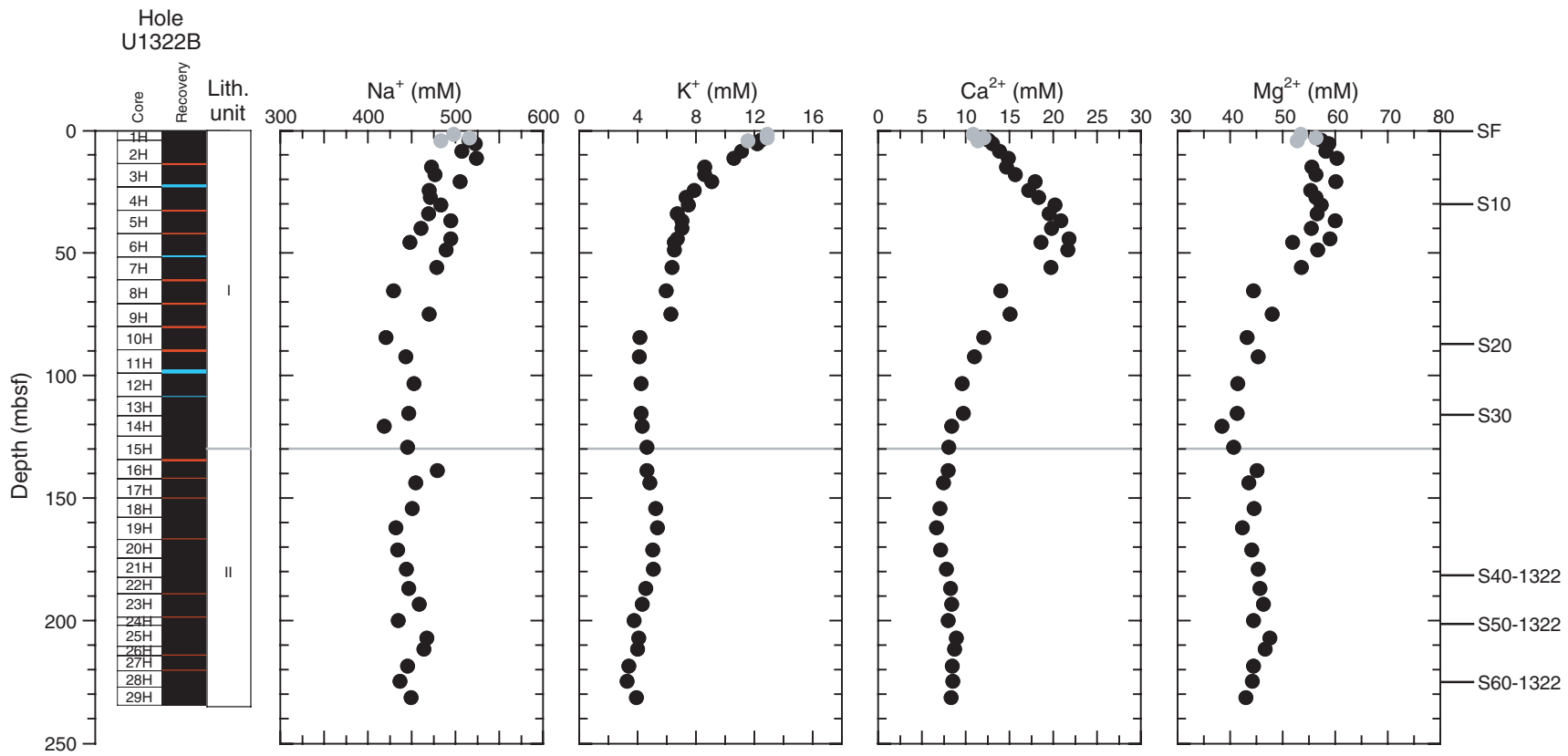




**Figure F29.** Interstitial water concentration profiles for trace metals  $B^{3+}$ ,  $Li^+$ , and  $Sr^{2+}$  (black = Hole U1322B, gray = Hole 1322C) along with lithostratigraphic units and seismic reflectors (SF = seafloor). (Continued on next page.)

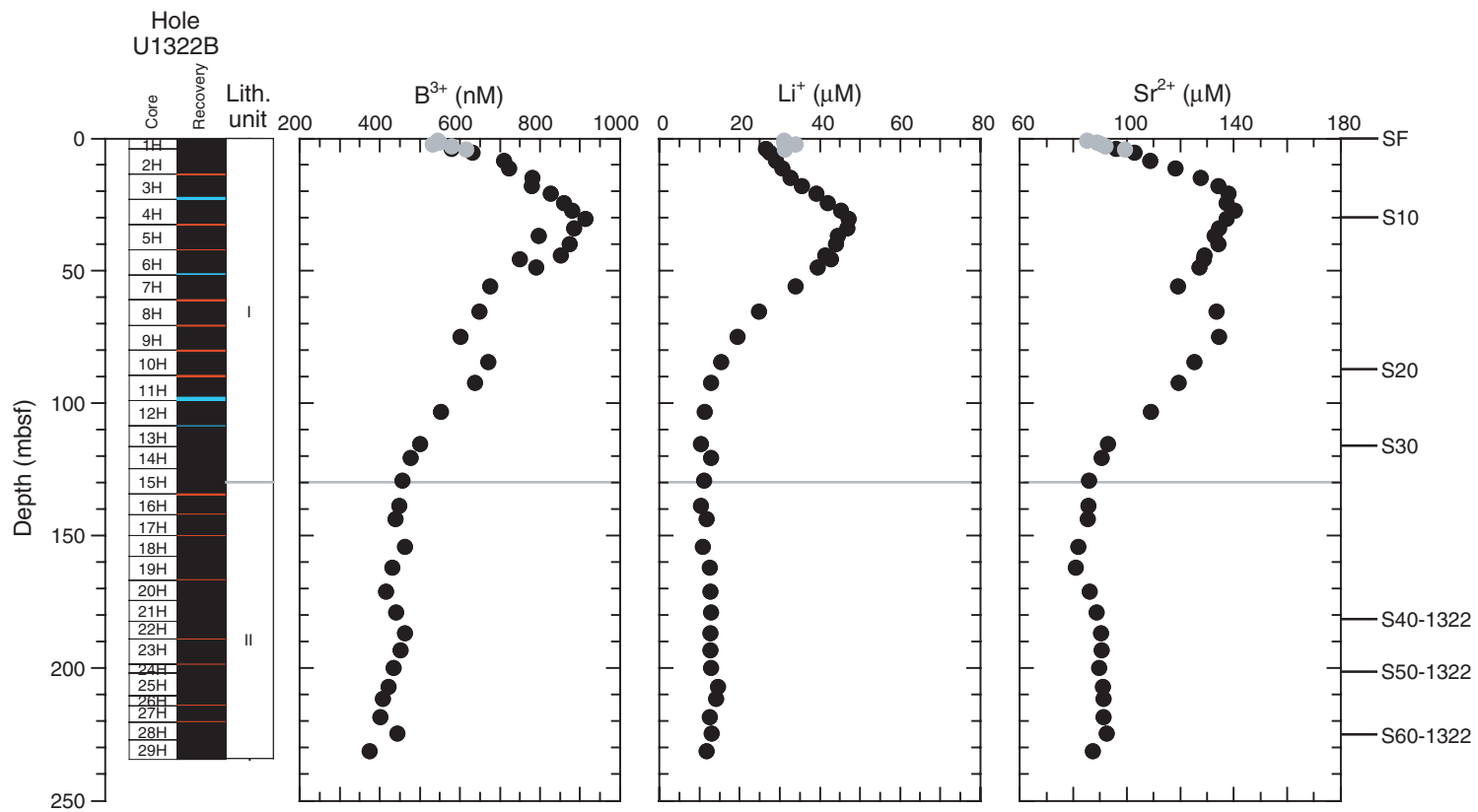


**Figure F29 (continued).**  $\text{Ba}^{2+}$ ,  $\text{Fe}^{2+}$ , and  $\text{Mn}^{2+}$ .

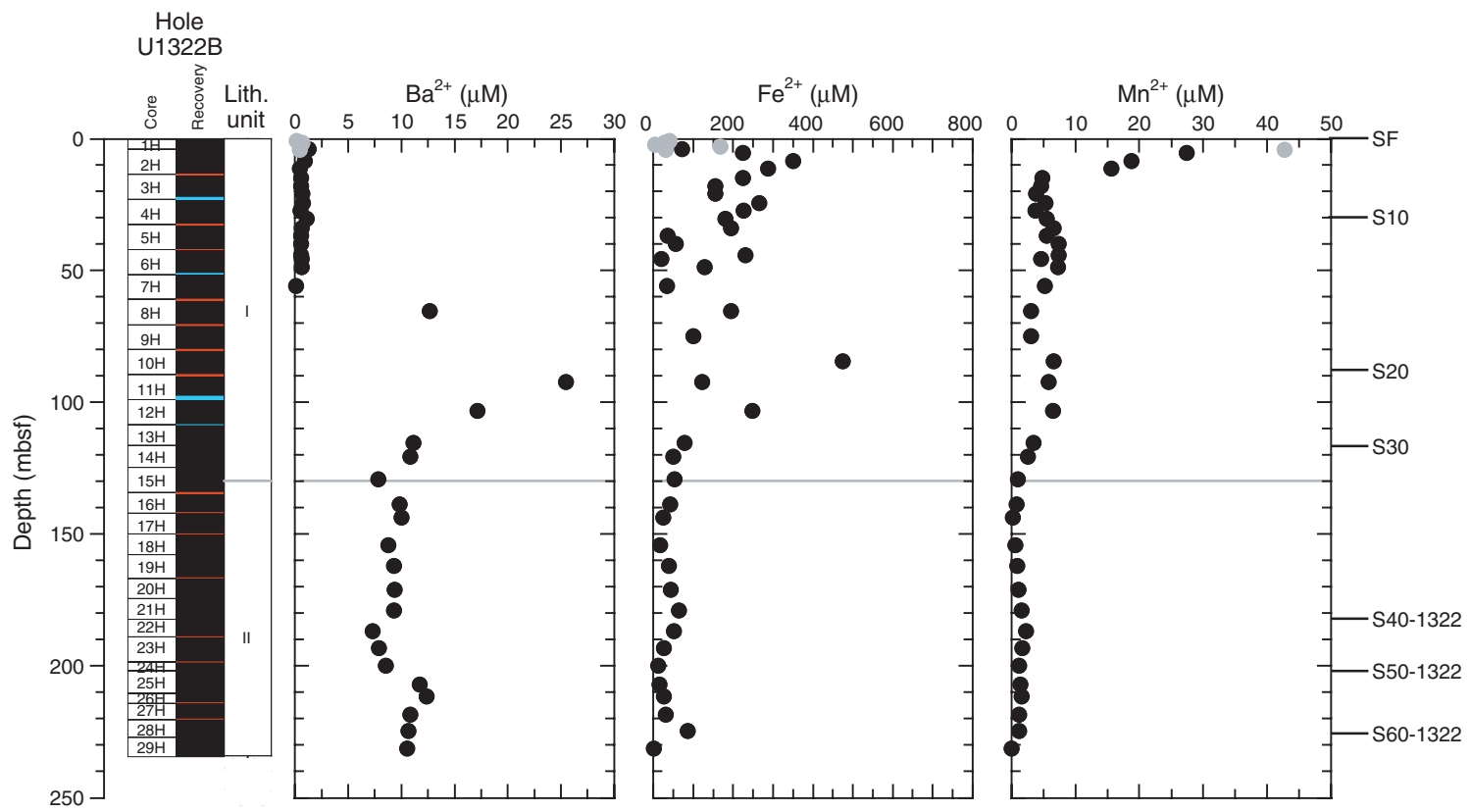


**Figure F30.** Downhole variations in total inorganic carbon (TIC), total organic carbon (TOC), calcium carbonate, total nitrogen, C/N, and total hydrogen in sediments at Site U1322 (black = Hole U1322B, gray = Hole 1322C, open = Hole U1322D), along with lithostratigraphic units and seismic reflectors (SF = seafloor).

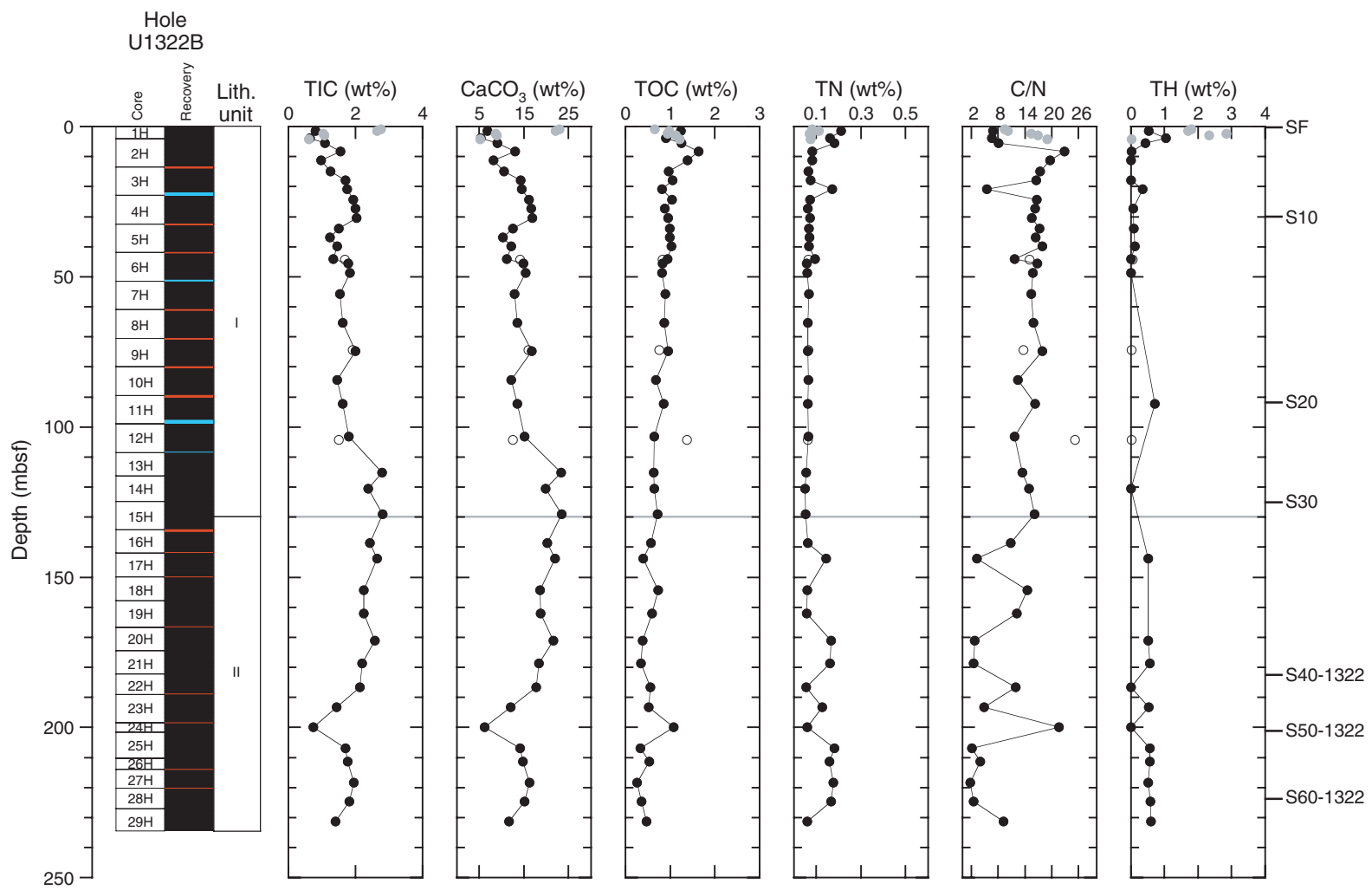


**Figure F31.** Headspace gas concentrations of methane and ethane in Hole U1322B along with lithostratigraphic units and seismic reflectors (SF = seafloor).

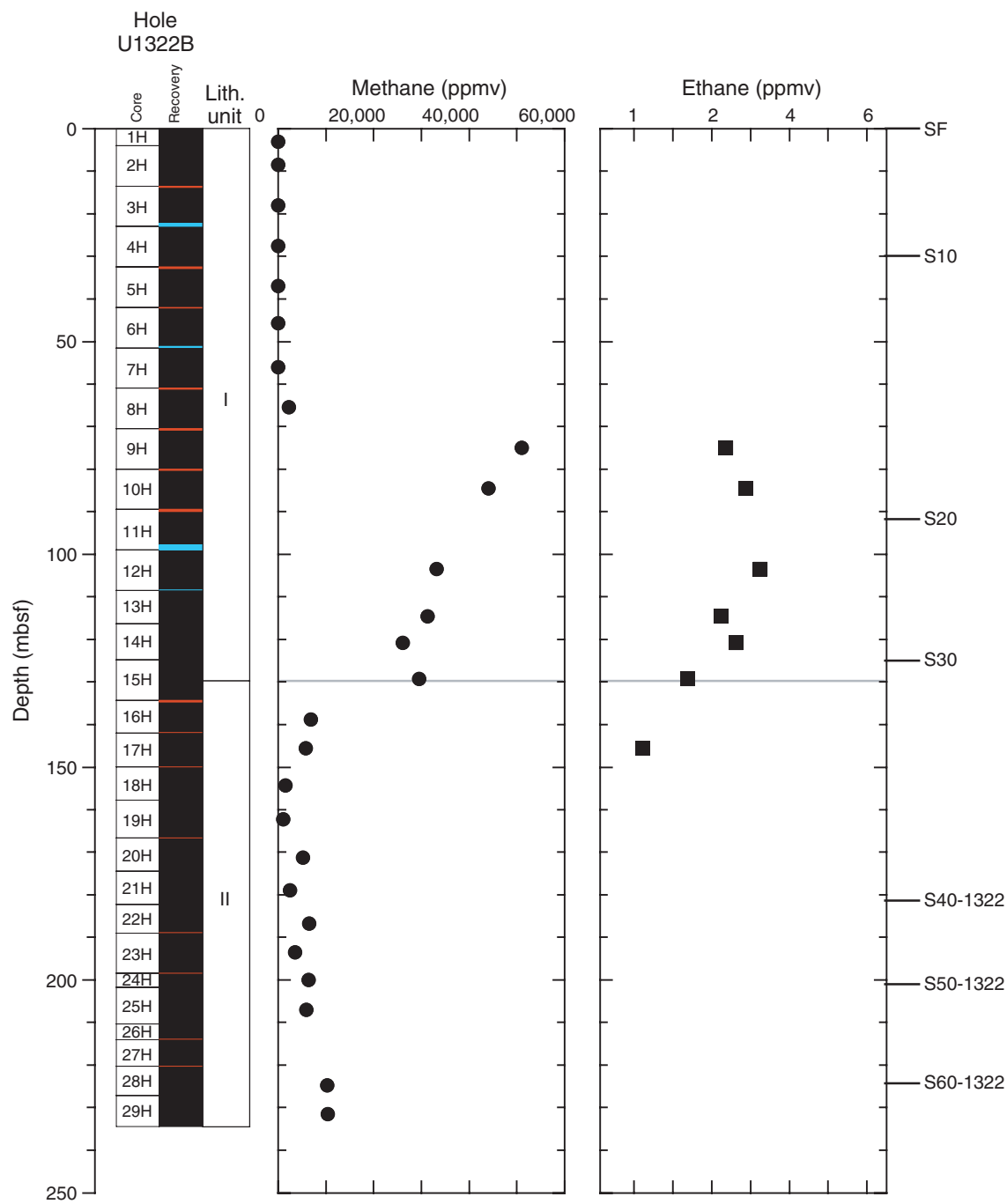


**Figure F32.** Profiles of methane and sulfate concentrations in Hole U1322B along with lithostratigraphic units and seismic reflectors (SF = seafloor).

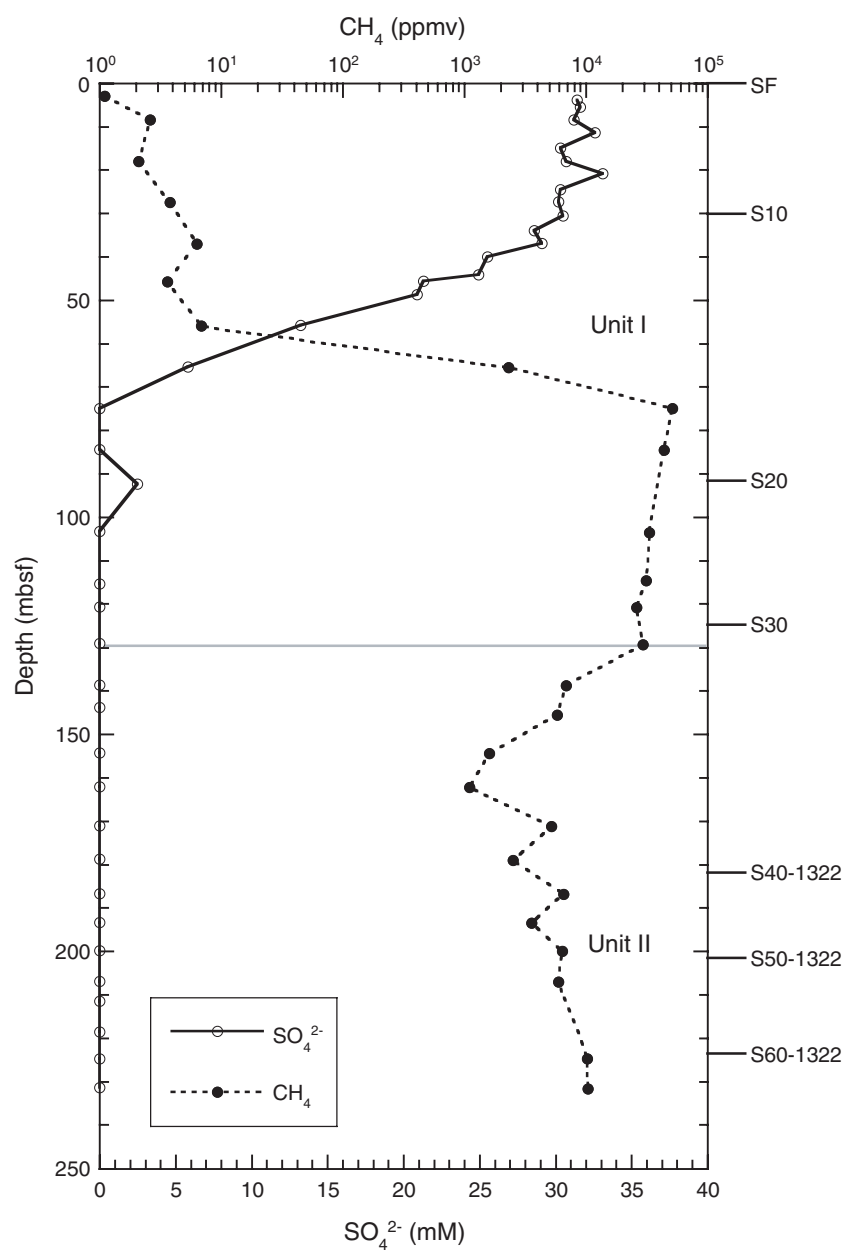


**Figure F33.** Cell density profile in Hole U1322B. Solid symbols = cell density, open symbols = not detected or below significant levels. SF = seafloor.

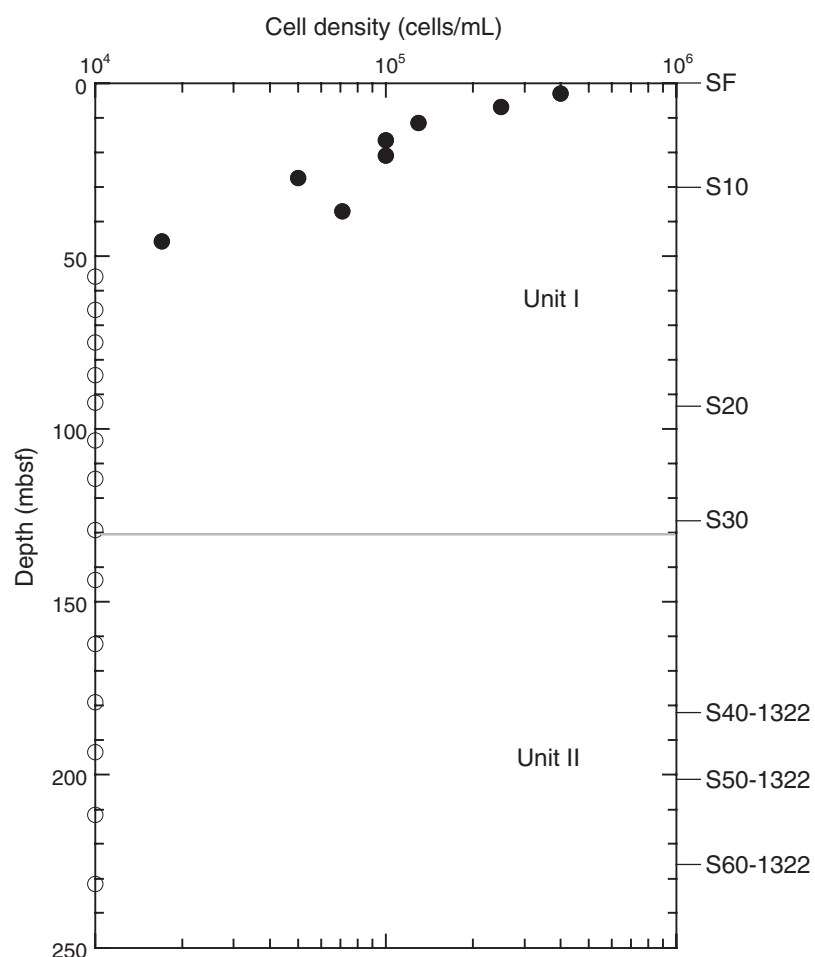


**Figure F34.** A. Bulk density determined from moisture and density (MAD), multisensor track (MST), and measurement while drilling (MWD: image-derived density [IDRO]). B. Grain density from MAD measurements. C. Porosity from MAD measurements and also calculated from IDRO assuming a constant grain density of 2.7 g/cm<sup>3</sup> and a pore water density of 1.024 g/cm<sup>3</sup>. Yellow = mass transport deposits (see “[Lithostratigraphy](#)”); lithostratigraphic units and seismic reflectors (SF = seafloor) are also shown.

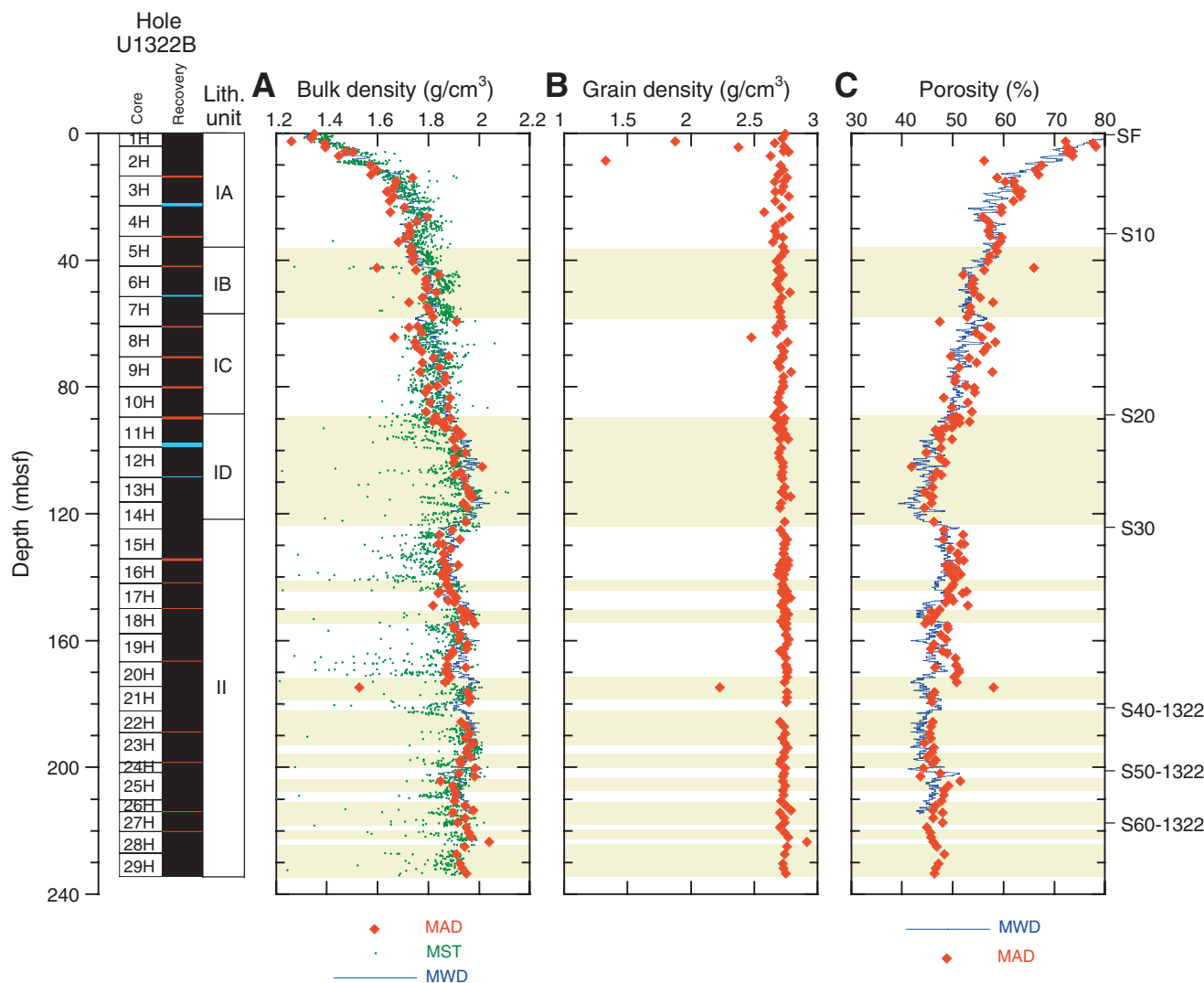




**Figure F35.** (A) Noncontact resistivity and (B) deep resistivity from logging while drilling/measurement while drilling (LWD/MWD; see Fig. F43). Yellow = mass transport deposits (see “[Lithostratigraphy](#)”); lithostratigraphic units and seismic reflectors (SF = seafloor) are also shown.

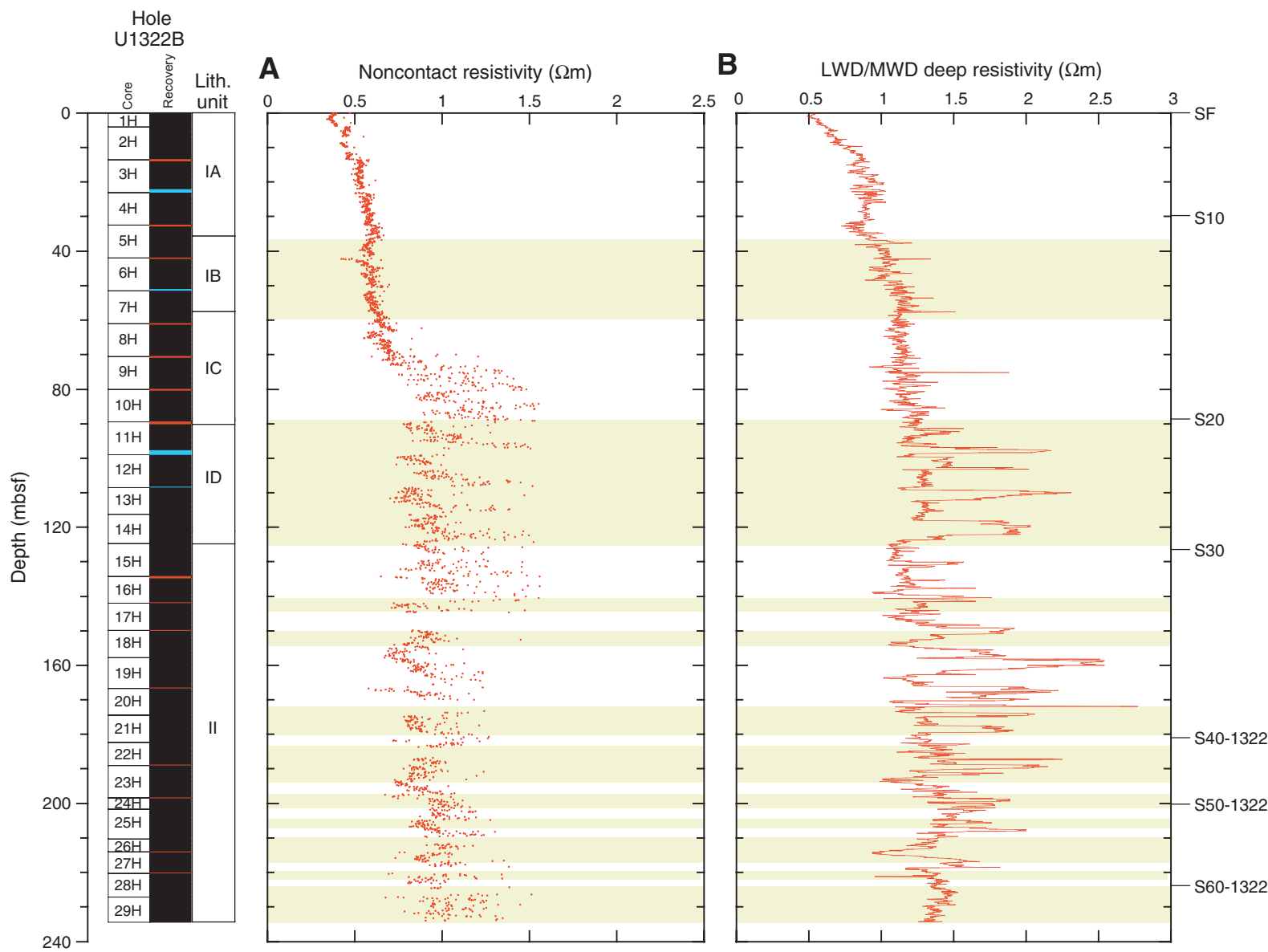


**Figure F36.** Magnetic susceptibility. Yellow = mass transport deposits (see “[Lithostratigraphy](#)”); lithostratigraphic units and seismic reflectors are also shown.

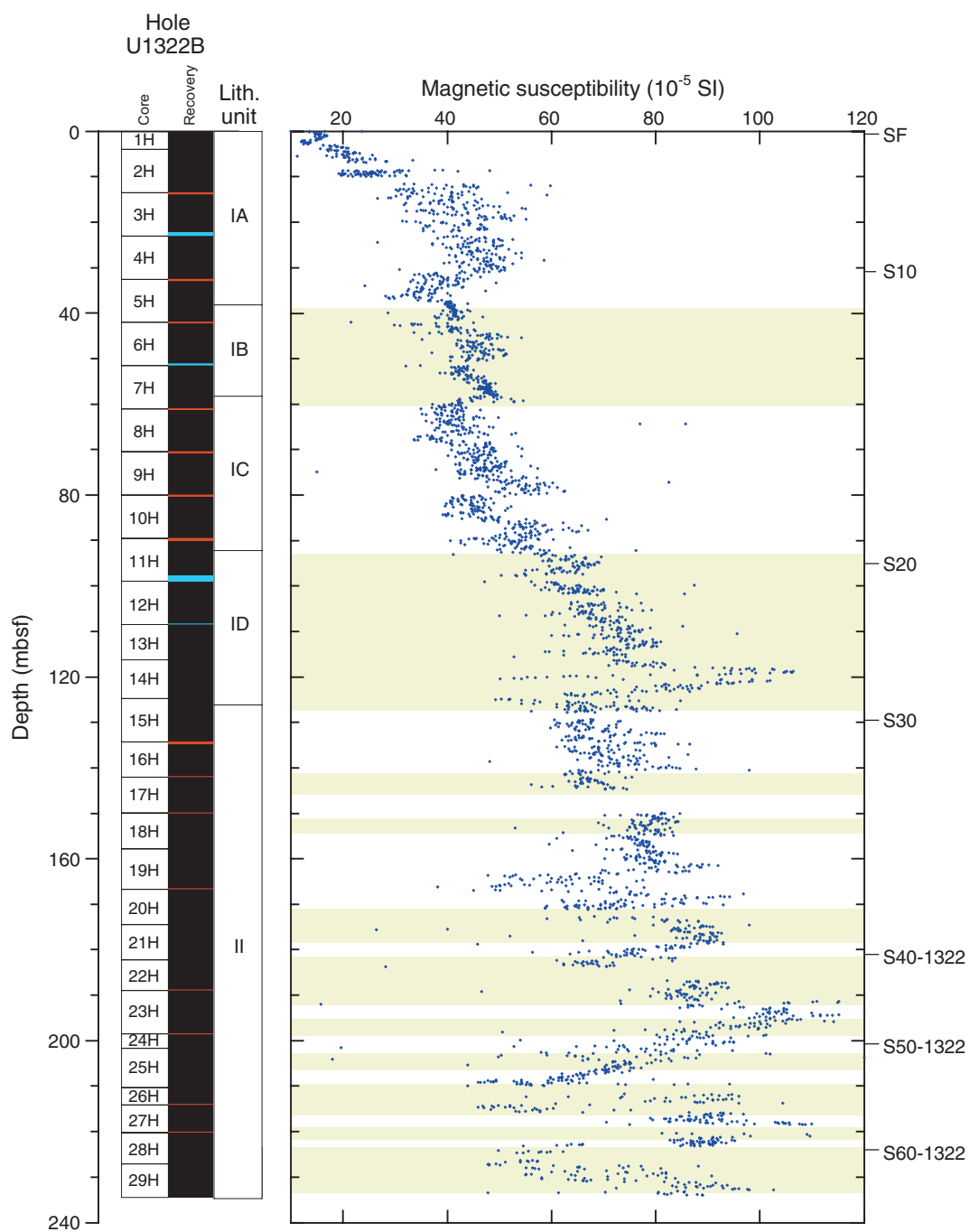


**Figure F37.** Thermal conductivity. Yellow = mass transport deposits (see “[Lithostratigraphy](#)”); lithostratigraphic units and seismic reflectors (SF = seafloor) are also shown.

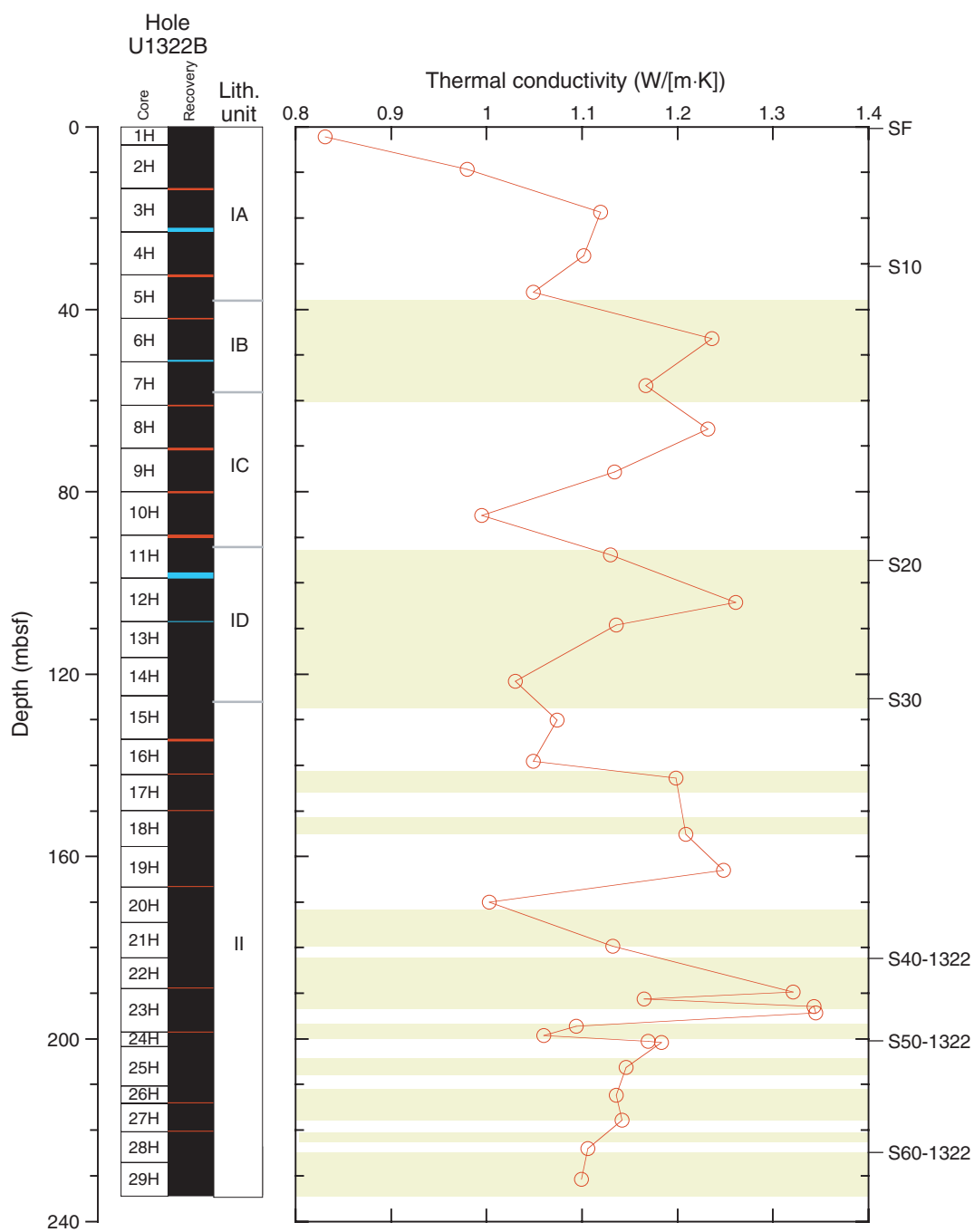


**Figure F38.** P-wave velocity (PWS = P-wave sensor; PWL = P-wave logger on the MST). Yellow = mass transport deposits (see “[Lithostratigraphy](#)”); lithostratigraphic units and seismic reflectors (SF = seafloor) are also shown.

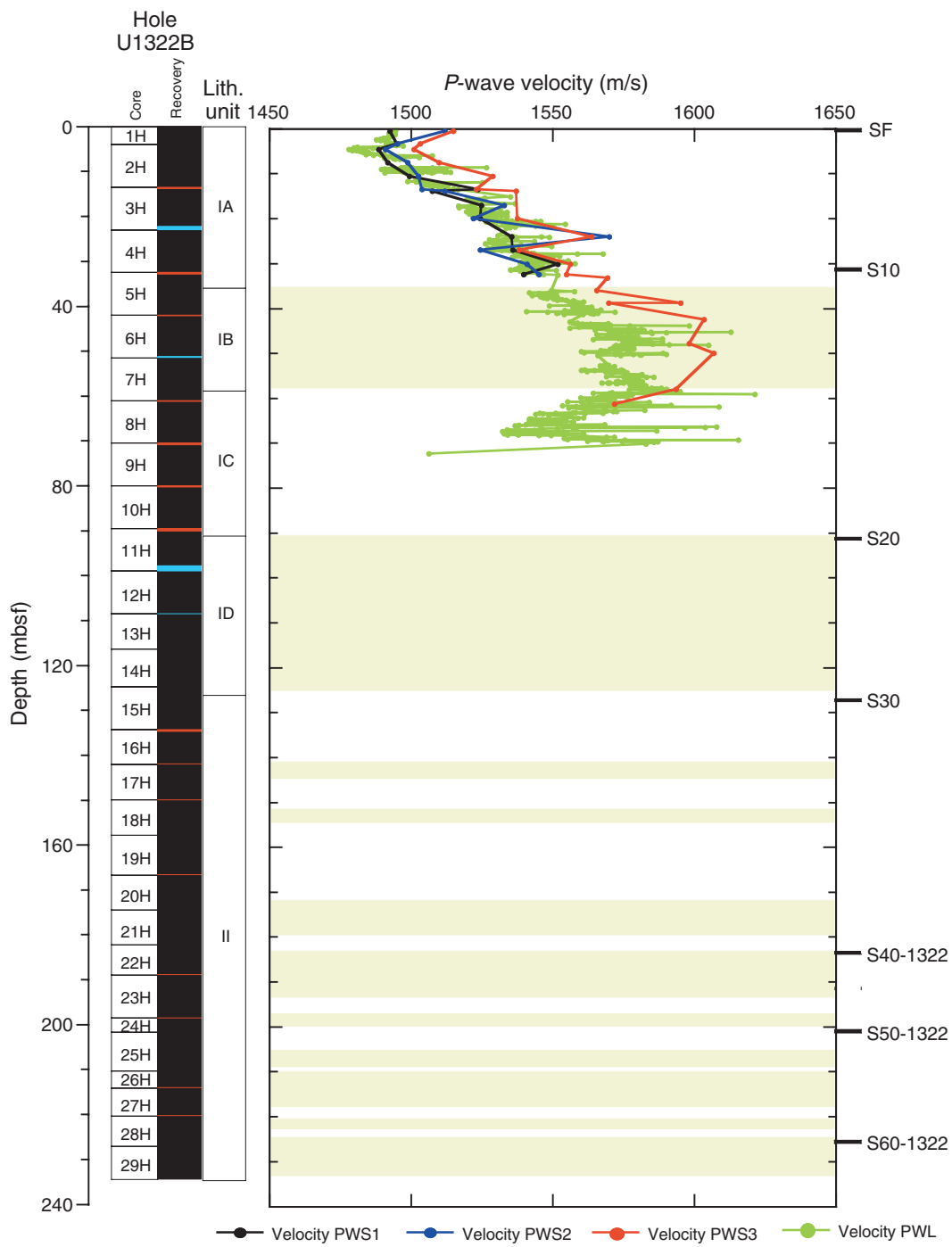


**Figure F39.** (A) Peak and residual undrained shear strength from vane shear tests, (B) comparison of peak undrained shear strengths measured by vane and pocket penetrometer, and (C) sensitivity (ratio between peak and residual undrained shear strength using AVS). Yellow = mass transport deposits (see “[Lithostratigraphy](#)”); lithostratigraphic units and seismic reflectors (SF = seafloor) are also shown.

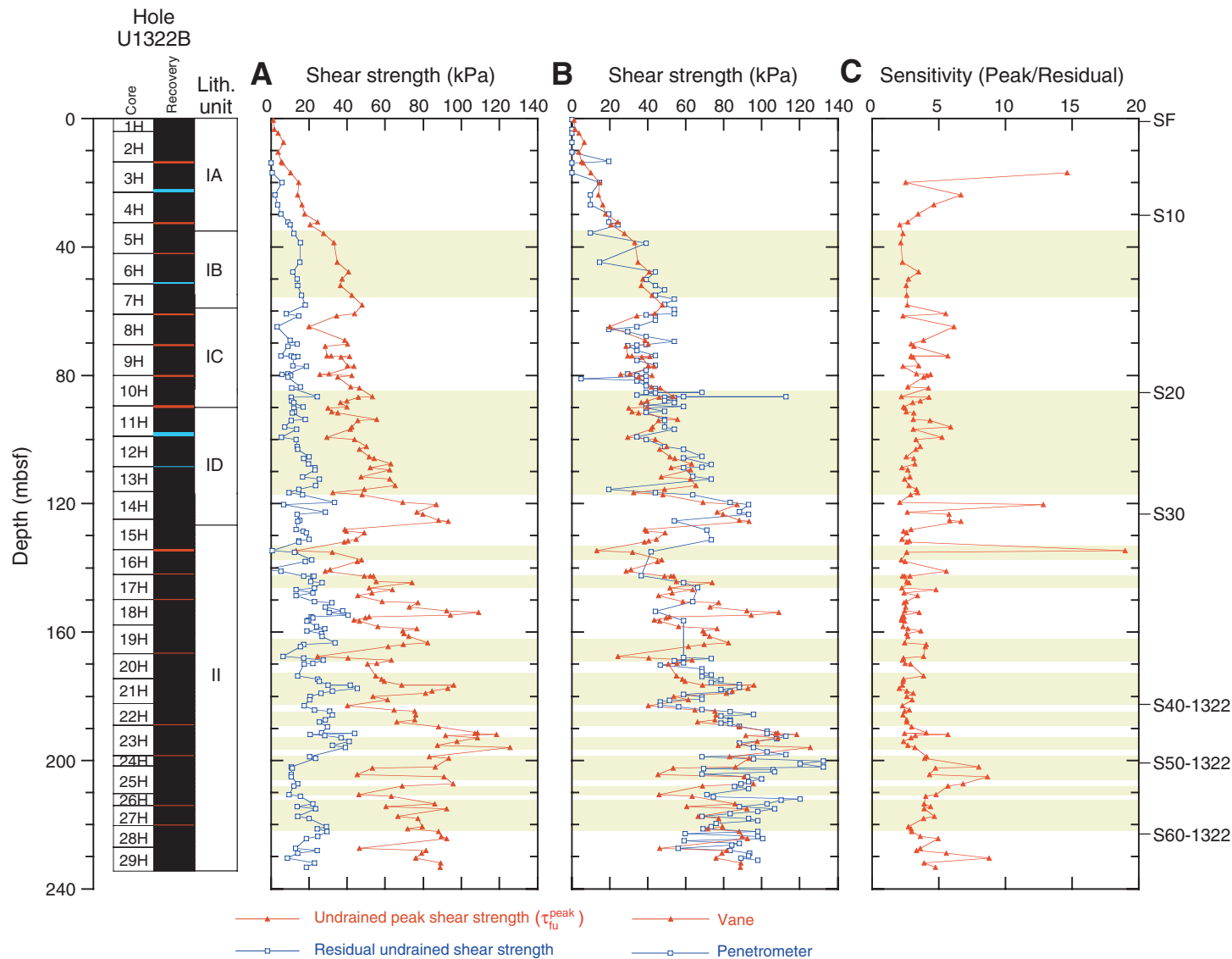


**Figure F40.** A. Undrained peak shear strength vs. the ratio between peak shear strength ( $\tau_{fu}^{\text{peak}}$ ) and vertical hydrostatic effective stress ( $\sigma_{vh}'$ ). B. Lithostatic stress ( $\sigma_v$ ) and vertical hydrostatic effective stress ( $\sigma_{vh}'$ ; assumes hydrostatic conditions) estimated from logging-while-drilling data. Yellow = mass transport deposits (see “[Lithostratigraphy](#)”); lithostratigraphic units and seismic reflectors (SF = seafloor) are also shown.

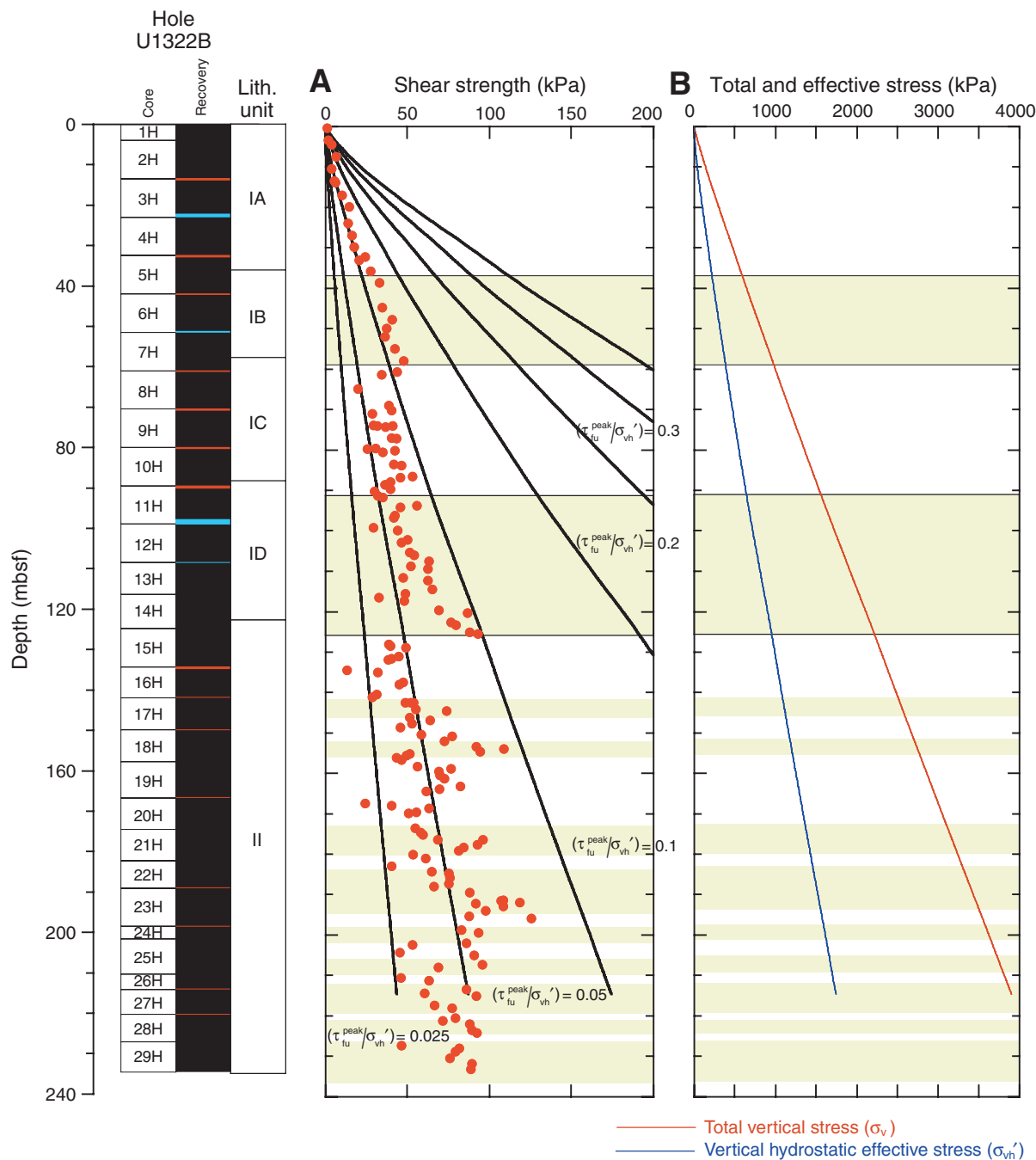


**Figure F41.** Data quality displayed for measurement-while-drilling and logging-while-drilling (MWD/LWD) measurements from Hole U1322A. The rate of penetration (ROP), density-derived caliper, and density correction based on hole diameter are shown.

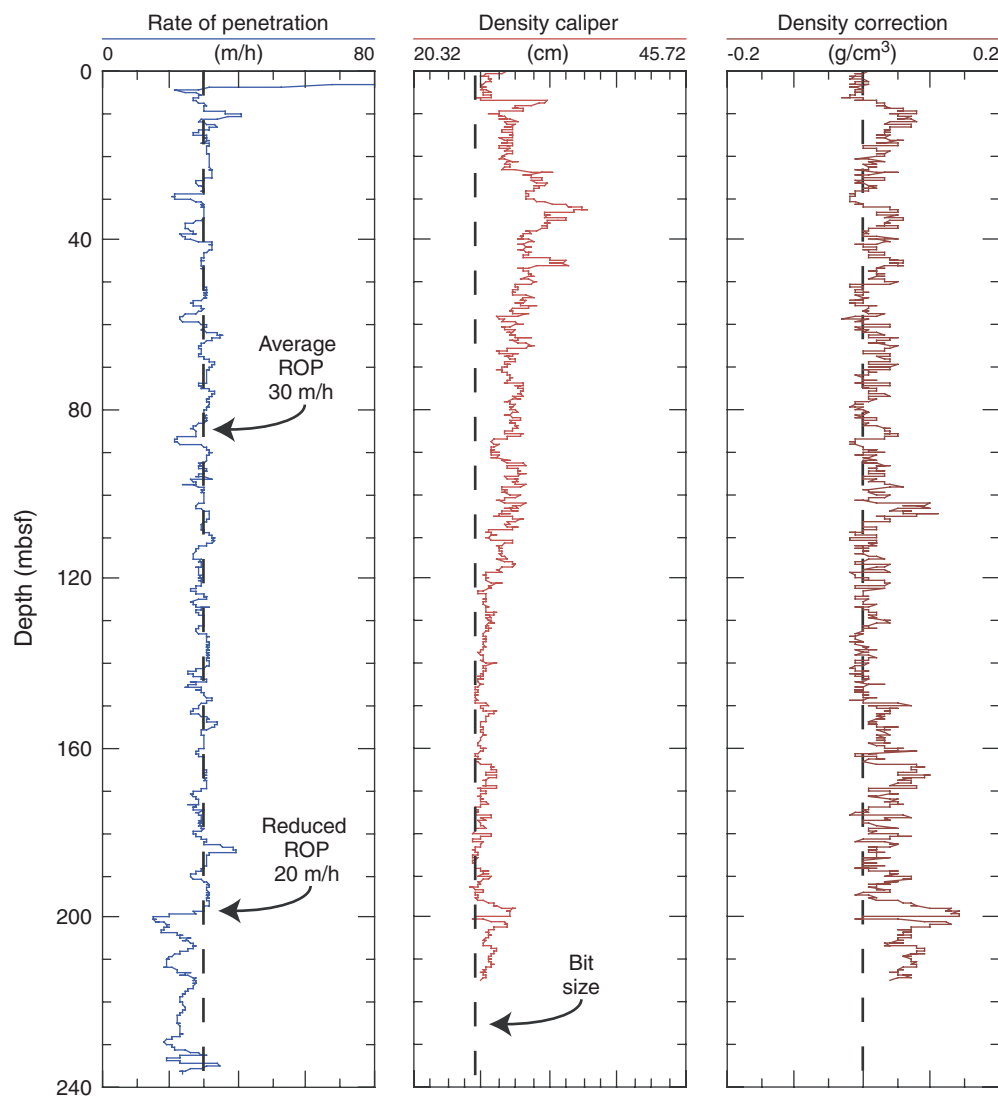


**Figure F42.** Annular pressure-while-drilling (APWD) monitoring of Hole U1322A. The almost linear increase of APWD is interpreted to record stable borehole conditions throughout the borehole and no shallow-water flow problems. Subtle variations in annular overpressure in excess of hydrostatic (APWD\*), equivalent circulating density referenced to seafloor (ECD<sub>rsf</sub>), and caliper measurements are interpreted to reflect loose material filling the borehole annulus. Gamma ray (GR) and caliper measurements are shown for correlation. SF = seafloor.

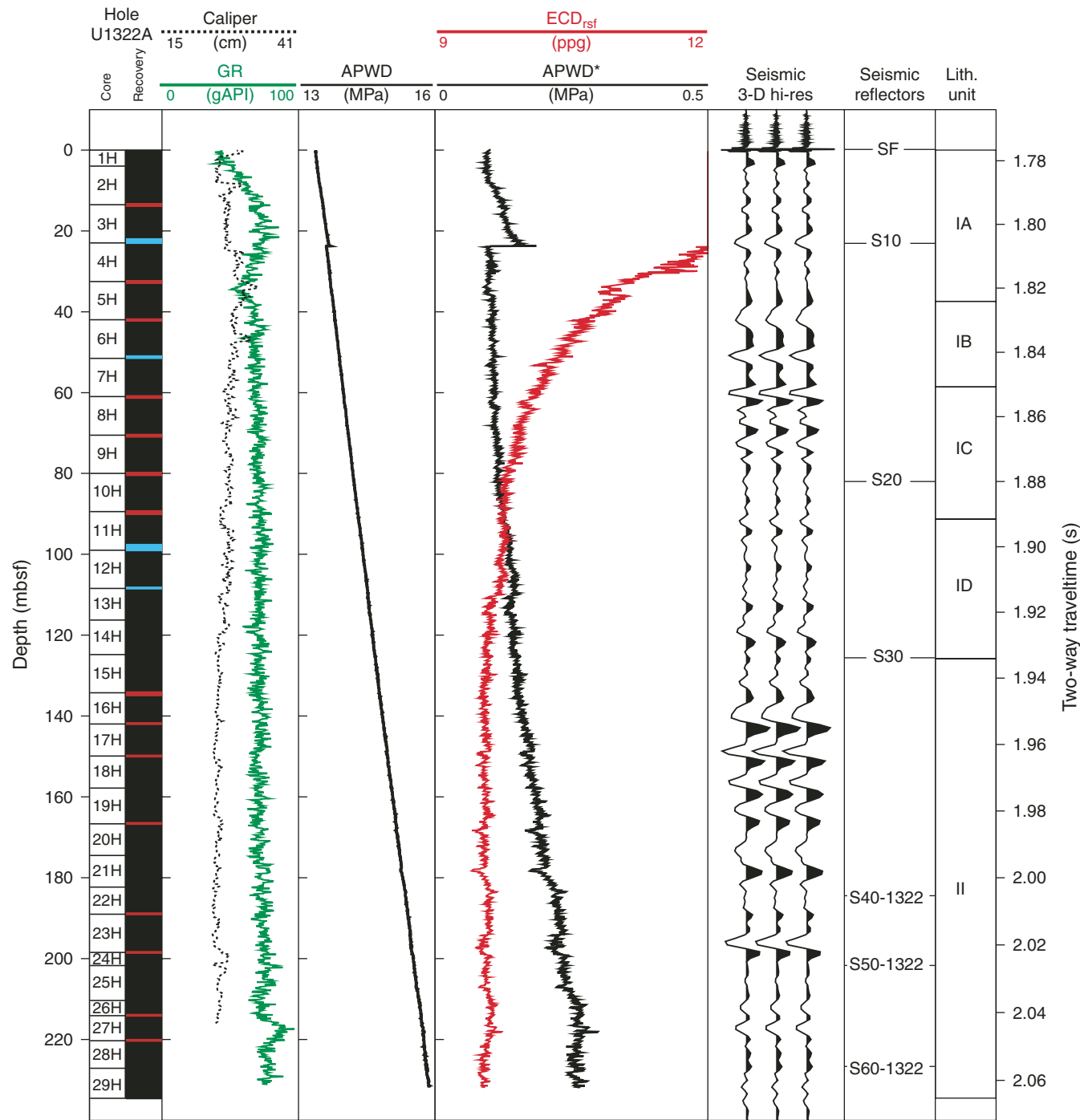


**Figure F43.** LWD logs recorded in Hole U1322A. Density caliper, photoelectric factor (PEF), and neutron porosity were recorded with the Vision Density Neutron (VDN) tool, whereas gamma ray and resistivity were obtained with the GeoVision Resistivity (GVR) tool. Superimposed on the PEF log is a five-point sliding window curve.

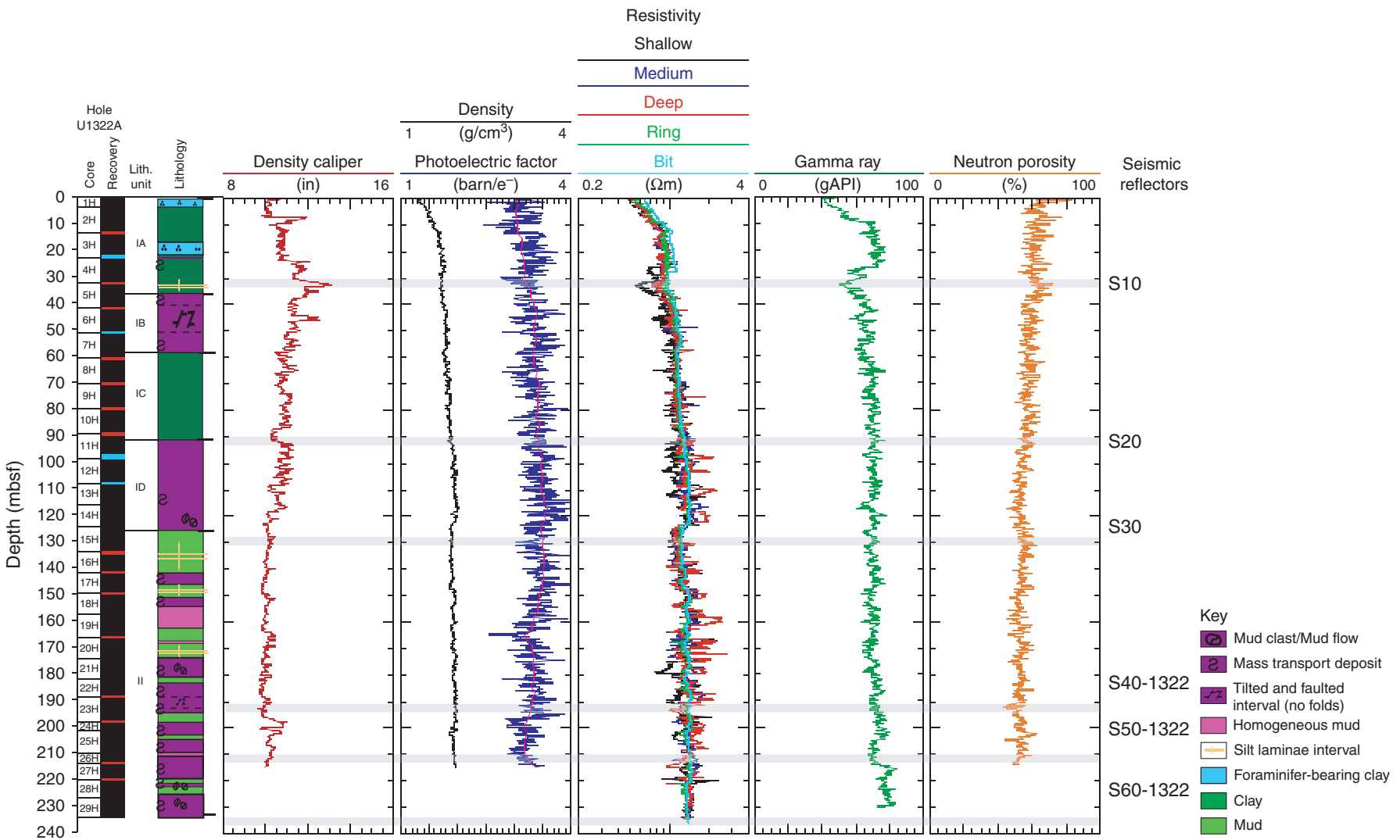


**Figure F44.** Core-log-seismic correlation for Site U1322. The synthetic seismogram was constructed by convolving a 200 Hz minimum-phase Ricker wavelet with the reflection coefficient series based on LWD bulk density and a constant velocity (1600 m/s). A seismic high-resolution trace (Hi-Res) is extracted from 3-D high-resolution multichannel seismic data at the location of Site U1322. Caliper, gamma ray (GR), and resistivity logs are also plotted. Time-depth calibration is based on Equation E1.

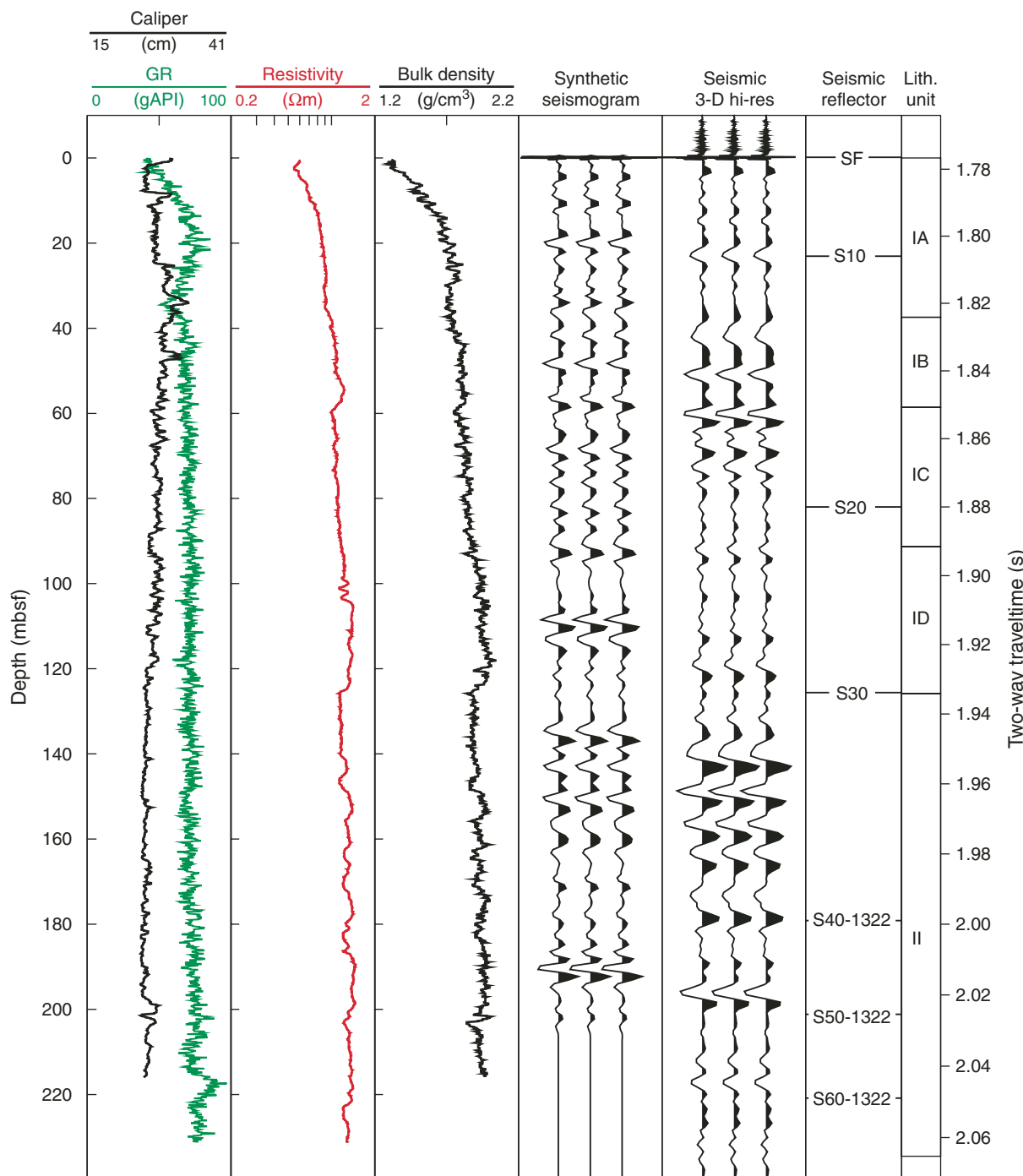


**Figure F45.** Static and dynamic resistivity-at-the-bit GeoVision Resistivity (GVR) image with gamma ray (green) and RING resistivity (red) logs for Hole U1322A. The displayed section represents the highly disturbed lithostratigraphic Subunit IB, characterized by steeply dipping beds, faults, and folded sediments. Also indicated are breakouts reflecting the east-west-oriented minimum horizontal stress. The third column highlights the dip angle of the observed planes. Lithologic column is also plotted.

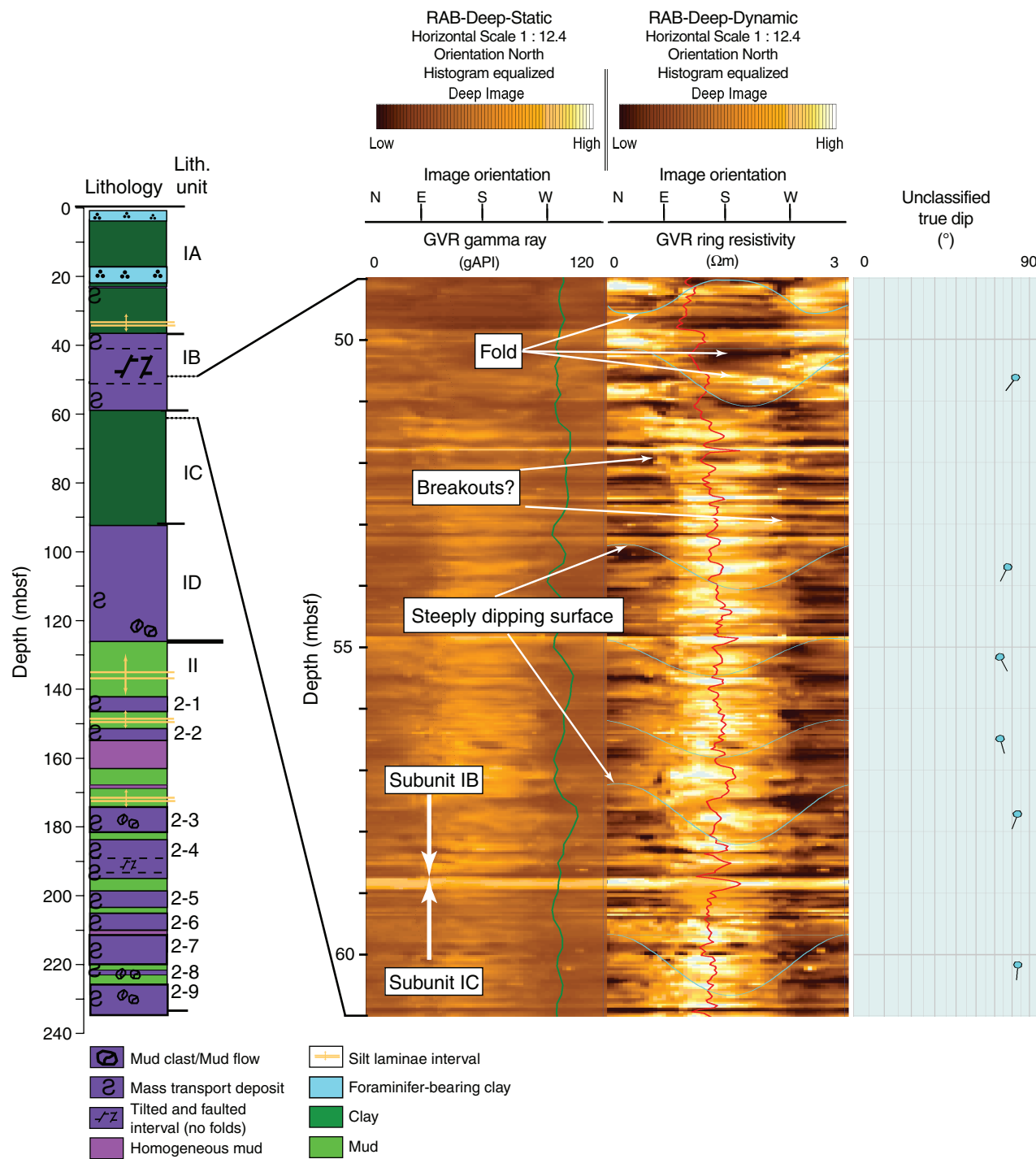


**Figure F46.** Static and dynamic resistivity-at-the-bit GeoVision Resistivity (GVR) image with gamma ray (green) and ring resistivity (red) logs for Hole U1322A. Breakouts reflect the east-west-oriented minimum horizontal stress. The third column highlights the dip angle of the observed planes. Lithologic column is also plotted.

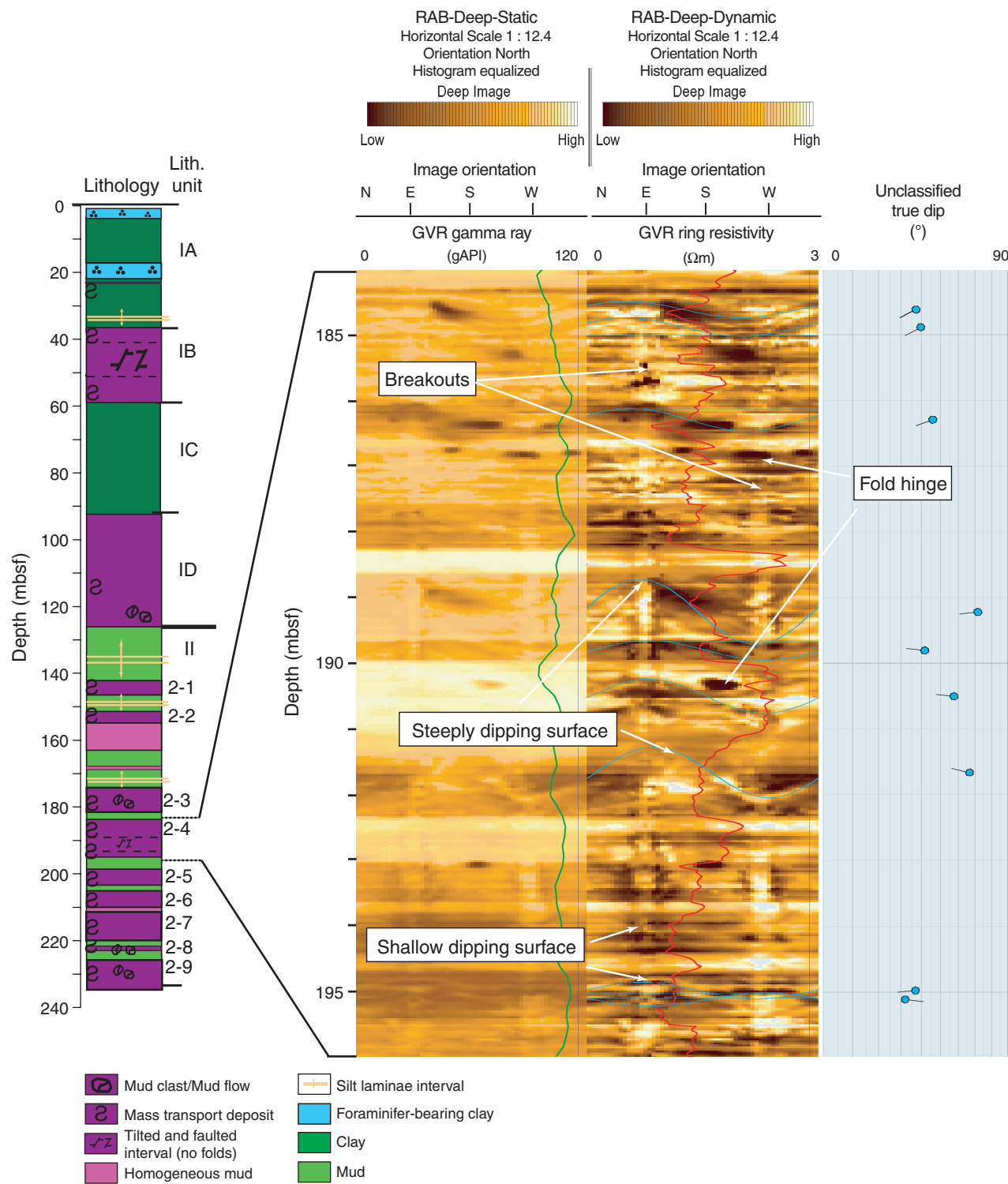


**Figure F47.** Advanced piston corer temperature (APCT) tool deployment from Core 308-U1322B-9H (80.0 mbsf). Solid line = recorded temperature; dashed line = equilibrium temperature. Equilibrium temperature is estimated from extrapolation of the temperature decay curve. See “Downhole” in “[Supplementary material](#).”

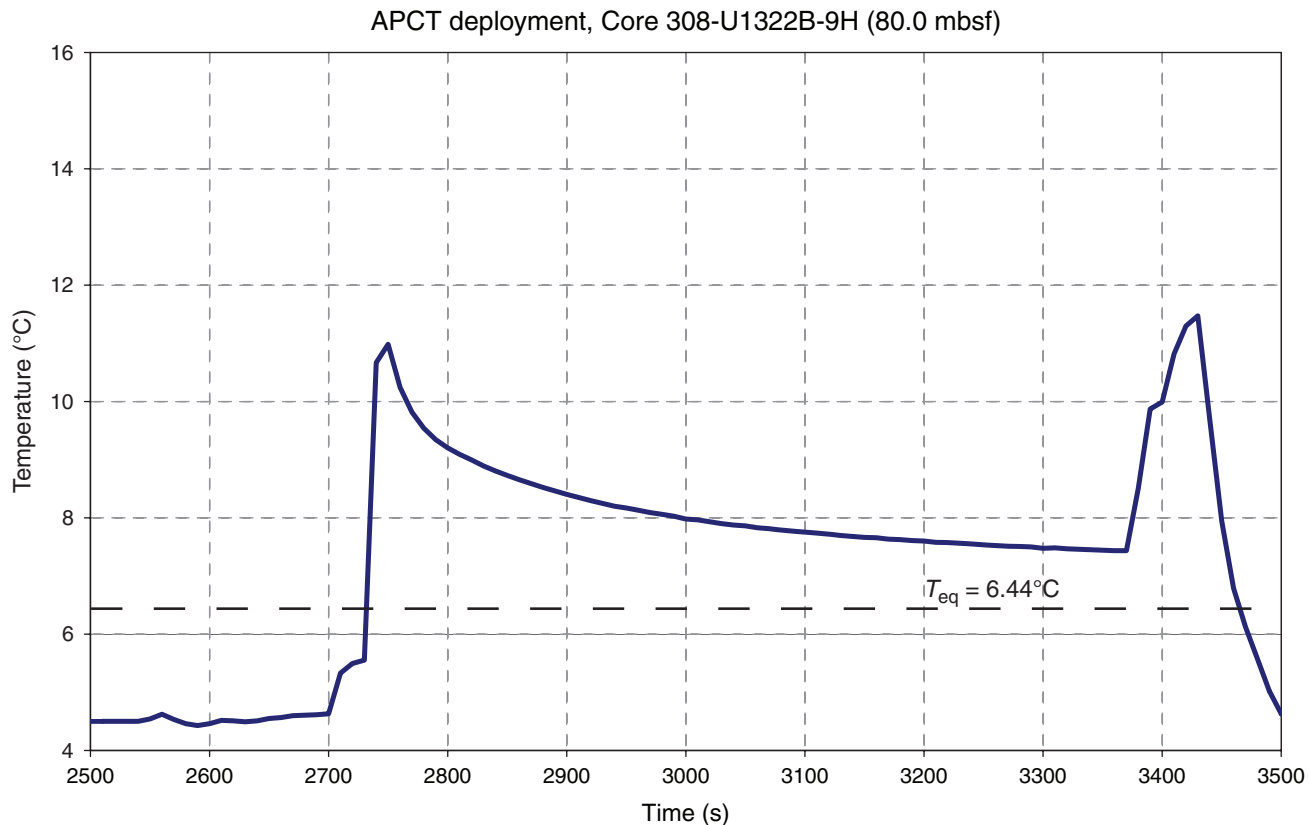


**Figure F48.** Advanced piston corer temperature (APCT) tool deployment from Core 308-U1322B-12H (108.5 mbsf). Solid line = recorded temperature; dashed line = equilibrium temperature. Equilibrium temperature is estimated from extrapolation of the temperature decay curve. See “Downhole” in “[Supplementary material](#).”

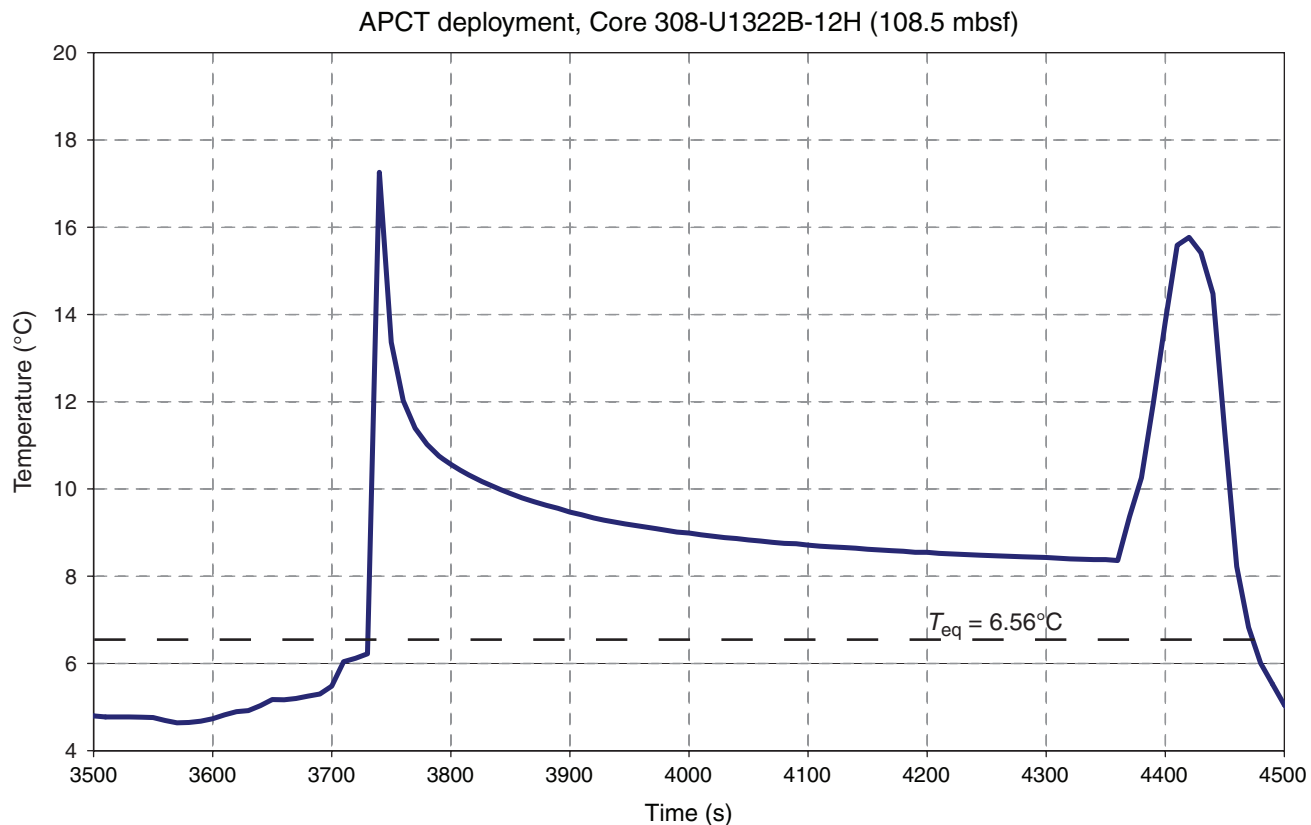


**Figure F49.** Temperature/dual pressure (T2P) probe pressure and temperature records from Deployment 17. CDT = central daylight time. See “Downhole” in “[Supplementary material](#).”

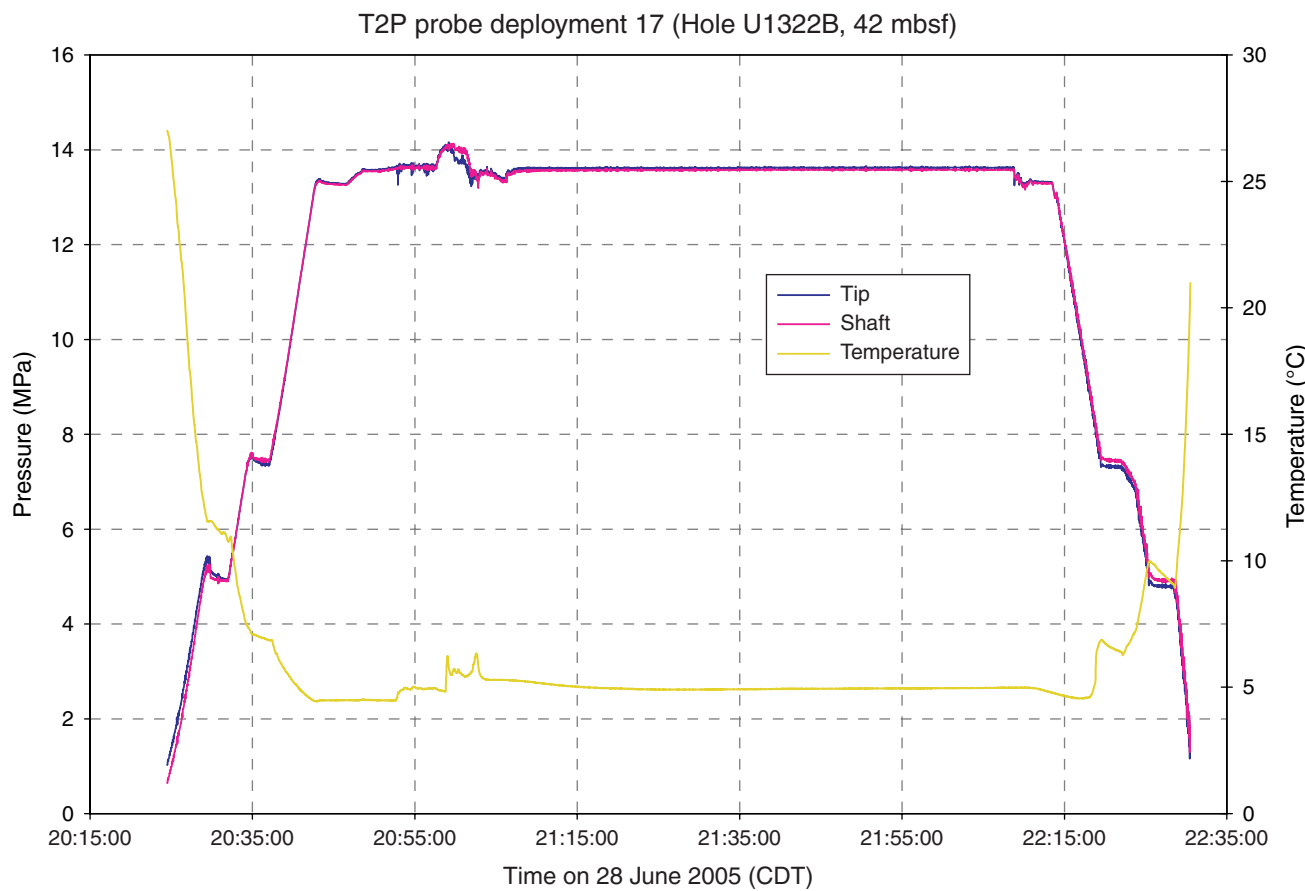


**Figure F50.** Temperature/dual pressure (T2P) probe pressure and temperature records from Deployment 19. CDT = central daylight time. See “Downhole” in “[Supplementary material](#).”

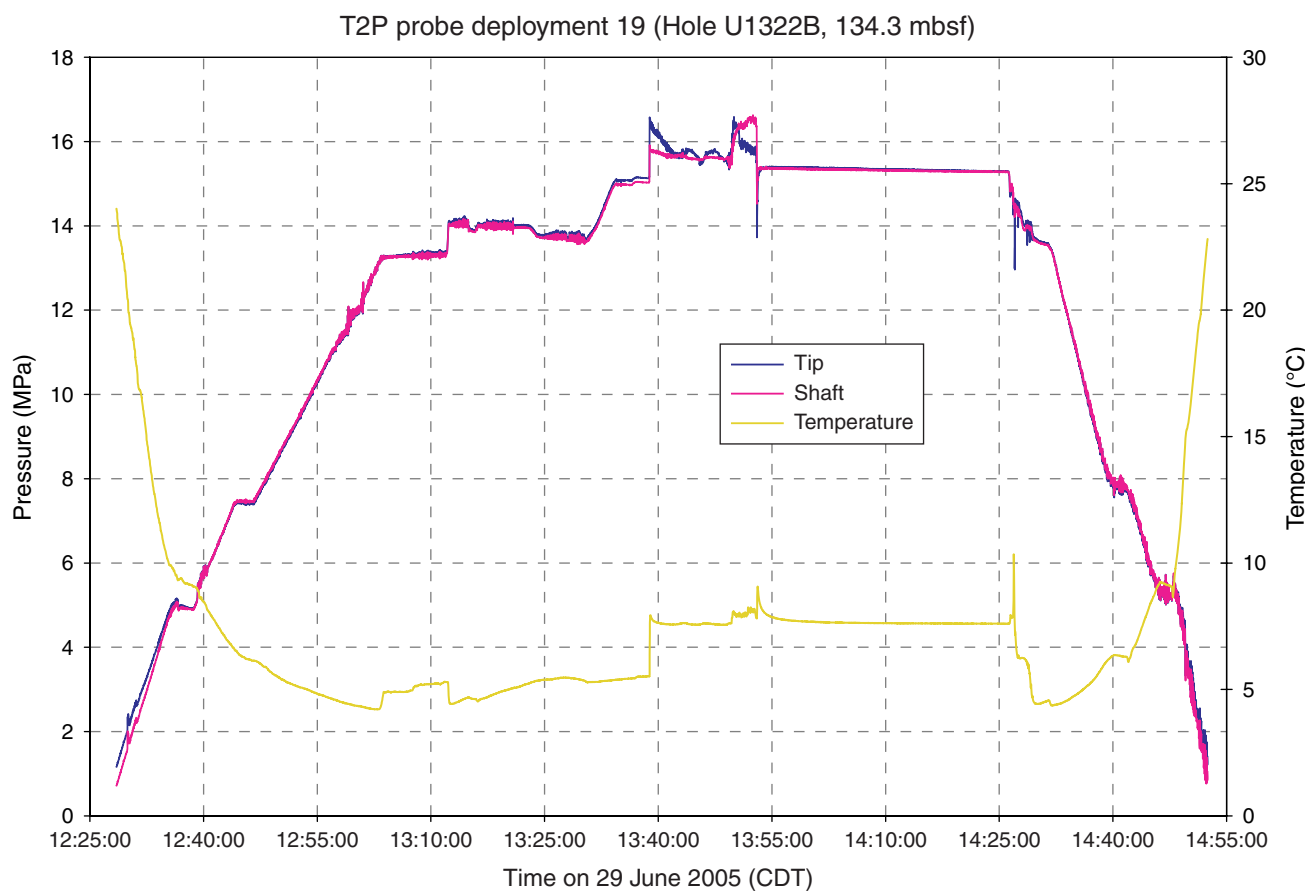


**Figure F51.** Temperature/dual pressure (T2P) probe pressure and temperature records from Deployment 20. CDT = central daylight time. See “Downhole” in “[Supplementary material](#).”

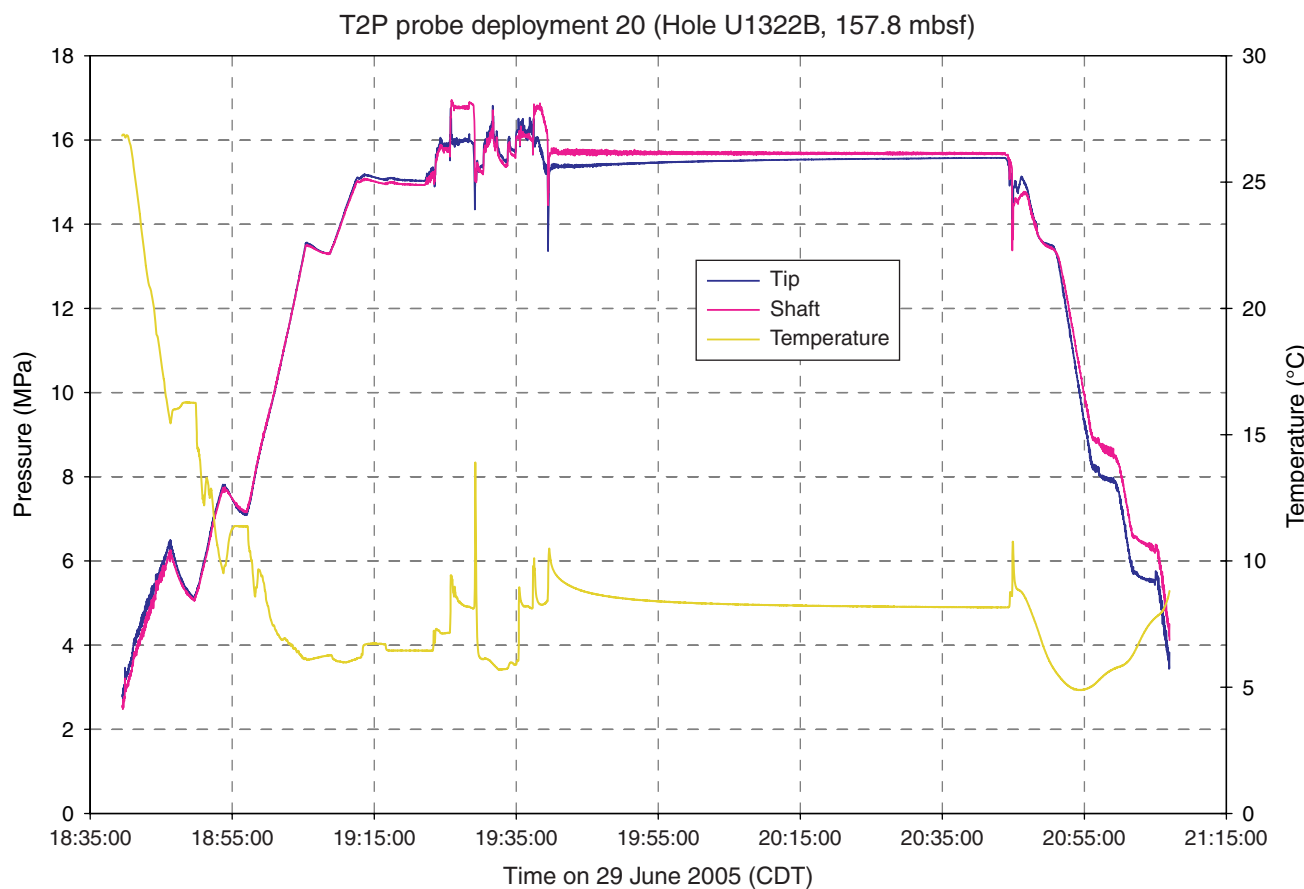


**Figure F52.** Temperature/dual pressure (T2P) probe pressure and temperature records from Deployment 23. CDT = central daylight time. See “Downhole” in “[Supplementary material](#).”

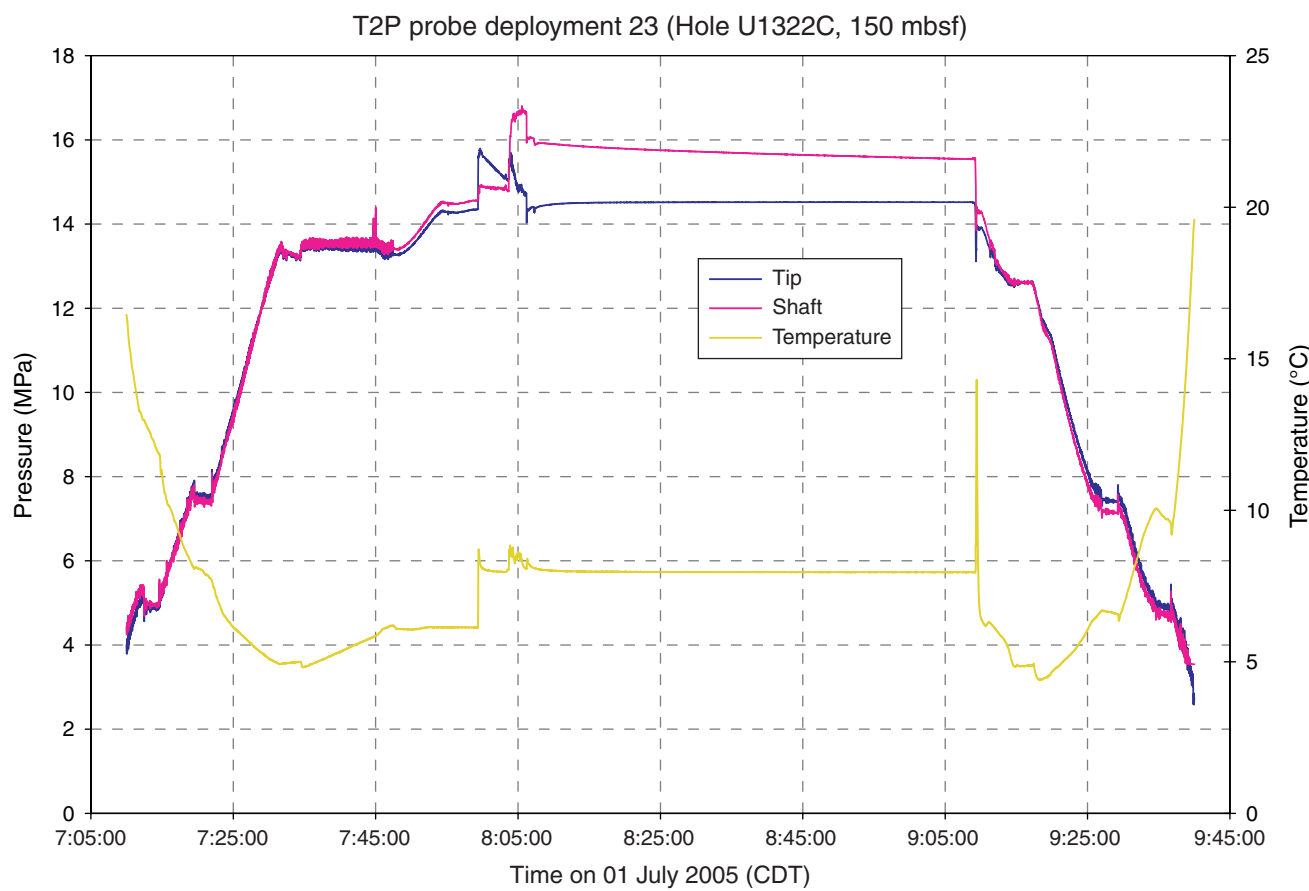


**Figure F53.** Temperature/dual pressure (T2P) probe pressure and temperature records from Deployment 24. CDT = central daylight time. See “Downhole” in “[Supplementary material](#).”

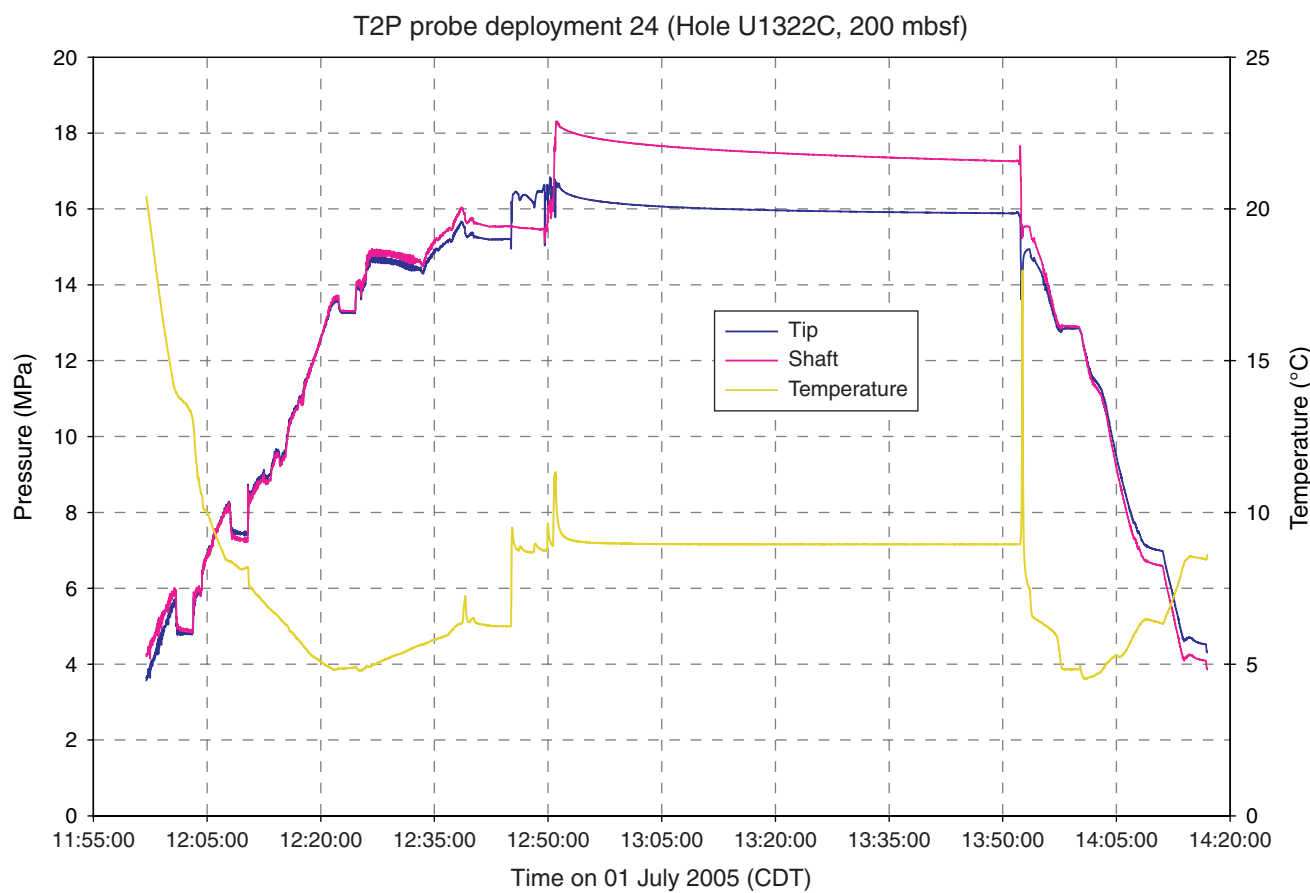


**Figure F54.** Temperature/dual pressure (T2P) probe pressure and temperature records from Deployment 25. CDT = central daylight time. See “Downhole” in “[Supplementary material](#).”

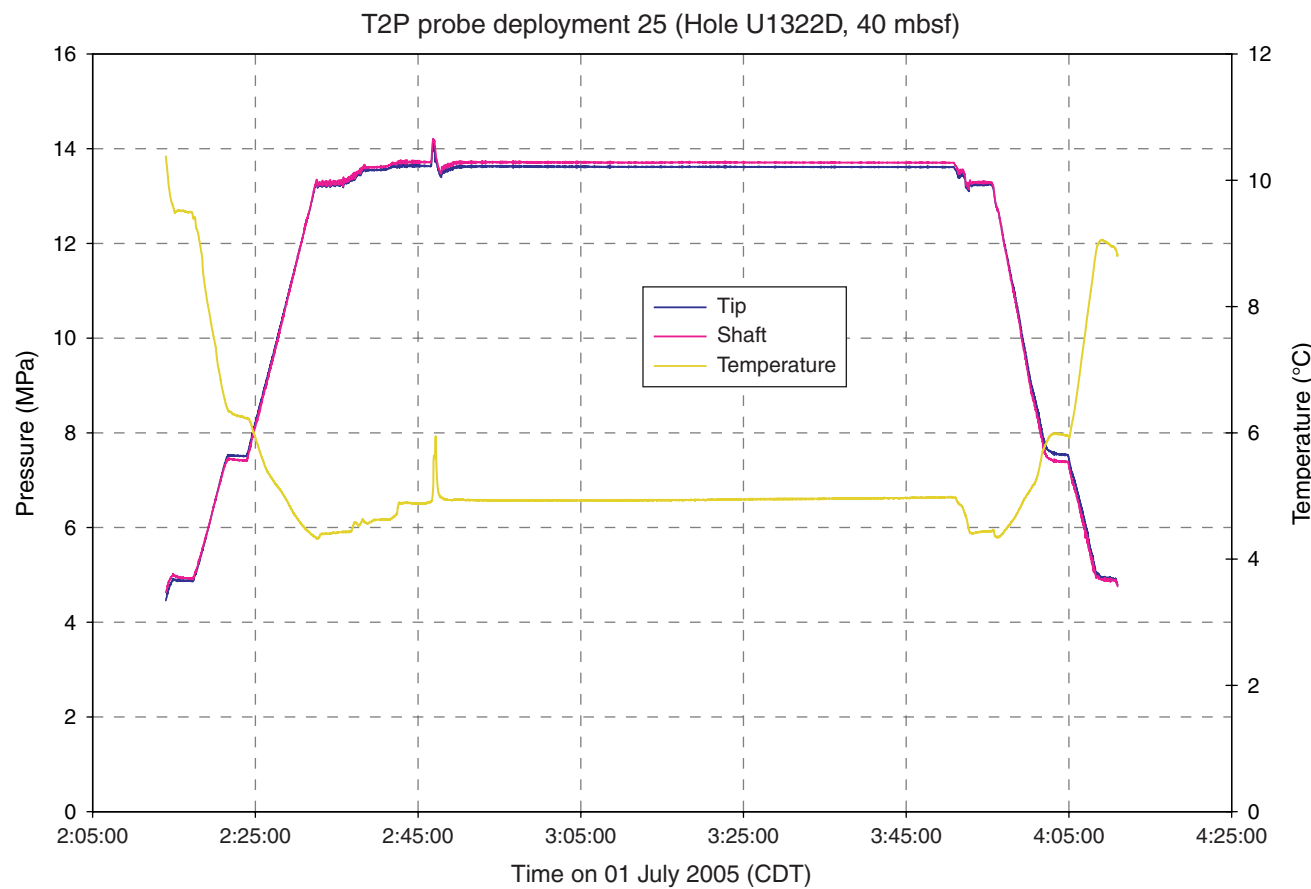


**Figure F55.** Temperature/dual pressure (T2P) probe pressure and temperature records from Deployment 26. CDT = central daylight time. See “Downhole” in “[Supplementary material](#).”

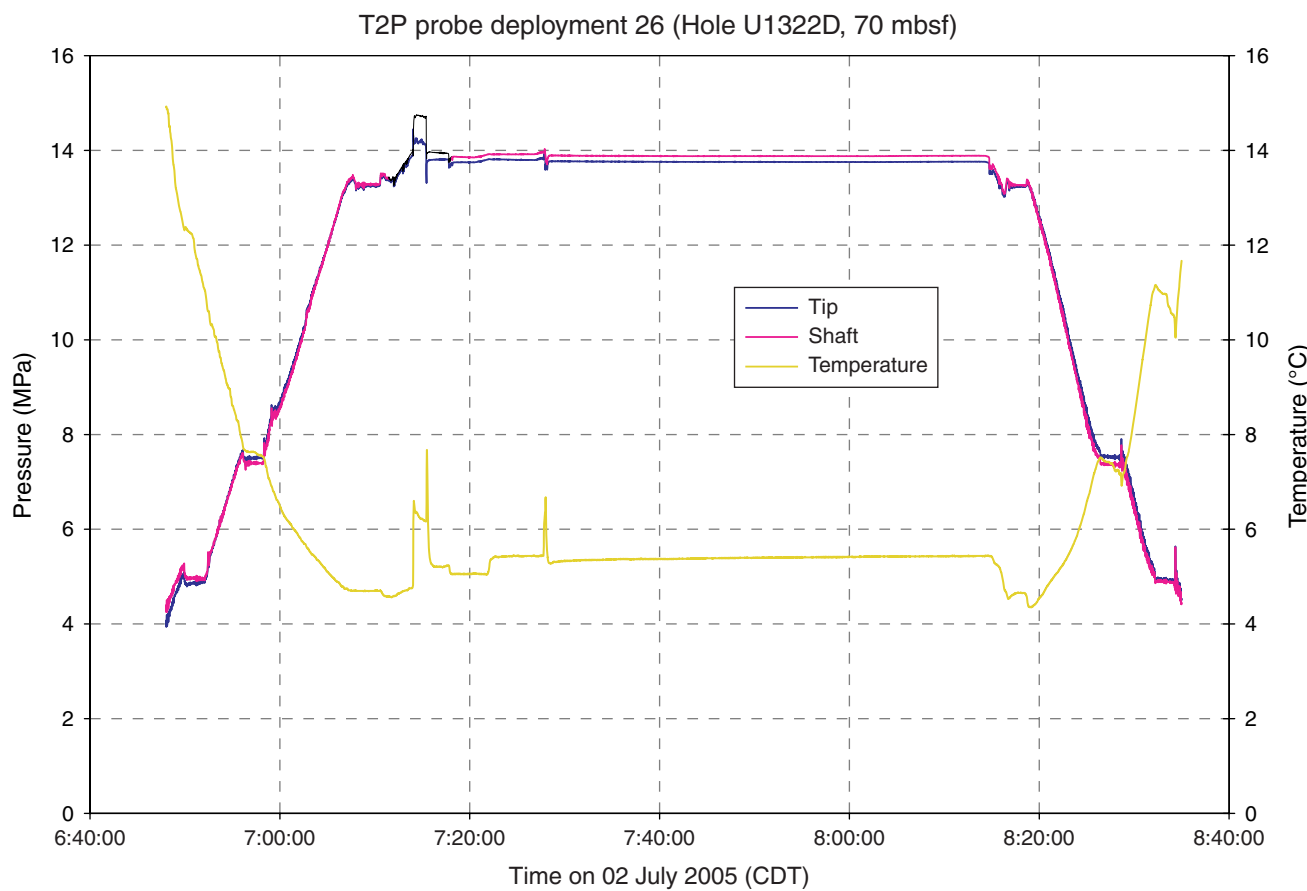


**Figure F56.** Temperature/dual pressure (T2P) probe pressure and temperature records from Deployment 27. CDT = central daylight time. See “Downhole” in “[Supplementary material](#).”

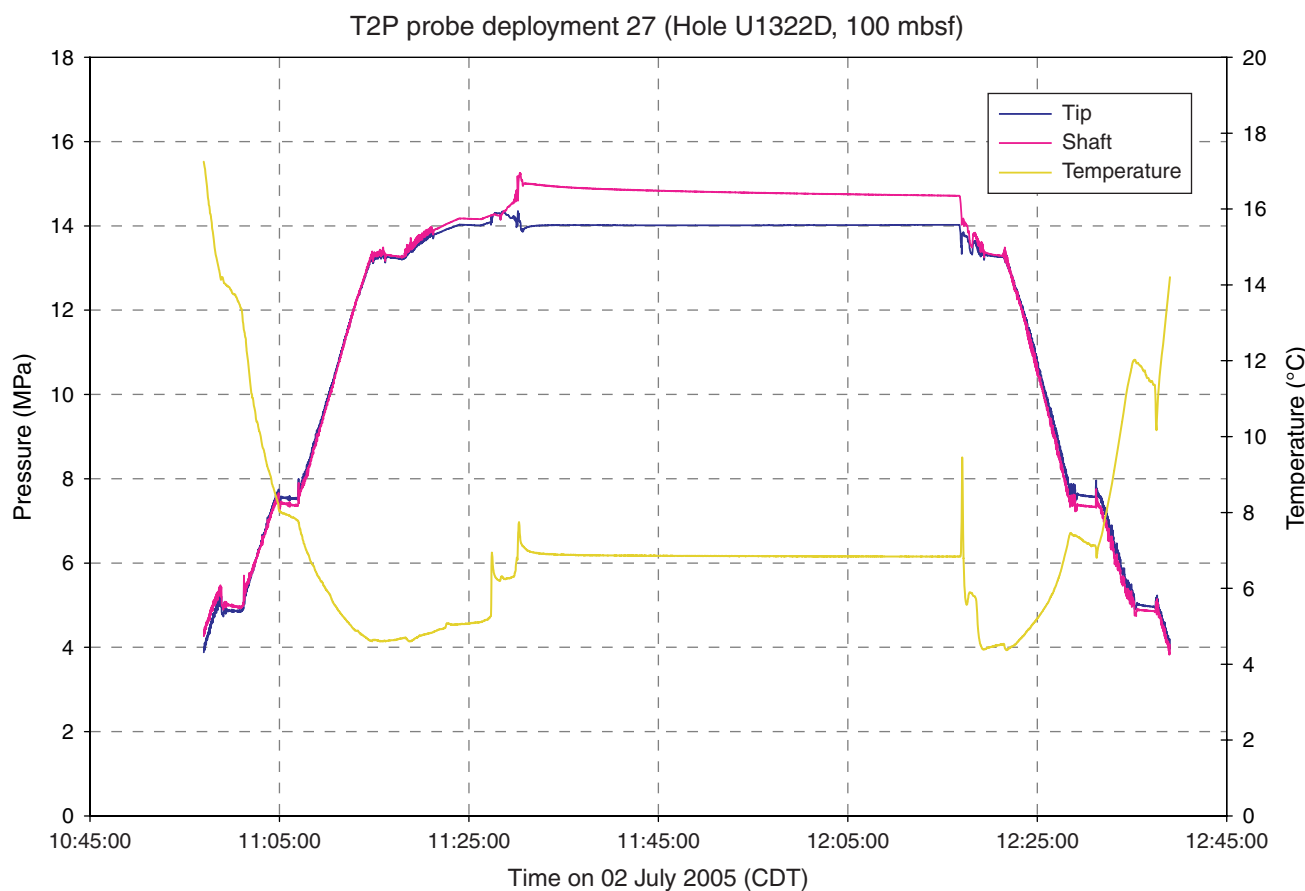


**Figure F57.** Temperature/dual pressure (T2P) probe pressure and temperature records from Deployment 28. CDT = central daylight time. See “Downhole” in “[Supplementary material](#).”

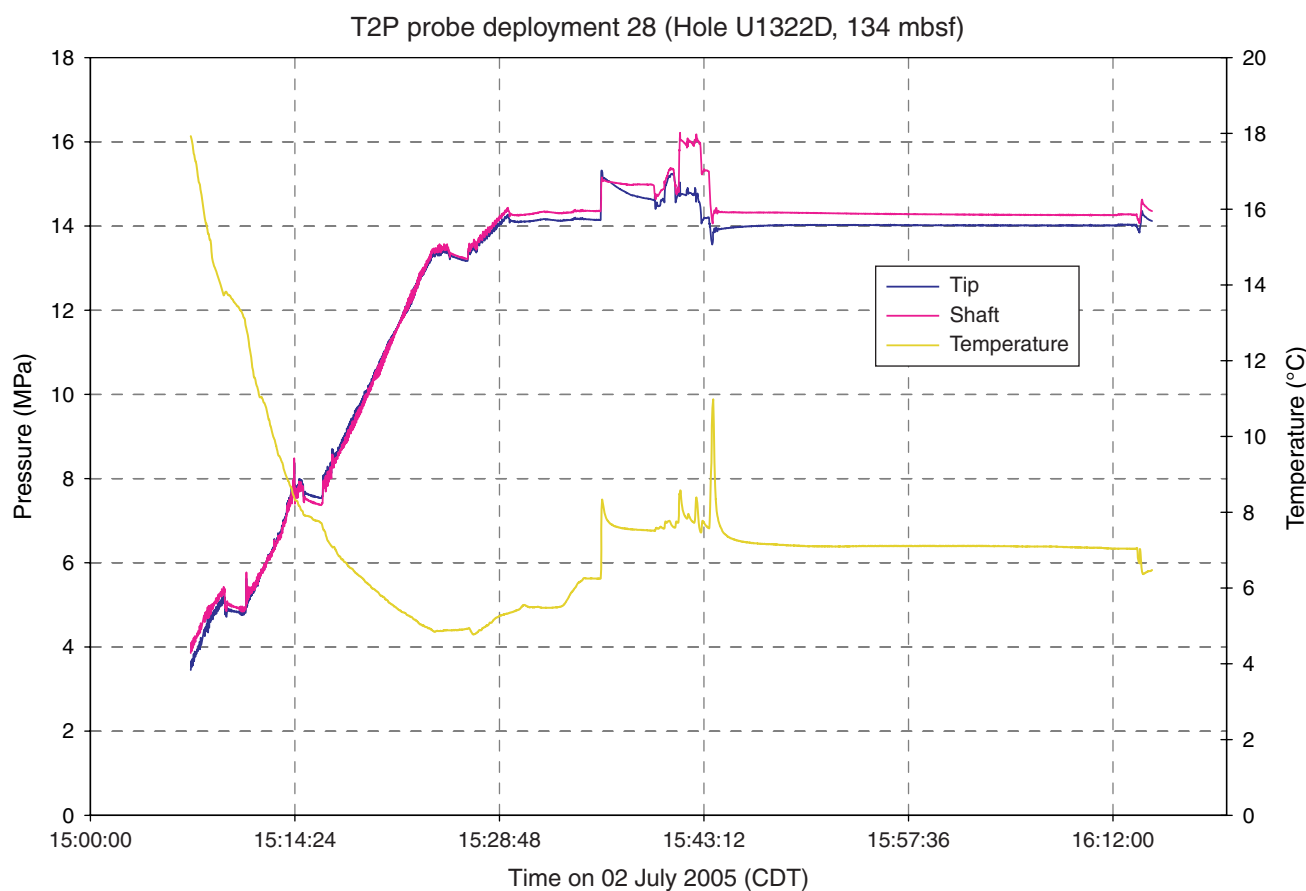


**Figure F58.** Davis-Villinger Temperature-Pressure Probe (DVTTP) pressure and temperature records from Deployment 16. GMT = Greenwich Mean Time. See “Downhole” in “[Supplementary material](#).”

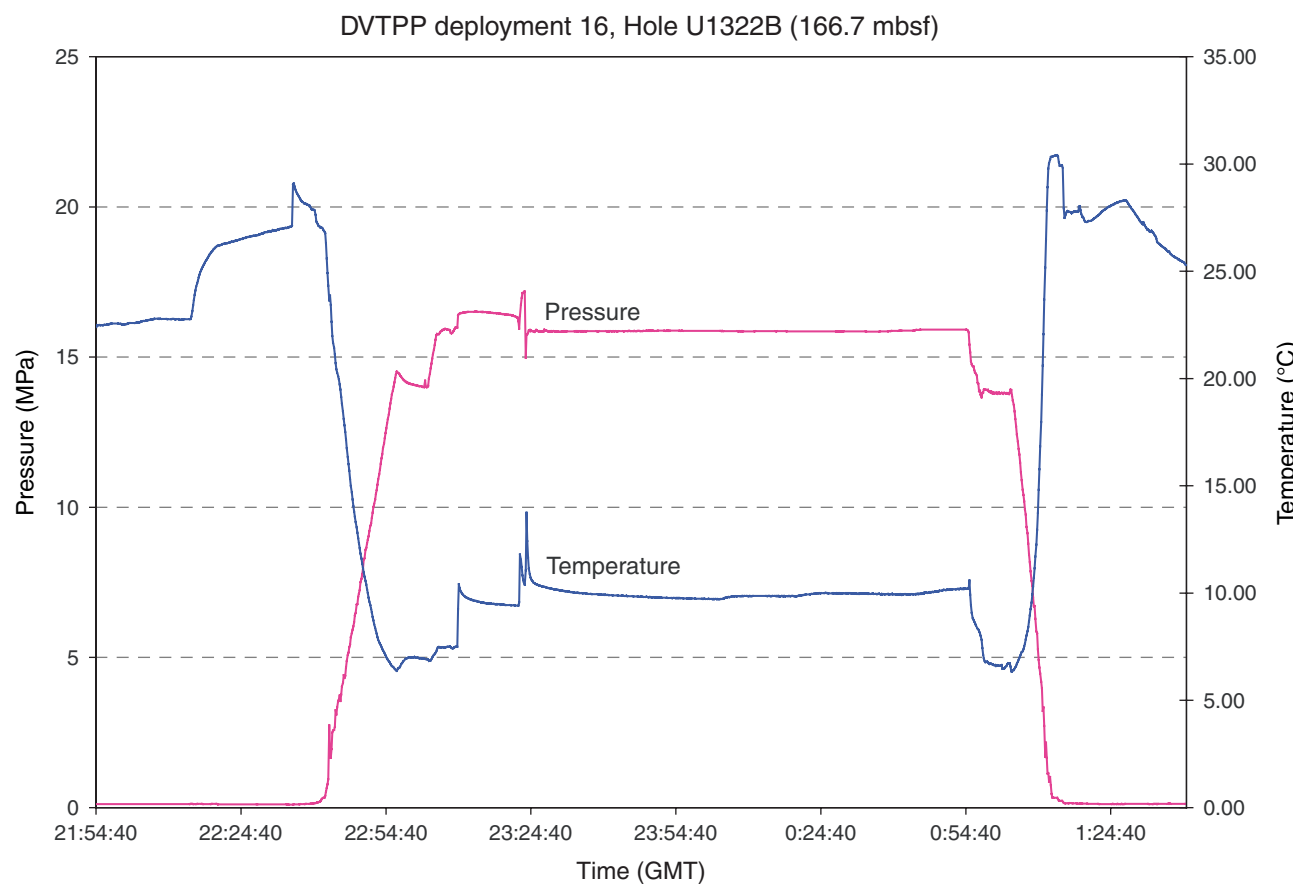


**Figure F59.** Davis-Villinger Temperature-Pressure Probe (DVTTP) pressure and temperature records from Deployment 17. GMT = Greenwich Mean Time. See “Downhole” in “[Supplementary material](#).”

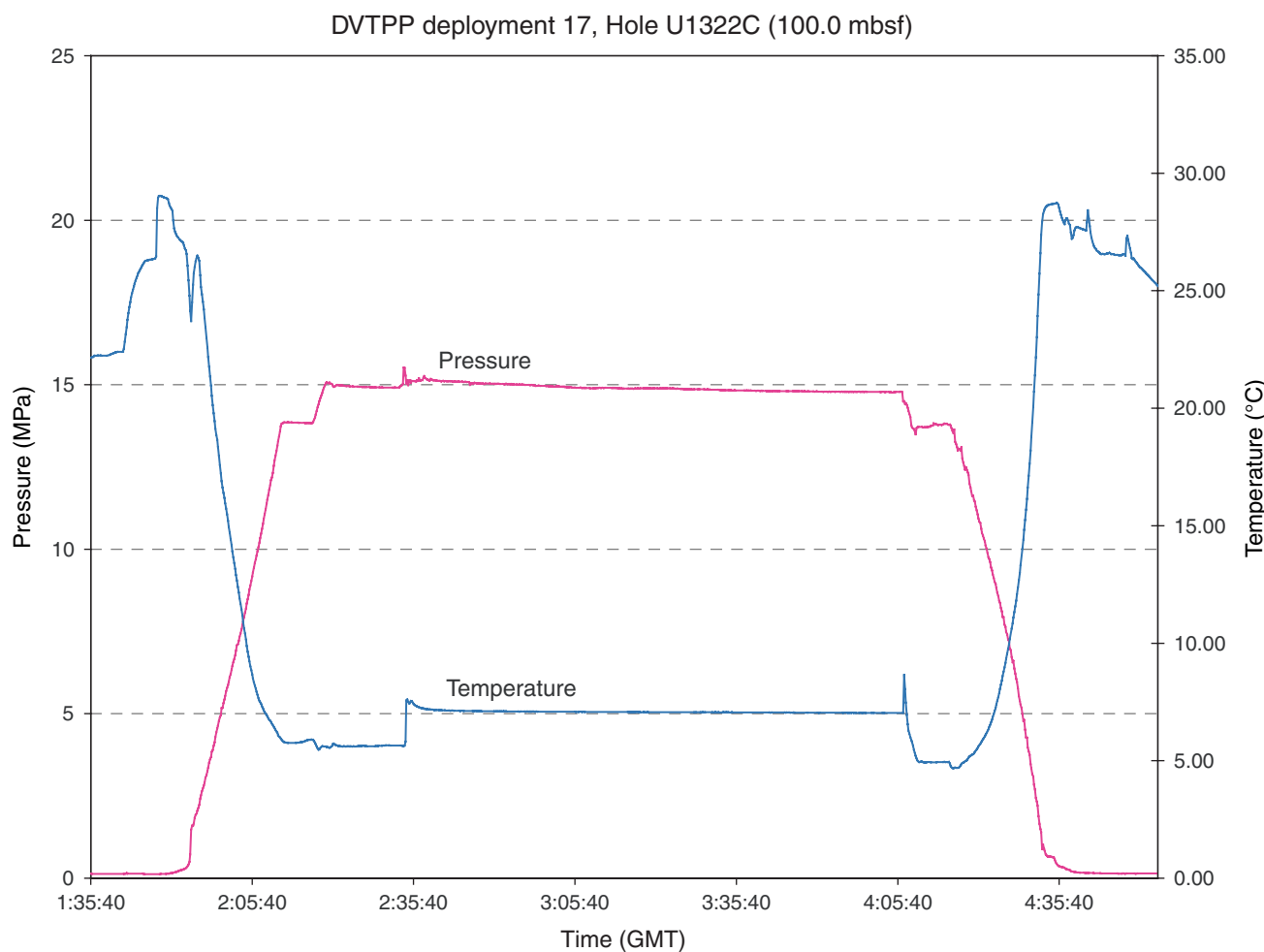


**Figure F60.** Davis-Villinger Temperature-Pressure Probe (DVTTP) pressure and temperature records from Deployment 18. GMT = Greenwich Mean Time. See “Downhole” in [“Supplementary material.”](#)

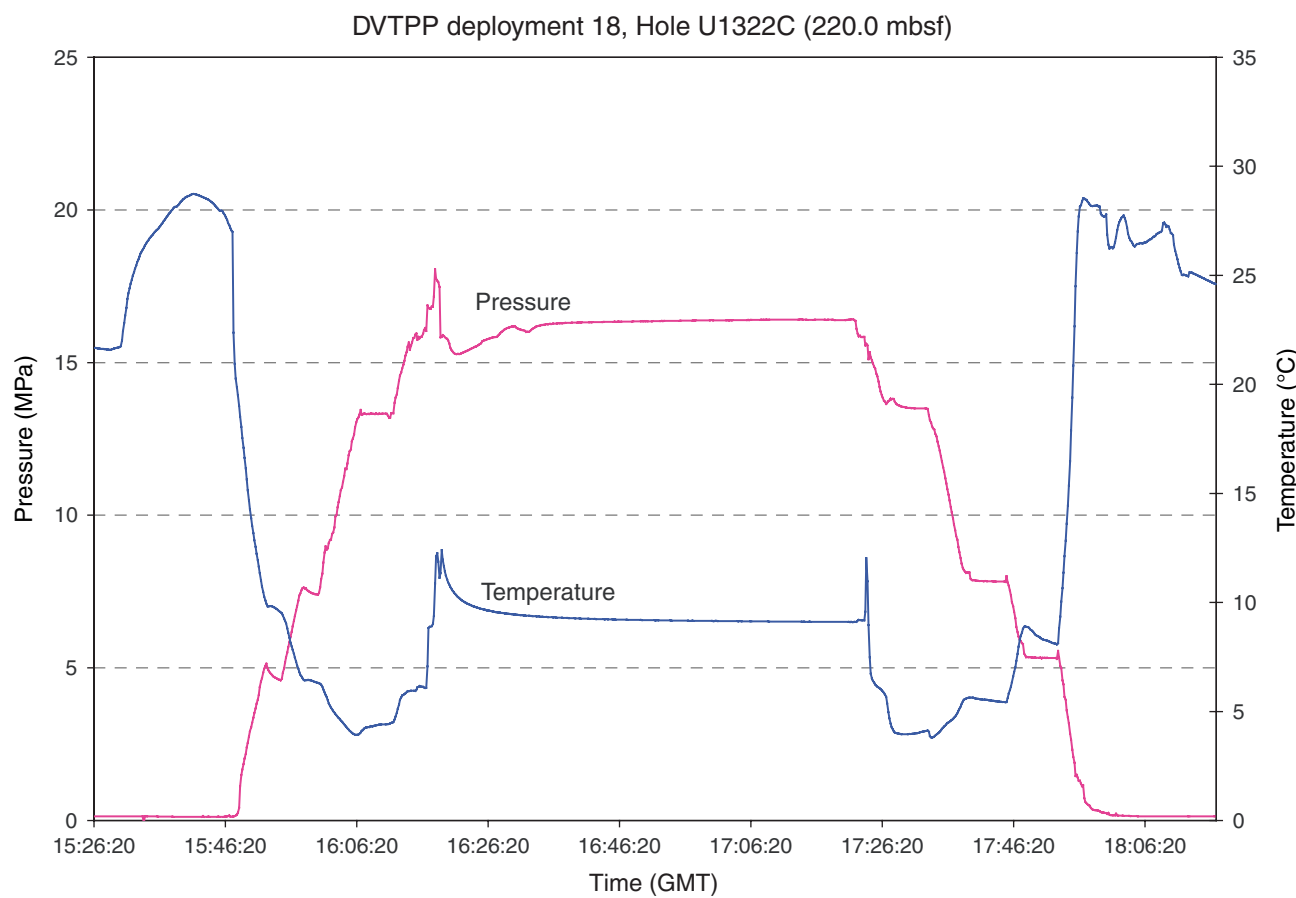


**Figure F61.** Davis-Villinger Temperature-Pressure Probe (DVTTP) pressure and temperature records from Deployment 19. GMT = Greenwich Mean Time. See “Downhole” in “[Supplementary material](#).”

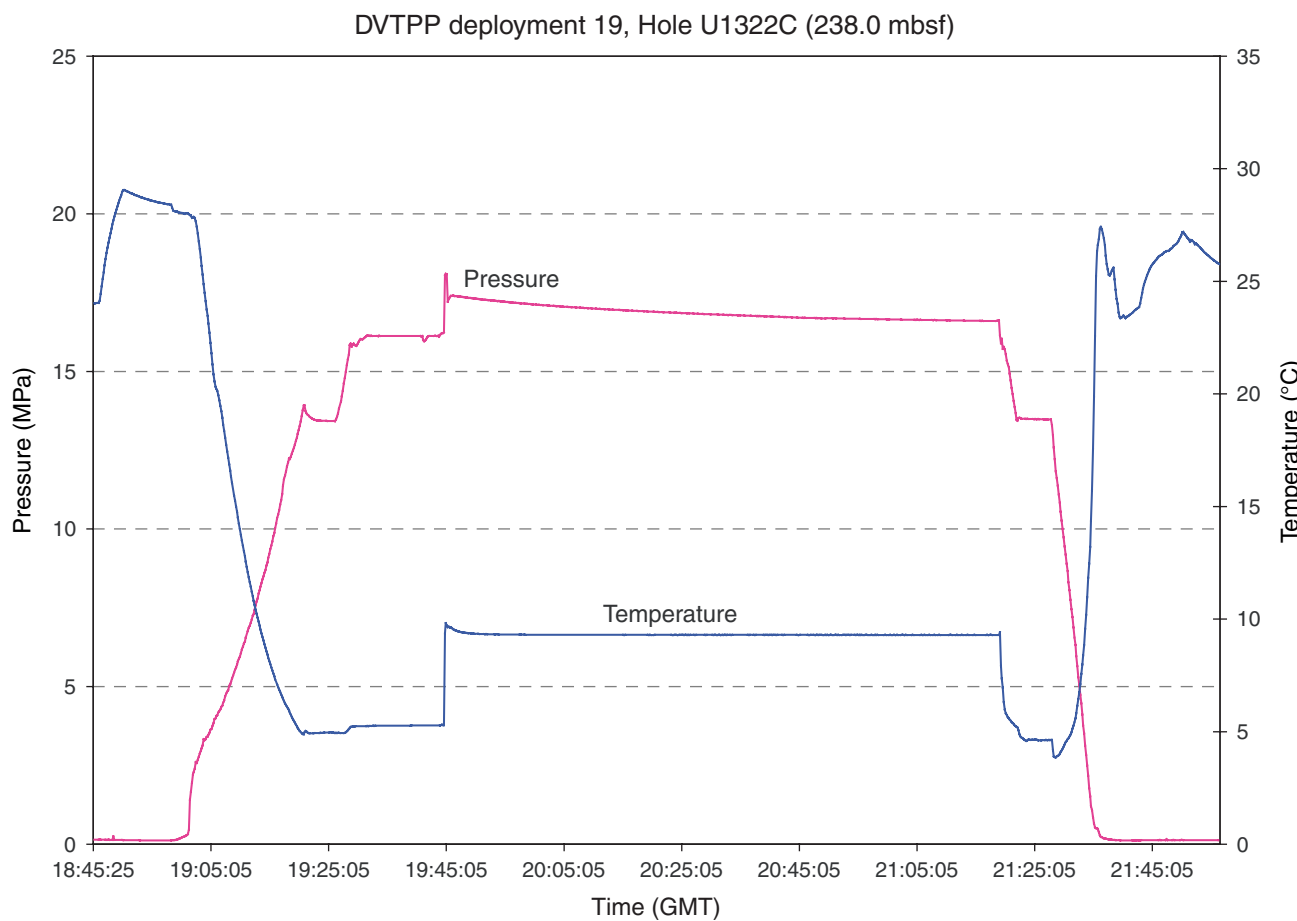


**Figure F62.** Davis-Villinger Temperature-Pressure Probe (DVTTP) pressure and temperature records from Deployment 20. GMT = Greenwich Mean Time. See “Downhole” in [“Supplementary material.”](#)

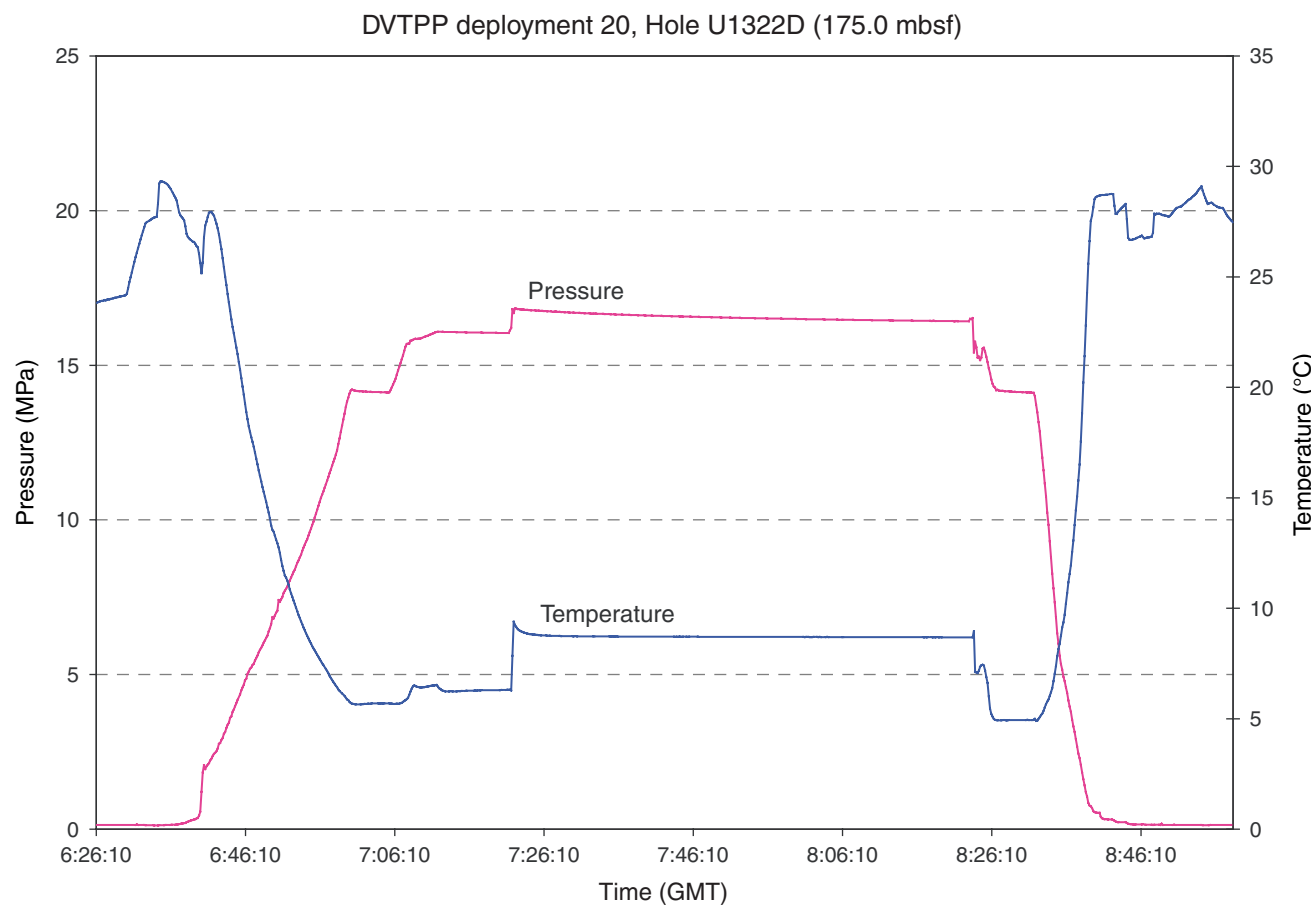


**Figure F63.** Equilibrium temperatures from the advanced piston corer temperature (APCT) tool, temperature/dual pressure (T2P) probe, and Davis-Villinger Temperature-Pressure Probe (DVTTP). Solid line = linear regression of the measured temperatures (average gradient =  $26.2^{\circ}\text{C}/\text{km}$ ).

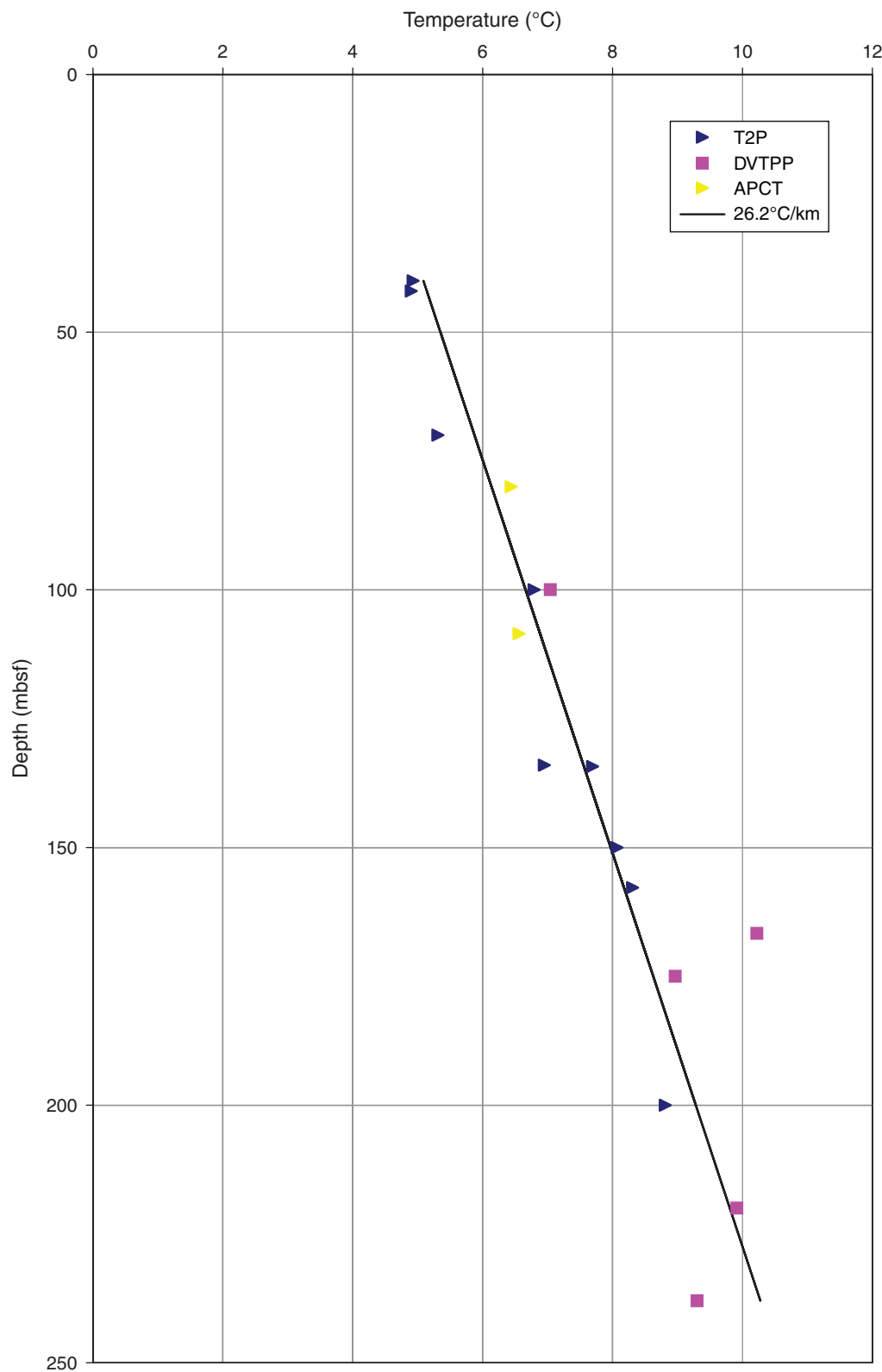


**Figure F64.** Maximum in situ pressures estimated from the last measurement on pressure dissipation curves from the temperature/dual pressure (T2P) probe and Davis-Villinger Temperature-Pressure Probe (DVTTP). Hydrostatic pressure is calculated for an assumed water density of 1.024 g/m<sup>3</sup>. Lithostatic stress is calculated for an assumed bulk density of 1.7 g/m<sup>3</sup>. All pressure data are referenced to the seafloor.

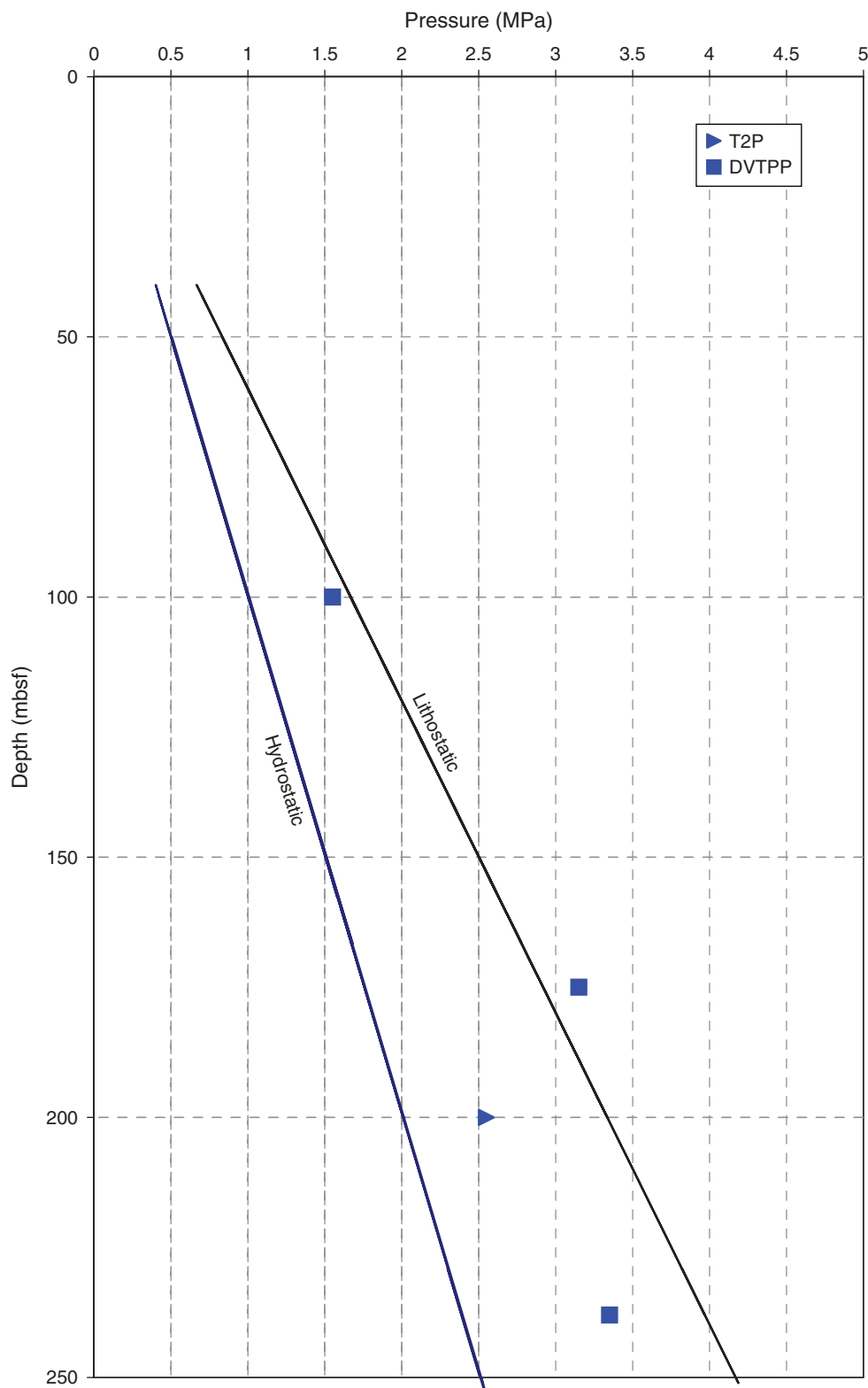


**Figure F65.** Maximum in situ pressures estimated from the last measurement on pressure dissipation curves from the temperature/dual pressure (T2P) probe and Davis-Villinger Temperature-Pressure Probe (DVTPP). Pressures interpreted from pressure rebound curves are also shown (open circles). Hydrostatic pressure is calculated for an assumed water density of 1.024 g/m<sup>3</sup>. Lithostatic stress is calculated for an assumed bulk density of 1.7 g/m<sup>3</sup>. All pressure data are referenced to the seafloor.

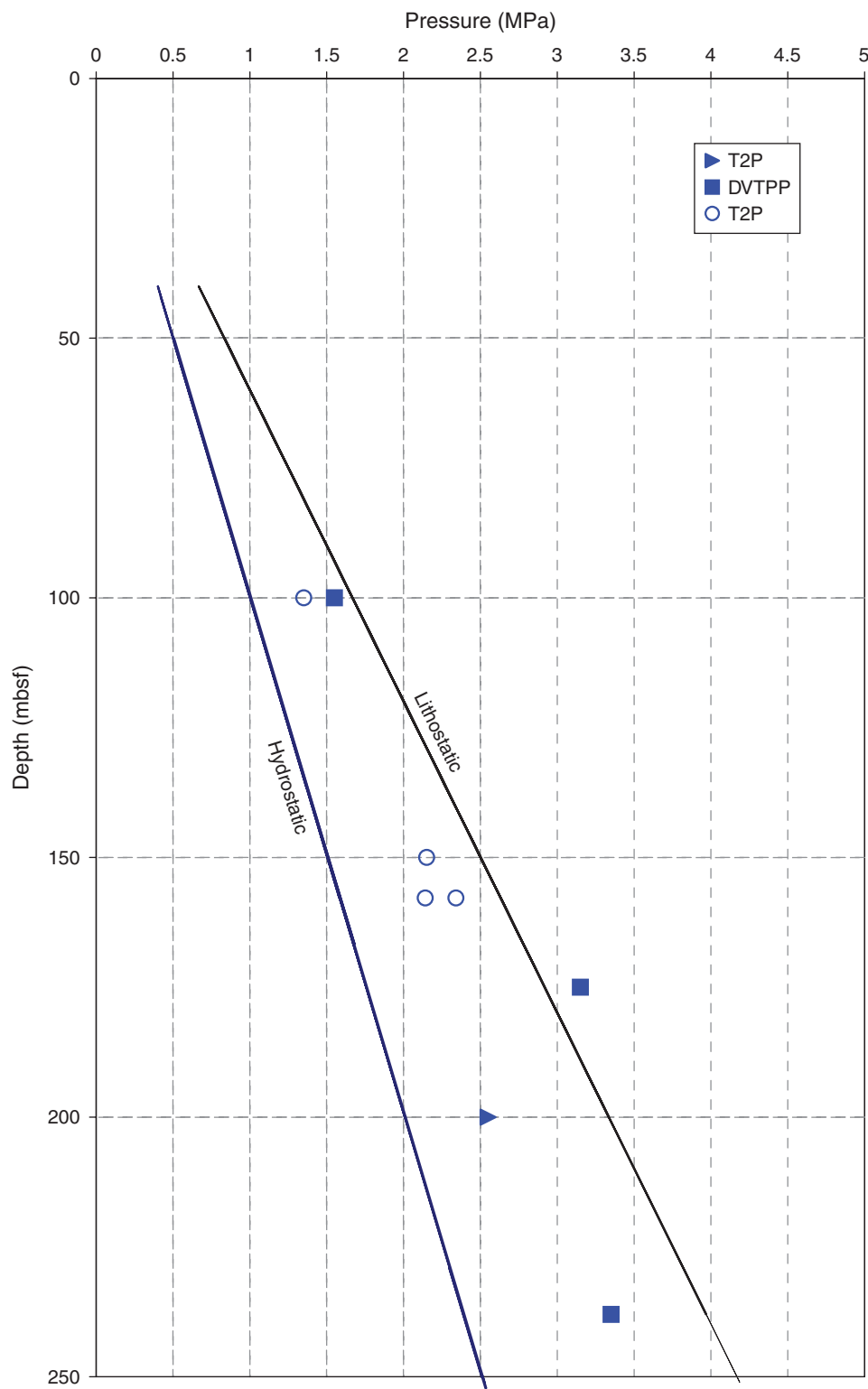


**Table T1.** Two-way traveltimes and depth of seismic surfaces, Sites U1322, U1323, and U1324.

Site U1324			Site U1323			Site U1322		
Reflector	TWT (ms)	Depth (mbsf)	Reflector	TWT (ms)	Depth (mbsf)	Reflector	TWT (ms)	Depth (mbsf)
SF	1412	0	SF	1687	0	SF	1766	0
S10	1458	35	S10	1731	33	S10	1806	30
S20	1548	105	S20	1812	97	S20	1880	88
S30	1623	165	S30	1938	197	S30	1926	124
S40-1324	1857	359	S40-1323	1961	216	S40-1322	1999	183
S50-1324	1971	459	S50-1323	2068	305	S50-1322	2021	201
S60-1324	2136	612				S60-1322	2049	224
						S70-1322	2078	247

Notes: TWT = two-way traveltimes. SF = seafloor. Time-depth calculation based on Equation E1.

**Table T2.** Coring summary, Hole U1322A.

Hole U1322A							
Core	Date (Jun 2005)	Local time (h)	Depth (mbsf)		Length (m)		Recovery (%)
			Top	Bottom	Cored	Recovered	
308-U1322A- 1-0	15	1330	0	238.0	0	0	0
			Cored totals:		0	0	0
					LWD/MWD		

Note: LWD/MWD = logging while drilling/measurement while drilling.



**Table T3.** Coring summary, Hole U1322B.**Hole U1322B**

Latitude: 28°5.9642'N  
 Longitude: 89°1.4995'W  
 Time on site (h): 49.00  
 Seafloor (drill pipe measurement from rig floor, mbrf): 1330.5  
 Distance between rig floor and sea level (m): 11  
 Water depth (drill pipe measurement from sea level, m): 1319.5  
 Total depth (drill pipe measurement from rig floor, mbrf): 1165  
 Total penetration (meters below seafloor, mbsf): 234.5  
 Total length of cored section (m): 234.5  
 Total core recovered (m): 236.79  
 Core recovery (%): 101  
 Total number of cores: 29

Core	Date (Jun 2005)	Local time (h)	Depth (mbsf)		Length (m)		Recovery (%)	Comments
			Top	Bottom	Cored	Recovered		
<b>308-U1322B-</b>								
1H	28	1220	0.0	4.0	4.0	4.10	102.50	Fluorescent microspheres
2H	28	1310	4.0	13.5	9.5	9.91	104.32	Fluorescent microspheres
3H	28	1345	13.5	23.0	9.5	8.71	91.68	Fluorescent microspheres
4H	28	1420	23.0	32.5	9.5	9.97	104.95	Fluorescent microspheres
5H	28	1455	32.5	42.0	9.5	9.78	102.95	Fluorescent microspheres; T2P probe at 1372.5 m
6H	28	1820	42.0	51.5	9.5	9.28	97.68	Fluorescent microspheres; pumped liner out
7H	28	1930	51.5	61.0	9.5	9.81	103.26	Fluorescent microspheres
8H	29	0035	61.0	70.5	9.5	9.91	104.32	Fluorescent microspheres; Tensor tool on at 2345 h
9H	29	0135	70.5	80.0	9.5	9.93	104.53	Fluorescent microspheres
10H	29	0215	80.0	89.5	9.5	10.10	106.32	Fluorescent microspheres
11H	29	0250	89.5	99.0	9.5	8.40	88.42	Fluorescent microspheres; broken liner, pump out; part of core liner between Sections 2 and 3 was crushed; the bottom sections were disturbed; cut out on the rig floor
12H	29	0400	99.0	108.5	9.5	9.47	99.68	
13H	29	0450	108.5	116.3	7.8	7.84	100.51	Florescent microspheres; core liner stuck in barrel, broken in a few places. Section 6 was okay, so samples were taken from it. Sections 5 and 7 were extruded on rig floor
14H	29	0555	116.3	124.8	8.5	8.55	100.59	
15H	29	0645	124.8	134.3	9.5	10.00	105.26	Fluorescent microspheres; Tensor tool out at 0640 h; T2P probe; changed all seals
16H	29	1100	134.3	142.0	7.7	7.78	101.04	Tensor tool in at 1010 h
17H	29	1150	142.0	149.9	7.9	8.02	101.52	Fluorescent microspheres; crushed liner; split liner
18H	29	1255	149.9	157.8	7.9	7.96	100.76	T2P probe at 1488.3 m
19H	29	1700	157.8	166.7	8.9	8.96	100.67	DVTTP at 1497.2 m; fluorescent microspheres
20H	29	2105	166.7	174.5	7.8	7.80	100.00	Tensor tool on at 2020 h
21H	29	2155	174.5	182.3	7.8	7.87	100.90	Fluorescent microspheres
22H	29	2300	182.3	189.0	6.7	6.75	100.75	
23H	29	2355	189.0	198.5	9.5	9.60	101.05	Fluorescent microspheres
24H	30	0105	198.5	201.7	3.2	3.23	100.94	
25H	30	0230	201.7	210.3	8.6	8.68	100.93	
26H	30	0335	210.3	214.1	3.8	3.83	100.79	Fluorescent microspheres
27H	30	0435	214.1	220.3	6.2	6.28	101.29	Tensor tool out at 0430 h
28H	30	0530	220.3	227.1	6.8	6.86	100.88	Tensor tool at 0445 h
29H	30	0640	227.1	234.5	7.4	7.41	100.14	
Cored totals:			234.5	236.79	100.98			

Note: T2P = temperature/dual pressure probe, DVTTP = Davis-Villinger Temperature-Pressure Probe.



**Table T4.** Coring summary, Hole U1322C.

**Hole U1322C**  
 Latitude: 28°5.9640'N  
 Longitude: 89°1.5228'W  
 Time on site (h): 32.23  
 Seafloor (drill pipe measurement from rig floor, mbrf): 1330  
 Distance between rig floor and sea level (m): 11.1  
 Water depth (drill pipe measurement from sea level, m): 1318.9  
 Total depth (drill pipe measurement from rig floor, mbrf): 1566  
 Total penetration (meters below seafloor, mbsf): 236  
 Total length of cored section (m): 4.5  
 Total core recovered (m): 231.5  
 Core recovery (%): 101  
 Total number of cores: 1

Core	Date (2005)	Local time (h)	Depth (mbsf)		Length (m)		Recovery (%)	Comments
			Top	Bottom	Cored	Recovered		
308-U1322C-								
1H	Jun 30	1150	0.0	4.5	4.5	4.53	100.67	
2-0	Jun 30	1330	4.5	50.0				T2P probe at 1380.0 m
2-1	Jun 30	1700	50.0	75.0				T2P probe at 1405.0 m
2-2	Jun 30	2045	75.0	100.0				DVTTP at 1430 m (100 mbsf)
2-3	Jul 1	0140	100.0	150.0				T2P probe
2-4	Jul 1	0625	150.0	200.0				T2P probe
2-5	Jul 1	1030	200.0	220.0				DVTTP
2-6	Jul 1	1345	220.0	236.0				DVTTP at 1566.0 m
			Cored totals:		4.5	4.53	100.67	

Note: T2P = temperature/dual pressure probe, DVTTP = Davis-Villinger Temperature-Pressure Probe.

**Table T5.** Operations coring summary, Hole U1322D.

**Hole U1322D**  
 Latitude: 28°5.9753'N  
 Longitude: 89°1.5104'W  
 Time on site (h): 30.10  
 Seafloor (drill pipe measurement from rig floor, mbrf): 1330  
 Distance between rig floor and sea level (m): 11.1  
 Water depth (drill pipe measurement from sea level, m): 1318.9  
 Total depth (drill pipe measurement from rig floor, mbrf): 1505  
 Total penetration (meters below seafloor, mbsf): 175  
 Total length of cored section (m): 26.8  
 Total core recovered (m): 27.21  
 Core recovery (%): 101  
 Total number of cores: 3

Core	Date (Jul 2005)	Local time (h)	Depth (mbsf)		Length (m)		Recovery (%)	Comments
			Top	Bottom	Cored	Recovered		
308-U1322D-								
1-0	1	2100	0.0	40.0				T2P probe
1-H	1	2355	40.0	49.5	9.5	9.58	100.84	
2-1	2	125	49.5	70.0				T2P probe
2-H	2	425	70.0	79.5	9.5	9.78	102.95	
3-2	2	530	79.5	100.0				T2P probe
3-H	2	830	100.0	107.8	7.8	7.85	100.64	
4-3	2	945	107.8	134.0				T2P probe
4-4	2	1345	134.0	175.0				DVTTP at 1505 m (175 mbsf)
			Cored totals:		26.8	27.21	101.53	

Note: T2P = temperature/dual pressure probe, DVTTP = Davis-Villinger Temperature-Pressure Probe.



**Table T6.** Lithostratigraphic units, Hole U1322B.

Unit	Top		Bottom		Thickness (m)
	Core, section, interval (cm)	Depth (mbsf)	Core, section, interval (cm)	Depth (mbsf)	
308-U1322B-					
I	1H-1, 0	0.00	15H-1, 100	125.80	125.80
IA	1H-1, 0	0.00	5H-4, 43	37.43	37.43
IB	5H-4, 43	37.43	7H-5, 110	58.60	21.17
IC	7H-5, 110	58.60	11H-3, 0	91.31	32.71
ID	11H-3, 0	91.31	15H-1, 100	125.80	34.49
II	15H-1, 100	125.80	29H-CC, base	234.50	108.70

**Table T7.** Lithostratigraphic Unit II, Hole U1322B.

Interval	Depth (mbsf)	Comments
Coherent with silt laminae	125.80–142.00	Laminated clay couples with black mottled bands and silt laminae
MTD 2-1	142.00–145.82	Folds and small-scale normal faults; homogenized zone at the base
Coherent with silt laminae	145.82–151.40	Laminated clay couples with black mottled bands with silt laminae
MTD 2-2	151.40–154.83	Recumbent folds and small-scale normal and reverse faults; homogenized zone in the upper and lower part
Homogenized zone		Homogenized, relatively soft interval; transitional zone to coherent layers in the lower part
Coherent layers		Laminated clay couples with black mottled bands with silt laminae
MTD 2-3	173.34–180.1	Several-meter-scale folds; homogenized zone in the lower part
	180.1–183.6	Laminated clay couples with black mottled bands
MTD 2-4 upper	183.6–188.67	Inclined layers; recumbent folds are shown by faint dark mud laminae
MTD 2-4 middle		Slightly inclined ( $\sim 10^\circ$ ) layers; a few microscale normal faults; no recumbent folds or homogenized zone
MTD 2-4 lower	193.75–194.75	Recumbent folds
MTD 2-5	198.50–201.73	Laminated clay couples with black mottled bands
		Slightly tilted in the upper part, recumbent and inclined beds in the lower part
		Faint-laminated mud couples
MTD 2-6	205.55–210.00	Basically homogeneous mud with some recumbent folds
MTD 2-7	210.80–219.28	Inclined interval with some recumbent folds
MTD 2-8	222.79–224.18	Homogenized zone with a few small-scale folds and mud clasts in lower part
		Laminated clay couples
MTD 2-9	225.8	Inclined beds, recumbent folds, and listric normal faults; mud clasts contained

Note: MTD = mass transport deposit.

**Table T8.** Relative abundances of planktonic foraminifers, Hole U1322B.

Core, section, interval (cm)	Depth (mbsf)	Sample code	Zone	Age	Relative abundance data by species												Comments	
					Z	Y1	Y2	Y3	Y5	Y6	Globorotalia menardii	Globorotalia inflata	Globorotalia heterosa	Globorotalia tenuis	Globorotalia truncatulinoides	Globorotalia sphaerula		
308-U1322B-	1H-CC, 0–10	PAL	Pleistocene	>63							Globigerinella inflata	Globigerinella sphaerulata	Globigerinella sphaerulata	Globigerinella inflata	Globigerinella inflata	Globigerinella inflata	Globigerinella inflata	Globigerinella inflata
											R	T	F	R	R	B	R	G. inflata reworked
	2H-CC, 17–27	PAL			M	C					R	T	F	R	R	B	R	
	3H-CC, 6–16	PAL			VG	F					R	T	F	R	R	F	R	
	4H-CC, 29–34	PAL			VG	C					T	F	C	C	R	F	R	
	5H-CC, 24–29	PAL			VG	F					T	F	F	R	R	F	R	
	6H-CC, 41–46	PAL			VG	C					T	F	F	R	R	F	R	
	7H-CC, 22–27	PAL			VG	C					T	F	F	R	R	F	R	
	8H-CC, 25–30	PAL			VG	C					T	F	F	R	R	F	R	
	9H-CC, 45–50	PAL			VG	C					T	F	F	R	R	F	R	
	10H-CC, 29–34	PAL			VG	C					T	F	F	R	R	F	R	
	11H-CC, 56–61	PAL			VG	C					T	F	F	R	R	F	R	
	12H-CC, 28–33	PAL			VG	C					T	F	F	R	R	F	R	
	13H-CC, 63–68	PAL			VG	C					T	F	F	R	R	F	R	
	14H-CC, 43–48	PAL			VG	C					T	F	F	R	R	F	R	Abundant charcoal
	15H-1, 95–99	PAL			VG	C					T	F	F	R	R	F	R	Rare
	15H-CC, 47–52	PAL			VG	C					T	F	F	R	R	F	R	Abundant charcoal
	16H-CC, 41–46	PAL			VG	C					T	F	F	R	R	F	R	Mica
	17H-CC, 40–45	PAL			VG	C					T	F	F	R	R	F	R	Mica + charcoal
	18H-CC, 31–36	PAL			VG	C					T	F	F	R	R	F	R	Charcoal +
	19H-CC, 28–33	PAL			VG	C					T	F	F	R	R	F	R	Charcoal +
	20H-CC, 46–51	PAL			VG	C					T	F	F	R	R	F	R	Silt sand
	21H-CC, 24–29	PAL			VG	C					T	F	F	R	R	F	R	Charcoal
	22H-CC, 33–38	PAL			VG	C					T	F	F	R	R	F	R	Silt sand
	23H-CC, 37–42	PAL			VG	C					T	F	F	R	R	F	R	Mica + silt
	24H-CC, 18–23	PAL			VG	C					T	F	F	R	R	F	R	Silt + many sea urchin spines
	25H-CC, 33–38	PAL			VG	C					T	F	F	R	R	F	R	Silt + mica
	26H-CC, 21–26	PAL			VG	C					T	F	F	R	R	F	R	Silt + mica
	27H-CC, 23–28	PAL			VG	C					T	F	F	R	R	F	R	Mica + silt + charcoal
	28H-CC, 33–38	PAL			VG	C					T	F	F	R	R	F	R	Charcoal
	29H-CC, 39–44	PAL			VG	C					T	F	F	R	R	F	R	Charcoal

Notes: Abundance: A = abundant, C = common, F = frequent, R = rare, VR = very rare, T = trace, B = barren. Preservation: VG = very good, G = good, M = moderate. PAL = paleontological sample.





**Table T9.** Relative abundances of benthic foraminifers, Hole U1322B. (Continued on next page.)

Notes: Abundance: A = abundant, C = common, F = frequent, R = rare, VR = very rare, T = trace, B = barren. Preservation: VG = very good, G = good, M = moderate. PAL = paleontological sample. SE = shelf edge.

Table T9 (continued).

Core, section, interval (cm)	Depth (mbsf)	Sample code	Zone	Age	Comments					
					Z	Y1	Y2	Y3	Y5	Y6
308-U1322B-1H-CC, 0–10	4.00	PAL		Pleistocene	R	R	R	R	R	R
2H-CC, 17–27	13.81				R	R	R	R	R	R
3H-CC, 6–16	22.11				F	F	F	F	F	F
4H-CC, 29–34	32.92				R	R	R	R	R	R
5H-CC, 24–29	42.23				R	R	R	R	R	R
6H-CC, 41–46	51.02				R	R	R	R	R	R
7H-CC, 22–27	61.26				R	R	R	R	R	R
8H-CC, 25–30	70.86				R	R	R	R	R	R
9H-CC, 45–50	80.38				R	R	R	R	R	R
10H-CC, 29–34	90.05				R	R	R	R	R	R
11H-CC, 56–61	97.85				R	R	R	R	R	R
12H-CC, 28–33	108.42				R	R	R	R	R	R
13H-CC, 63–68	116.29				R	R	R	R	R	R
14H-CC, 43–48	124.80				R	R	R	R	R	R
15H-1, 95–99	125.75				R	R	R	R	R	R
15H-CC, 47–52	134.75				R	R	R	R	R	R
16H-CC, 41–46	142.03				R	R	R	R	R	R
17H-CC, 40–45	149.97				R	R	R	R	R	R
18H-CC, 31–36	157.81				R	R	R	R	R	R
19H-CC, 28–33	166.71				R	R	R	R	R	R
20H-CC, 46–51	174.45				R	R	R	R	R	R
21H-CC, 24–29	182.32				R	R	R	R	R	R
22H-CC, 33–38	189.00				R	R	R	R	R	R
23H-CC, 37–42	198.55				R	R	R	R	R	R
24H-CC, 18–23	201.68				R	R	R	R	R	R
25H-CC, 33–38	210.33				R	R	R	R	R	R
26H-CC, 21–26	214.08				R	R	R	R	R	R
27H-CC, 23–28	220.33				R	R	R	R	R	R
28H-CC, 33–38	227.11				R	R	R	R	R	R
29H-CC, 39–44	234.46				R	R	R	R	R	R



**Table T10.** Datums used to plot Figure F23, Hole U1322B.

Code	Event	Top		Bottom		Age (ka)	Average depth (mbsf)	Average sedimentation rate (m/k.y.)
		Core, section, interval (cm)	Depth (mbsf)	Core, section, interval (cm)	Depth (mbsf)			
PF	LO <i>G. inflata</i>	308-U1322B-1H-CC, 0–20	4	308-U1322B-2H-CC, 17–27	13.81	10	8.9	0.89
PF	Y1/Y2 boundary	3H-CC, 6–16	22.11	4H-CC, 29–34	32.92	16	27.5	3.2
PF	Y2/Y3 boundary	14H-CC, 43–48	124.8	15H-1, 95–99	125.75	24	125.3	12.2
PF	Y5/Y6 boundary	21H-CC, 24–29	182.32	22H-CC, 33–38	189	57	185.6	1.8
PF	No LO <i>P. obliquiloculata</i>			29X-CC, 39–44	234.46	65	234.46	>16

Notes: PF = planktonic foraminifer. LO = last occurrence.

**Table T11.** Summary of pass-through cryogenic magnetometer measurements, Hole U1322B.

Measurement	Core, section
Natural remanent magnetization (0, 10, 20 mT)	308-U1322B-1H-1 through 29H-5
Skipped sections	11H-8, 13H-2, 13H-5, 13H-6, 13H-7, 17H-1, 17H-4, 17H-7, and 23H-7
Fugro cutting shoe	2H, 4H, 8H, 10H, 14H, 16H, 18H, 20H, 22H, 24H, 26H, and 28H
Tensor tool	6H through 29H



**Table T12.** Results of pore water chemistry at Site U1322.

Core, section, interval (cm)	Depth (mbsf)	Alkalinity (mM)	pH	Salinity (pph)	Chlorinity (mM)	$\text{SO}_4^{2-}$ (mM)	$\text{NH}_4^+$ ( $\mu\text{M}$ )	$\text{PO}_4^{3-}$ ( $\mu\text{M}$ )	$\text{H}_4\text{SiO}_4$ (nM)	$\text{Na}^+$ (mM)	$\text{K}^+$ (mM)	$\text{Mg}^{2+}$ (mM)	$\text{Ca}^{2+}$ (mM)	$\text{B}^{3+}$ (nM)	$\text{Li}^+$ ( $\mu\text{M}$ )	$\text{Sr}^{2+}$ ( $\mu\text{M}$ )	$\text{Ba}^{2+}$ ( $\mu\text{M}$ )	$\text{Fe}^{2+}$ ( $\mu\text{M}$ )	$\text{Mn}^{2+}$ ( $\mu\text{M}$ )
<b>308-U1322B-</b>																			
1H-3, 87–100	3.87	4.09	7.16	3.8	557	31.4	428	0.0	435	515	12.4	57.3	12.6	580	26.5	96.1	1.3	72.3	61.2
2H-1, 145–150	5.45	4.74	6.89	3.7	571	31.6	618	1.1	427	523	12.2	58.8	13.1	632	27.5	103.0	0.8	224.8	27.5
2H-3, 145–150	8.45	5.27	6.85	3.7	571	31.2	909	0.0	517	507	11.1	58.2	13.9	711	29.1	108.7	0.9	350.8	18.8
2H-5, 137–142	11.37			3.7	572	32.6	1200	0.5	480	524	10.6	60.3	14.8	722	30.6	118.4	0.5	286.9	15.6
3H-1, 145–150	14.95	4.65	6.81	3.7	578	30.3	1371	0.0	438	472	8.6	55.6	14.6	781	32.7	127.6	0.6	224.3	4.8
3H-3, 145–150	17.95	4.91	6.92	3.7	577	30.7	1502	1.1	420	476	8.6	56.3	15.7	779	35.5	134.4	0.6	155.2	4.6
3H-5, 137–142	20.87	5.31	7.16	3.7	574	33.1	1391	0.0	447	505	9.1	60.1	17.9	827	39.1	138.2	0.7	155.4	3.8
4H-1, 145–150	24.45	5.48	7.17	3.8	576	30.3	1150	0.0	518	470	7.9	55.4	17.2	860	42.0	137.4	0.8	265.0	5.3
4H-3, 137–142	27.37	5.81	7.65	3.7	572	30.2	1622	0.5	469	471	7.3	56.3	18.3	881	45.2	140.4	0.5	226.9	3.7
4H-5, 145–150	30.45	5.75	7.61	3.8	574	30.5	1401	0.0	485	483	7.5	57.4	20.2	914	47.2	137.3	1.1	180.5	5.5
5H-1, 145–150	33.95	5.85	6.74	3.7	565	28.6	1311	2.8	503	469	6.7	56.5	19.5	886	46.9	134.5	0.6	194.2	6.6
5H-3, 137–142	36.87				562	29.1	1341	0.0	389	495	7.0	60.0	20.9	796	44.4	133.0	0.6	35.7	5.5
5H-5, 145–150	39.95				571	25.5	1371	1.1	414	461	7.0	55.5	19.8	874	44.0	134.3	0.6	56.2	7.4
6H-2, 145–150	44.21	5.38	6.66	3.6	558	24.9	1391	3.4	511	494	6.7	59.0	21.8	852	41.3	129.0	0.6	231.3	7.4
6H-3, 137–142	45.63	5.65	7.31	3.6	568	21.3	1351	0.0	314	448	6.5	51.9	18.6	750	42.8	128.9	0.6	19.5	4.7
6H-5, 145–150	48.71	5.54	6.96	3.5	570	20.9	1321	1.1	458	489	6.5	56.7	21.7	790	39.5	127.2	0.6	128.3	7.2
7H-3, 132–142	55.82				561	13.2	1562	1.1	370	478	6.3	53.5	19.7	677	34.0	119.2	0.1	34.0	5.2
8H-3, 137–142	65.37	4.84	6.76	3.4	563	5.8	1652	1.7	532	429	6.0	44.4	14.0	649	24.8	133.6	12.7	194.2	3.1
9H-3, 137–142	74.87				564	0.0	1853	3.4	377	470	6.3	48.0	15.1	601	19.4	134.5	36.4	99.6	3.0
10H-3, 137–142	84.37	3.75	6.46	3.3	549	0.0	2023	2.3	487	421	4.2	43.2	12.1	671	15.4	125.3	30.9	475.8	6.6
11H-3, 132–142	92.33	4.02	7.10	3.4	554	2.5	2144	2.3	327	443	4.1	45.3	11.0	638	12.9	119.4	25.5	123.4	5.8
12H-3, 132–142	103.32	5.60	6.95	3.4	556	0.0	2204	0.5	525	453	4.2	41.5	9.6	553	11.4	108.9	17.1	249.1	6.5
13H-6, 75–85	115.31	4.99	7.20	3.3	559	0.0	2836	2.3	410	447	4.2	41.4	9.7	501	10.3	93.0	11.1	78.8	3.4
14H-3, 140–150	120.70	4.85	7.26	3.4	551	0.0	2676	0.5	349	418	4.3	38.4	8.4	478	12.8	90.5	10.8	49.3	2.6
15H-3, 134–144	129.14	4.13	7.25	3.3	562	0.0	3920	2.3	359	445	4.6	40.6	8.1	457	11.1	86.0	7.9	53.1	1.0
16H-3, 140–150	138.70	4.44	7.14	3.3	559	0.0	4221	1.1	374	479	4.6	45.1	8.0	448	10.4	85.7	9.9	42.5	0.7
17H-2, 28–38	143.83	4.53	7.20	3.3	558	0.0	3749	2.3	354	455	4.8	43.5	7.4	440	11.7	85.5	10	24.4	0.2
18H-3, 140–150	154.30	5.23	7.16	3.4	557	0.0	4211	1.1	319	450	5.2	44.6	7.0	462	10.9	81.8	8.8	16.9	0.6
19H-3, 132–142	162.12	5.04	7.28	3.3	555	0.0	4422	4.0	322	432	5.4	42.3	6.7	431	12.5	81.0	9.3	39.2	0.8
20H-3, 140–150	171.10	5.72	7.17	3.3	557	0.0	4040	0.5	413	434	5.0	44.1	7.1	416	12.7	86.1	9.4	43.2	1.1
21H-3, 132–142	178.82	5.74	7.13	3.4	550	0.0	4281	1.1	463	444	5.1	45.3	7.8	440	12.9	88.7	9.3	64.5	1.6
22H-3, 140–150	186.70				552	0.0	4432	1.1	435	447	4.5	45.7	8.2	464	12.6	90.4	7.3	51.7	2.2
23H-3, 132–142	193.32	6.25	7.40	3.3	559	0.0	4412	1.1	341	459	4.3	46.3	8.4	451	12.7	90.6	7.9	26.9	1.7
24H-1, 140–150	199.90	6.18	7.14	3.3	551	0.0	3488	2.3	378	435	3.8	44.4	8.0	435	12.8	89.6	8.5	13.1	1.2
25H-4, 140–150	206.95	6.07	7.05	3.4	555	0.0	2274	1.7	373	467	4.1	47.6	8.9	423	14.7	91.0	11.7	14.9	1.4
26H-1, 122–132	211.52	6.09	7.19	3.4	550	0.0	2385	1.7	360	464	4.0	46.7	8.7	408	14.2	91.3	12.4	25.9	1.6
27H-3, 140–150	218.50	5.69	7.05	3.3	543	0.0	2425	2.3	384	445	3.4	44.4	8.5	401	12.5	91.3	10.9	31.7	1.1
28H-3, 140–150	224.70	6.14	7.11	3.4	549	0.0	2224	1.7	461	436	3.3	44.2	8.6	444	13.0	92.5	10.7	86.6	1.2
29H-3, 132–142	231.42	5.46	7.25	3.3	542	0.0	2455	2.3	259	449	3.9	42.9	8.3	374	11.8	87.3	10.6	1.0	0.0
<b>308-U1322C-</b>																			
1H-1, 90–95	0.90	3.92	7.04		553	31.1			299					545	31.1	85.3	0.1	40.6	153.7
1H-1, 145–150	1.50	3.85	7.27	3.7	560	30.0	147	2.8	358	498	12.9	53.5	10.9	549	31.2	88.9	0.7	27.3	110.9
1H-2, 90–95	2.40	3.96	7.38		557	27.3			309					532	34.0	90.5	0.5	5.1	76.6
1H-2, 145–150	3.00	4.28	7.04	3.6	558	30.9	307	2.3	424	516	12.9	56.3	12.0	580	31.3	92.0	0.5	167.6	58.8
1H-3, 128–133	4.33	4.69	7.15	3.6	559	28.5	358	2.3	354	483	11.5	52.8	11.4	616	31.3	99.3	0.5	31.8	42.8
<b>308-U1322D-</b>																			
1H-3, 140–150	44.40	5.70	6.95	3.6	559														
2H-3, 140–150	74.40	4.42	6.63	3.4	559														
3H-3, 140–150	104.40	5.26	6.88	3.4	559														

**Table T13.** Sediment elemental analysis, Holes U1322B, U1322C, and U1322D.

Core, section, interval (cm)	Depth (mbsf)	Carbon (wt%)				TN (wt%)	TH (wt%)	C/N
		Total	Inorganic	CaCO <sub>3</sub>	Organic			
<b>308-U1322B-</b>								
1H-1, 145–150	1.45	2.06	0.82	6.83	1.24	0.21	0.53	6.83
1H-3, 87–100	3.87	1.56	0.65	5.42	0.91	0.16	1.05	6.58
2H-1, 145–150	5.45	2.35	1.09	9.06	1.26	0.18	0.44	8.10
2H-3, 145–150	8.45	3.20	1.56	13.03	1.64	0.08	0.02	22.91
2H-5, 137–142	11.37	2.38	0.98	8.20	1.40	0.08	0.01	19.69
3H-1, 145–150	14.95	2.24	1.26	10.52	0.98	0.07		17.34
3H-3, 145–150	17.95	2.76	1.71	14.27	1.05	0.07	0.01	16.52
3H-5, 137–142	20.87	2.57	1.75	14.55	0.82	0.17	0.35	5.52
4H-1, 145–150	24.45	2.98	1.94	16.19	1.04	0.07		16.63
4H-3, 137–142	27.37	2.89	2.00	16.66	0.89	0.06	0.07	16.25
4H-5, 145–150	30.45	2.99	2.03	16.90	0.96	0.07		15.48
5H-1, 145–150	33.95	2.50	1.50	12.53	1.00	0.07	0.09	17.22
5H-3, 137–142	36.87	2.23	1.24	10.34	0.99	0.07		16.41
5H-5, 145–150	39.95	2.50	1.46	12.15	1.04	0.07	0.12	17.94
6H-2, 145–150	44.21	2.28	1.34	11.17	0.94	0.09	0.01	11.72
6H-3, 137–142	45.63	2.62	1.79	14.94	0.83	0.06		16.83
6H-5, 145–150	48.71	2.67	1.84	15.37	0.83	0.06	0.01	15.85
7H-3, 132–142	55.82	2.44	1.55	12.93	0.89	0.07		15.44
8H-3, 137–142	65.37	2.50	1.63	13.57	0.87	0.06		15.94
9H-3, 137–142	74.87	2.97	2.01	16.76	0.96	0.06		17.95
10H-3, 137–142	84.37	2.14	1.46	12.14	0.68	0.06		12.45
11H-3, 132–142	92.33	2.49	1.63	13.61	0.86	0.06	0.72	16.23
12H-3, 132–142	103.32	2.46	1.81	15.10	0.65	0.06		11.68
13H-6, 75–85	115.31	3.43	2.80	23.34	0.63	0.05		13.42
14H-3, 140–150	120.70	3.03	2.38	19.86	0.65	0.05	0.01	14.95
15H-3, 134–144	129.14	3.54	2.82	23.46	0.72	0.05		16.16
16H-3, 140–150	138.70	3.00	2.43	20.24	0.57	0.06		10.80
17H-2, 28–38	143.83	3.05	2.65	22.04	0.40	0.14	0.51	3.23
18H-3, 140–150	154.30	2.98	2.25	18.70	0.73	0.06		14.55
19H-3, 132–142	162.12	2.84	2.25	18.77	0.59	0.06		12.19
20H-3, 140–150	171.10	2.98	2.59	21.61	0.39	0.17	0.52	2.75
21H-3, 132–142	178.82	2.56	2.21	18.41	0.35	0.16	0.56	2.50
22H-3, 140–150	186.70	2.70	2.14	17.81	0.56	0.05	0.01	11.93
23H-3, 132–142	193.32	1.96	1.44	12.02	0.52	0.13	0.54	4.83
24H-1, 140–150	199.90	1.84	0.75	6.28	1.09	0.06	0.01	21.56
25H-4, 140–150	206.95	2.04	1.71	14.21	0.33	0.18	0.57	2.15
26H-1, 122–132	211.52	2.31	1.78	14.79	0.53	0.16	0.57	3.95
27H-3, 140–150	218.50	2.21	1.95	16.26	0.26	0.18	0.52	1.71
28H-3, 140–150	224.70	2.18	1.82	15.18	0.36	0.17	0.59	2.57
29H-3, 132–142	231.42	1.88	1.41	11.76	0.47	0.06	0.60	9.24
<b>308-U1322C-</b>								
1H-1, 90–95	0.90	3.42	2.76	22.96	0.66	0.08	1.81	9.45
1H-1, 145–150	1.45	3.64	2.66	22.13	0.98	0.11	1.72	10.15
1H-2, 90–95	2.40	1.99	1.05	8.74	0.94	0.07	2.85	15.47
1H-2, 145–150	2.95	2.20	1.07	8.88	1.13	0.08	2.34	16.88
1H-3, 128–133	4.28	1.84	0.62	5.19	1.22	0.07	0.02	19.06
<b>308-U1322D-</b>								
1H-3, 140–150	44.40	2.54	1.70	14.20	0.84	0.07	0.05	15.01
2H-3, 140–150	74.40	2.68	1.92	16.02	0.76	0.07	0.01	13.65
3H-3, 140–150	104.40	2.89	1.51	12.58	1.38	0.06	0.03	25.28

Note: TN = total nitrogen, TH = total hydrogen.



**Table T14.** Headspace gas analysis, Hole U1322B.

Core, section, interval (cm)	Depth (mbsf)	Headspace gas (ppmv)			C <sub>1</sub> /C <sub>2</sub> ratio
		Methane	Ethane	Ethylene	
308-U1322B-					
1H-3, 0–5	3.0	1.1	0.0	0.0	
2H-4, 0–5	8.5	2.6	0.0	0.0	
3H-4, 0–5	18.0	2.1	0.0	0.0	
4H-4, 0–5	27.5	3.8	0.0	0.0	
5H-4, 0–5	37.0	6.3	0.0	0.0	
6H-4, 0–5	45.8	3.6	0.0	0.0	
7H-4, 0–5	56.0	6.9	0.0	0.0	
8H-4, 0–5	65.5	2,305	0.0	0.0	
9H-4, 0–5	75.0	51,002	2.7	0.0	18,890
10H-4, 0–5	84.5	43,985	3.1	2.6	14,189
12H-4, 0–5	103.5	33,217	3.4	0.0	9,770
13H-6, 0–5	114.6	31,248	2.6	0.0	12,018
14H-4, 0–5	120.8	26,154	2.9	0.0	9,019
15H-4, 0–5	129.3	29,536	1.9	0.0	15,545
16H-4, 0–5	138.8	6,835	0.0	0.0	
17H-5, 0–5	145.6	5,826	1.0	0.0	5,944
18H-4, 0–5	154.4	1,599	0.0	0.0	
19H-4, 0–5	162.3	1,097	0.0	0.0	
20H-4, 0–5	171.2	5,198	0.0	0.0	
21H-4, 0–5	179.0	2,520	0.0	0.0	
22H-4, 0–5	186.8	6,520	0.0	0.0	
23H-4, 0–5	193.5	3,573	0.0	0.0	
24H-2, 0–5	200.0	6,391	0.0	0.0	
25H-5, 0–5	207.1	5,957	0.0	0.0	
28H-4, 0–5	224.8	10,302	0.0	0.0	
29H-4, 0–5	231.6	10,419	0.0	0.0	

**Table T15.** Microbiology, Hole U1322B.

Core, section, interval (cm)	Cell density (cells/mL)	Comments
308-U1322B-		
1H-2, 2.9–3.0	$4.0 \times 10^5$	
2H-2, 6.9–7.0	$2.5 \times 10^5$	
2H-5, 11.4–11.5	$1.3 \times 10^5$	
3H-2, 16.4–16.5	$1.0 \times 10^5$	
3H-5, 20.9–21.0	$1.0 \times 10^5$	
4H-3, 27.4–27.5	$5.0 \times 10^4$	
5H-3, 36.9–37.0	$7.1 \times 10^4$	
6H-3, 45.7–45.8	$1.7 \times 10^4$	
7H-3, 55.9–56.0	ND	
8H-3, 65.4–65.5	ND	
9H-3, 74.9–75.0	ND	
10H-3, 84.4–84.5	ND	
11H-3, 92.4–92.5	ND	
12H-3, 103.4–103.5	ND	No contamination test
13H-6, 114.4–115.5	ND	
15H-3, 129.2–129.3	ND	
17H-2, 143.8–143.8	ND	
19H-3, 162.2–162.3	ND	
21H-3, 178.9–179.0	ND	
23H-3, 193.4–193.5	ND	
26H-1, 211.6–211.7	ND	
29H-3, 231.5–231.6	ND	

Note: ND = not detected or below cell enumeration confidence limit (=  $1.0 \times 10^4$  cells/mL).



**Table T16.** Downhole tool deployment, Site U1322.

Hole	Tool	Deployment	Depth		Date (2005)	Time in formation (min)
			(mbsf)	(mbsl)		
308-						
U1322B	T2P	17	42.0	1361.7	28 Jun	60
U1322B	T2P	19	134.3	1454.0	29 Jun	30
U1322B	T2P	20	157.8	1477.5	29 Jun	60
U1322C	T2P	21	50.0	1368.9	30 Jun	60
U1322C	T2P	22	75.0	1393.9	30 Jun	60
U1322C	T2P	23	150.0	1468.9	1 Jul	60
U1322C	T2P	24	200.0	1518.9	1 Jul	60
U1322D	T2P	25	40.0	1358.9	1 Jul	60
U1322D	T2P	26	70.0	1388.9	2 Jul	45
U1322D	T2P	27	100.0	1418.9	2 Jul	45
U1322D	T2P	28	134.0	1452.9	2 Jul	45
U1322B	DVTTP	16	166.7	1486.4	29 Jun	90
U1322C	DVTTP	17	100.0	1418.9	30 Jun	90
U1322C	DVTTP	18	220.0	1538.9	1 Jul	60
U1322C	DVTTP	19	238.0	1556.9	1 Jul	90
U1322D	DVTTP	20	175.0	1493.9	2 Jul	60
U1322B	APCT	6	80.0	1399.7	29 Jun	10
U1322B	APCT	7	108.5	1428.2	29 Jun	10

Note: T2P = temperature/dual pressure probe, DVTTP = Davis-Villinger Temperature-Pressure Probe, APCT = advanced piston corer temperature tool.

**Table T17.** T2P Deployment 17, Hole U1322B.

Event	Time (GMT)	Description
1	18:39:55	Data logger started at 1 Hz
2	20:10:31	T2P on rig floor
3	20:22:12	Start lowering T2P downhole, pumps on
4	20:29:54	Stop at 491 mbsl, pumps off
5	20:31:58	Start lowering probe
6	20:35:04	Stop at 741 mbsl, pumps off
7	20:37:04	Start lowering probe
8	20:43:20	Stop at 1321 mbsl, pumps off
9	20:46:30	Start lowering probe
10	20:48:58	Stop at 1351 mbsl, pumps off
11	20:50:55	Start lowering probe
12	20:57:30	CDS lands in BHA; pumps off
13	20:57:49	Start penetration of T2P into sediment
14	21:00:31	End of T2P penetration; bit on bottom of hole
15	21:00:37	Raising BHA 4.0 m off bottom of hole
16	22:07:42	Pulling T2P uphole slowly with wireline
17	22:10:32	Stop at 1321 mbsl, pumps off
18	22:13:27	Pulling T2P uphole slowly with wireline
19	22:19:47	Stop at 741 mbsl, pumps off
20	22:21:57	Pulling T2P uphole slowly with wireline
21	22:26:12	Stop at 491 mbsl, pumps off
22	22:28:28	Pulling T2P uphole slowly with wireline
23	22:32:54	Wireline disconnected from CDS
24	22:35:38	CDS disconnected from spacer
25	22:37:15	Spacer disconnected from CDS
26	22:38:00	T2P out of pipe
27		Data downloaded from data logger

Notes: Depth = 42.0 mbsf. Date = 28 June 2005. T2P = temperature/dual pressure probe. CDS = colleted delivery system. BHA = bottom-hole assembly.



**Table T18.** T2P Deployment 19, Hole U1322B.

Event	Time (GMT)	Description
1		Data logger started at 1 Hz
2	12:30:53	Start lowering T2P downhole, pumps on
3	12:36:29	Stop at 491 mbsl, pumps off
4	12:38:38	Start lowering probe
5	12:44:32	Stop at 741 mbsl, pumps off
6	12:46:30	Start lowering probe
7	13:03:56	Stop at 1321 mbsl, pumps off
8	13:07:17	Start lowering probe
9	13:34:36	Stop at 1443 mbsl, pumps off
10	13:36:23	Start lowering probe
11	13:41:16	CDS lands in BHA; pumps off
12	13:52:56	Start penetration of T2P into sediment
13	13:54:18	End of T2P penetration; bit on bottom of hole
14	13:54:18	Raising BHA 4.0 m off bottom of hole
15	14:25:47	Pulling T2P uphole slowly with wireline
16	14:29:38	Stop at 1321 mbsl, pumps off
17	14:31:25	Pulling T2P uphole slowly with wireline
18	14:40:06	Stop at 741 mbsl, pumps off
19	14:41:40	Pulling T2P uphole slowly with wireline
20	14:46:08	Stop at 491 mbsl, pumps off
21	14:47:40	Pulling T2P uphole slowly with wireline
22		Data downloaded from data logger

Notes: Depth = 134.3 mbsf. Date = 29 June 2005. T2P = temperature/dual pressure probe. CDS = colleted delivery system. BHA = bottom-hole assembly.

**Table T19.** T2P Deployment 20, Hole U1322B.

Event	Time (GMT)	Description
1		Data logger started at 1 Hz
2	18:15:52	T2P on rig floor
3	18:38:28	Start lowering T2P downhole, pumps on
4	18:46:30	Stop at 491 mbsl, pumps off
5	18:49:40	Start lowering probe
6	18:54:04	Stop at 741 mbsl, pumps off
7	18:57:00	Start lowering probe
8	19:05:42	Stop at 1321 mbsl, pumps off
9	19:08:33	Start lowering probe
10	19:13:48	Stop at 1467 mbsl, pumps off
11	19:19:02	Start lowering probe
12	19:36:51	CDS lands in BHA; pumps off
13	19:36:52	Start penetration of T2P into sediment
14	19:37:39	End of T2P penetration; bit on bottom of hole
15	19:37:50	Raising BHA 4.0 m off bottom of hole
16	20:43:13	Pulling T2P uphole slowly with wireline
17	21:10:30	Wireline disconnected from CDS
18	21:13:15	CDS disconnected from spacer
19	21:14:30	Spacer disconnected from CDS
20	22:15:00	T2P out of pipe
21		Data downloaded from data logger

Notes: Depth = 157.8 mbsf. Date = 29 June 2005. T2P = temperature/dual pressure probe. CDS = colleted delivery system. BHA = bottom-hole assembly.



**Table T20.** T2P Deployment 21, Hole U1322C.

Event	Time (GMT)	Description
1	17:16:36	Data logger started at 1 Hz
2	18:53:12	Start lowering T2P downhole, pumps on
3	18:59:12	Stop at 491 mbsl, pumps off
4	19:01:57	Start lowering probe
5	19:06:02	Stop at 741 mbsl, pumps off
6	19:08:10	Start lowering probe
7	19:15:34	Stop at 1321 mbsl, pumps off
8	19:17:39	Start lowering probe
9	19:21:57	Stop at 1359 mbsl, pumps off
10	19:23:32	Start lowering probe
11	19:28:12	CDS lands in BHA; pumps off
12	19:28:30	Start penetration of T2P into sediment
13	19:30:07	End of T2P penetration; bit on bottom of hole
14	19:30:14	Raising BHA 4.0 m off bottom of hole
15	20:33:35	Pulling T2P uphole slowly with wireline
16	20:35:24	Stop at 1321 mbsl, pumps off
17	20:37:37	Pulling T2P uphole slowly with wireline
18	20:43:30	Stop at 741 mbsl, pumps off
19	20:45:47	Pulling T2P uphole slowly with wireline
20	20:48:59	Stop at 491 mbsl, pumps off
21	20:51:12	Pulling T2P uphole slowly with wireline
22	20:56:27	Wireline disconnected from CDS
23	20:59:15	CDS/spacer disconnected from spacer
24	21:05:00	T2P out of pipe
25	21:15:00	Data downloaded from data logger

Notes: Depth = 50.0 mbsf. Date = 30 June 2005. T2P = temperature/dual pressure probe. CDS = colleted delivery system. BHA = bottom-hole assembly.

**Table T21.** T2P Deployment 22, Hole U1322C.

Event	Time (GMT)	Description
1		Data logger started at 1 Hz
2	22:18:46	Start lowering T2P downhole, pumps on
3	22:29:40	Stop at 491 mbsl, pumps off
4	22:31:51	Start lowering probe
5	22:35:38	Stop at 741 mbsl, pumps off
6	22:37:41	Start lowering probe
7	22:45:54	Stop at 1321 mbsl, pumps off
8	22:48:16	Start lowering probe
9	22:51:43	Stop at 1384 mbsl, pumps off
10	22:54:50	Start lowering probe
11	22:59:47	CDS lands in BHA; pumps off
12	22:59:57	Start penetration of T2P into sediment
13	23:00:52	End of T2P penetration; bit on bottom of hole
14	23:01:10	Raising BHA 4.0 m off bottom of hole
15	00:03:25	Pulling T2P uphole slowly with wireline
16	00:06:30	Stop at 1321 mbsl, pumps off
17	00:08:30	Pulling T2P uphole slowly with wireline
18	00:15:04	Stop at 741 mbsl, pumps off
19	00:17:14	Pulling T2P uphole slowly with wireline
20	00:20:20	Stop at 491 mbsl, pumps off
21	00:22:30	Pulling T2P uphole slowly with wireline
22	00:29:40	Wireline disconnected from CDS
23	00:31:25	CDS/spacer disconnected from spacer
24	00:32:42	T2P out of pipe
25		Data downloaded from data logger

Notes: Depth = 75.0 mbsf. Date = 30 June 2005. T2P = temperature/dual pressure probe. CDS = colleted delivery system. BHA = bottom-hole assembly.

**Table T22.** T2P Deployment 23, Hole U1322C.

Event	Time (GMT)	Description
1		Data logger started at 1 Hz
2	6:51:00	T2P on rig floor
3	7:01:01	Start lowering T2P downhole, pumps on
4	7:09:59	Stop at 491 mbsl, pumps off
5	7:12:10	Start lowering probe
6	7:17:10	Stop at 741 mbsl, pumps off
7	7:19:30	Start lowering probe
8	7:29:29	Stop at 1321 mbsl, pumps off
9	7:43:31	Start lowering probe
10	7:52:12	Stop at 1459 mbsl, pumps off
11	7:54:02	Start lowering probe
12	7:58:21	CDS lands in BHA; pumps off
13	7:58:31	Start penetration of T2P into sediment
14	8:02:56	End of T2P penetration; bit 1 m off bottom of hole
15	8:03:30	Raising BHA 4.0 m off bottom of hole
16	9:05:35	Pulling T2P uphole slowly with wireline
17	9:12:44	Stop at 1321 mbsl, pumps off
18	9:14:59	Pulling T2P uphole slowly with wireline
19	9:24:45	Stop at 741 mbsl, pumps off
20	9:26:45	Pulling T2P uphole slowly with wireline
21	9:32:17	Stop at 491 mbsl, pumps off
22	9:34:17	Pulling T2P uphole slowly with wireline
23		Data downloaded from data logger

Notes: Depth = 150.0 mbsf. Date = 01 July 2005. T2P = temperature/dual pressure probe. CDS = colleted delivery system. BHA = bottom-hole assembly.

**Table T23.** T2P Deployment 24, Hole U1322C.

Event	Time (GMT)	Event
1		Data logger started at 1 Hz
2	12:39:36	Stop at 1509 mbsl, pumps off
3	12:12:23	Start lowering probe
4	12:51:28	End of T2P penetration; bit 1 m off bottom of hole
5	12:51:28	Raising BHA 4.0 m off bottom of hole
6	13:51:30	Pulling T2P uphole slowly with wireline
7	14:09:00	Stop at 741 mbsl, pumps off
8	14:11:00	Pulling T2P uphole slowly with wireline
9	14:14:37	Stop at 491 mbsl, pumps off
10	14:16:37	Pulling T2P uphole slowly with wireline
11		Data downloaded from data logger

Notes: Depth = 200.0 mbsf. Date = 01 July 2005. T2P = temperature/dual pressure probe.



**Table T24.** T2P Deployment 25, Hole U1322D.

Event	Time (GMT)	Description
1		Data logger started at 1 Hz
2	2:06:25	Start lowering T2P downhole, pumps on
3	2:14:56	Stop at 491 mbsl, pumps off
4	2:21:58	Stop at 741 mbsl, pumps off
5	2:32:58	Stop at 1321 mbsl, pumps off
6	2:38:36	Stop at 1349 mbsl, pumps off
7	2:40:40	Start lowering probe
8	2:45:08	CDS lands in BHA; pumps off
9	2:46:36	Start penetration of T2P into sediment
10	2:46:51	End of T2P penetration; bit 0.8 m off bottom of hole
11	2:46:56	Raising BHA 4.0 m off bottom of hole
12	3:49:19	Pulling T2P uphole slowly with wireline
13	3:52:54	Stop at 1321 mbsl, pumps off
14	3:55:26	Pulling T2P uphole slowly with wireline
15	4:02:38	Stop at 741 mbsl, pumps off
16	4:04:48	Pulling T2P uphole slowly with wireline
17	4:08:33	Stop at 491 mbsl, pumps off
18	4:10:41	Pulling T2P uphole slowly with wireline
19		Data downloaded from data logger

Notes: Depth = 40.0 mbsf. Date = 01 July 2005. T2P = temperature/dual pressure probe. CDS = colleted delivery system. BHA = bottom-hole assembly

**Table T25.** T2P Deployment 26, Hole U1322D.

Event	Time (GMT)	Event
1		Data logger started at 1 Hz
2	6:32:00	T2P on rig floor
3	6:56:53	Stop at 741 mbsl, pumps off
4	7:07:51	Stop at 1321 mbsl, pumps off
5	7:18:15	Stop at 1386 mbsl, pumps off
6	7:20:27	Start lowering probe
7	7:24:50	CDS lands in BHA; pumps off
8	7:26:47	Start penetration of T2P into sediment
9	7:27:48	End of T2P penetration; bit 0.8 m off bottom of hole
10	7:27:54	Raising BHA 4.0 m off bottom of hole
11	8:14:30	Pulling T2P uphole slowly with wireline
12	8:16:29	Stop at 1321 mbsl, pumps off
13	8:26:26	Stop at 741 mbsl, pumps off
14	8:32:09	Stop at 491 mbsl, pumps off
15		Data downloaded from data logger

Notes: Depth = 70.0 mbsf. Date = 02 July 2005. T2P = temperature/dual pressure probe. CDS = colleted delivery system. BHA = bottom-hole assembly.



**Table T26.** T2P Deployment 27, Hole U1322D.

Event	Time (GMT)	Description
1		Data logger started at 1 Hz
2	11:04:50	Stop at 491 mbsl, pumps off
3	11:15:50	Stop at 741 mbsl, pumps off
4	11:15:56	Stop at 1321 mbsl, pumps off
5	11:24:06	Stop at 1409 mbsl, pumps off
6	11:26:27	Start lowering probe
7	11:29:25	CDS lands in BHA; pumps off
8	11:29:26	Start penetration of T2P into sediment
9	11:30:20	End of T2P penetration; bit 0.8 m off bottom of hole
10	11:30:25	Raising BHA 4.0 m off bottom of hole
11	12:16:01	Pulling T2P uphole slowly with wireline
12	12:19:11	Stop at 1321 mbsl, pumps off
13	12:28:55	Stop at 741 mbsl, pumps off
14	12:35:10	Stop at 491 mbsl, pumps off
15		Data downloaded from data logger

Notes: Depth = 100.0 mbsf. Date = 02 July 2005. T2P = temperature/dual pressure probe. CDS = colleted delivery system. BHA = bottom-hole assembly.

**Table T27.** Summary of T2P Deployment 28, Hole U1322D.

Event	Time (GMT)	Description
1		Data logger started at 1 Hz
2	14:52:35	T2P on rig floor
3	15:10:03	Stop at 491 mbsl, pumps off
4	15:12:03	Start lowering probe
5	15:15:00	Stop at 741 mbsl, pumps off
6	15:16:15	Start lowering probe
7		Data downloaded from data logger

Notes: Depth = 134.0 mbsf. Date = 2 July 2005. T2P = temperature/dual pressure probe.